

https://dspace.org/

The Effects of Rectilinear Acceleration and Deceleration on Shock Formation near a Stationary Boundary

Morrow, Sean Robert

2024

University of the Witwatersrand, Johannesburg

https://hdl.handle.net/10539/45594

Morrow, Sean Robert . (2024). The Effects of Rectilinear Acceleration and Deceleration on Shock Formation near a Stationary Boundary [Master`s dissertation, University of the Witwatersrand, Johannesburg]. WIReDSpace. https://hdl.handle.net/10539/45594

Downloaded from a DSpace repository. https://dspace.org/



The Effects of Rectilinear Acceleration and Deceleration on Shock Formation near a Stationary Boundary

Sean Robert Morrow

(Student number: 346718)

School of Mechanical, Industrial and Aeronautical Engineering

University of the Witwatersrand

Johannesburg, South Africa

Supervisors:

Dr H. Roohani, Prof B. W. Skews and Prof I. Gledhill

A research dissertation submitted to the Faculty of Engineering and the Built Environment, University of the Witwatersrand, in fulfillment of the requirements for the degree of Masters in Engineering.

15 July 2024

UNIVERSITY OF THE WITWATERSRAND, JOHANNESBURG
SCHOOL OF MECHANICAL, INDUSTRIAL AND AERONAUTICAL ENGINEERING

PLAGIARISM DECLARATION TO BE SIGNED BY ALL HIGHER DEGREE STUDENTS

SENATE PLAGIARISM POLICY: APPENDIX ONE

I, (name) **Sean Robert Morrow**, (Student number) **346718**, am a student registered for the degree of **MECN8000A**, (course name) **MSc Dissertation** in the academic year **2024**.

I hereby declare the following:

- I am aware that plagiarism (the use of someone else's work without their permission and / or without acknowledging the original source) is wrong;
- I confirm that the work submitted herewith for assessment in the above course is my own unaided work except where we have explicitly indicated otherwise;
- This task has not been submitted before, either individually or jointly, for any course requirement, examination, or degree at this or any other tertiary educational institution;
- I have followed the required conventions in referencing the thoughts and ideas of others;
- I understand that the University of the Witwatersrand may take disciplinary action against me if it can be shown that this task is not our own unaided work or that I have failed to acknowledge the sources of the ideas or words in my writing in this task.

Signature:  Date: **15-07-24**

ACKNOWLEDGEMENTS

I would like to acknowledge my supervisors Dr Hamed Roohani, Prof. Beric Skews and Prof. Irvy Gledhill for their guidance in the conduction of this research. I would also like to thank MerSETA and Prof. Skews for providing funding for this research and Prof. Gledhill for her valuable insight and support.

I am greatly appreciative of my friends and family for their support. Most of all I would like to express my deepest gratitude to my wife, Amy Naicker, who's unwavering and endless support and encouragement throughout this journey. For all her emotional strength, all the personal and financial sacrifices that she has made for us and for her belief in me, even during the most challenging times. I could not have reached this milestone without her patience, love and encouragement. This achievement is as much hers as it is mine.

ABSTRACT

Inspired by the world land speed record vehicles the Thrust and Bloodhound supersonic cars (SSC), the focus of this dissertation is to investigate how rapid acceleration affects the formation of shock waves coming off an object travelling in ground effect. Due to the proximity of the ground, these shock waves are not able to freely propagate under the object and must interact with, and reflect off, the ground. Steady state and transient models of aerofoils, accelerating from Mach 0.05 to Mach 2.00 at a test run acceleration of 3 g and an extreme acceleration of 176 g are developed and compared to reveal that the transient shock wave development trails that of the constant velocity aerofoil. The main reason for this difference is that the transient flow is unable to fully develop and reach a state of equilibrium. The extreme acceleration allowed even less time for the flow to develop, and the difference in the shock location continuously increased throughout the acceleration. The same difference in shock location was evident when these models were decelerated back down to Mach 0.05. However, the extreme deceleration and increasing difference in shock location drastically changed the transonic and subsonic flow field, especially as flow features and shock waves from the higher velocity flow overtook the model. In each acceleration and deceleration case, the transient flow history effects subsided and the aerodynamic performance from the transient analysis converged with the aerodynamic performance from the steady state analysis. Under acceleration the transient performance converged at a higher steady state Mach number, while under deceleration the transient performance converged at a lower steady state Mach number. As the magnitude of the acceleration and deceleration increased the Mach number at which the results converged shifted to higher and lower Mach numbers respectively. Models with different orientations and ground clearances were also compared against each other and a case at free flight to determine the impact ground effect has on the formations and locations of the shock waves. Increasing ground effect was shown to promote the formation of shock waves under the inverted aerofoil and in general delay the propagation of the bow shock between the model and the ground. Once the bow shock propagations passed underneath the models, the resulting flow field converged with free flight conditions and ground effect no longer had an impact on the supersonic aerodynamic performance of these models. Under some conditions, the combination of ground effect and the transient effects of acceleration or deceleration can cause dangerous lift and pitch conditions.

PUBLISHED WORK

Aspects of this dissertation have been presented and published in the following references:

1. S. R. Morrow, H. Roohani, B. W. Skews, I. M. A. Gledhill, and B. J. Evans, “The Effects of Rectilinear Acceleration on Shock Formation in Ground Effect”, *Proceedings of the 23rd International Shock Interaction Symposium*, Kruger National Park, South Africa, 9-13 July 2018, ed. R. T. Paton and B. W. Skews, 159-164, 2018 ISBN 978-0-620-80449-3 (eBook) 978-0-620-80448-6 (Print) [1].

2. S. R. Morrow, H. Roohani, B. W. Skews, I. Gledhill, and B. J. Evans, “The Aerodynamic Performance of an Aerofoil in Tri-sonic Ground Effect,” in *Proceedings of the 32nd International Symposium on Shock Waves (ISSW32 2019)*, Research Publishing Services, 2019, pp. 261–274. doi: 10.3850/978-981-11-2730-4_0376-cd [2].

TABLE OF CONTENTS

DECLARATION ii
ACKNOWLEDGEMENTS iii
ABSTRACT iv
PUBLISHED WORK v
TABLE OF CONTENTS vi
LIST OF FIGURES viii
LIST OF TABLES xiii
NOMENCLATURE xiv
1 INTRODUCTION 1
1.1 Purpose of the Study 1
1.2 Research Background 1
1.3 Research Motivation 3
1.4 Problem Statement 3
1.5 Research Objectives 4
2 LITERATURE REVIEW 5
2.1 Unsteady flow effects due to acceleration and deceleration 5
2.2 Transonic Flow 7
2.3 Shock Wave Theory 8
2.3.1 Normal Shock Waves 8
2.3.2 Oblique Shock Waves 8
2.3.3 Detached Shock Waves 9
2.3.4 Shock Formation on an Aerofoil 10
2.3.5 Shock Wave Reflections 11
2.3.6 Boundary Layer Interaction 12
2.4 Numerical modelling techniques 13
2.4.1 Techniques for constant velocity cases 14
2.4.2 Technique for accelerating objects in compressible fluids. 15
2.5 Ground Effect 17
3 NUMERICAL MODELLING 19
3.1 Steady state flow analysis 20
3.2 Transient flow analysis 20

3.3 Applying the Source Terms 21
3.4 Validation 21
3.4.1 Mesh independence 22
3.4.2 Steady state free flight conditions 22
3.4.3 Turbulence models 23
3.4.4 Transonic flow features in ground effect 23
3.4.5 Time step independence 25
3.4.6 Source term technique 26
4 RESULTS 27
4.1 Upright RAE 2822 aerofoil 27
4.1.1 Ground Effect 27
4.1.2 Transient Effects 33
4.1.3 Angle of Attack 38
4.2 Inverted RAE 2822 aerofoil 40
4.2.1 Ground Effect 40
4.2.2 Transient Effects 48
4.2.3 Angle of Attack 73
5 DISCUSSION 75
5.1 Aerodynamics 75
5.1.1 Ground Effect 75
5.1.2 Transient Effect 79
6 CONCLUDING REMARKS 83
6.1 Conclusions 83
6.2 Recommendation for Further Work 85
REFERENCES 87
APPENDIX A: User-Defined Function for Modelling Acceleration 90

LIST OF FIGURES

Figure 1: Thrust SSC in Black Rock Desert [3] 1
Figure 2: Aerial photo of the bow shockwave coming off the Thrust SSC [3] 1
Figure 3: Correlation between CFD pressure results and Pendine test pressure readings at different Mach numbers [5]. 2
Figure 4: CFD pressure distribution across the lower surface of the Thrust SSC [5]. 2
Figure 5: A particle moving at a) constant subsonic velocity and b) constant supersonic velocity [9]. 5
Figure 6: A particle accelerating from subsonic to supersonic velocity [9]. 6
Figure 7: An accelerated particle decelerating from supersonic velocity to subsonic velocity [9]. 6
Figure 8: Qualitative illustration of the variation of flow field properties across a normal shock wave [15] 8
Figure 9: Supersonic flow over a (a) concave corner and a convex corner (b) causing a single oblique shock wave and expansion fan respectively [15]. 8
Figure 10: Attached and detached shock waves for corner flow and around a wedge [15]. 9
Figure 11: Supersonic flow over a blunt body [15]. 10
Figure 12: Shock wave formation on an aerofoil [15]. 11
Figure 13: Shock wave formation on an aerofoil with flow separation [16]. 11
Figure 14: Regular and Mach oblique shock reflections [17]. 12
Figure 15: A normal shock wave without boundary layer separation. Ben-Dor *et al.* (2001) [17] 13
Figure 16: A normal shock wave with boundary layer separation, forming a lambda shock. Ben-Dor *et al.* (2001) [17] 13
Figure 17: Pressure flood plot comparison of an aerofoil moving at M0.85; modelled using (a) the moving reference technique and (b) the pressure-far-field technique [19]. 14
Figure 18: Pressure flood plot produced by the constant acceleration of the fluid at the upstream pressure-far-field boundary [19]. 15
Figure 19: Pressure flood plot of a uniformly accelerated fluid using the pressure-far-field technique with source terms [19]. 17
Figure 20: Domain, boundary settings and meshing technique used for all the aerofoil models. 19
Figure 21: AGARD case 9 validation with ground effect, validation model (bottom) against validated results from literature (top). Ground clearances of h/c = 1.00 (left) and 0.50 (right) [34]. 24
Figure 22: Comparison of the Mach number contours produced by the validation model (right) against existing validated research (left, [34]) 24
Figure 23: Comparison of the Mach number contours produced by Doig *et al*. (2012) left and the validation model (right). 24
Figure 24: Overall (left) and subsonic and transonic (right) lift performance for the upright RAE 2822 aerofoil at different ground clearances. 28
Figure 25: Overall (left) and subsonic and transonic (right) drag performance for the upright RAE 2822 aerofoil at different ground clearances. 28

Figure 26: Mach flood plots of the development of flow field and shock formations for the upright aerofoil at different Mach numbers and constant ground clearance of h/c = 0.50. 29
Figure 27: Subsonic drag performance for the upright RAE 2822 aerofoil at different ground clearances. 30
Figure 28: Overall (left) and supersonic (right) aerodynamic efficiency for the upright RAE 2822 aerofoil at different ground clearances. 31
Figure 29: Pitching moment performance for the upright RAE 2822 aerofoil at different ground clearances.....31
Figure 30: Subsonic and transonic pitching moment performance for the upright RAE 2822 aerofoil at different ground clearances. 32
Figure 31: Mach number plot comparison of the propagation of the reflected bow shock under the upright RAE 2822 aerofoil at two different ground clearances. 33
Figure 32: Upright RAE 2822 aerofoil, h/c = 1.0 - steady state and transient lift (left) and drag (right) performance curves.....34
Figure 33: Upright RAE 2822 aerofoil, h/c = 1.0 - steady state and transient pitching moment (left) and aerodynamic efficiency (right) performance curves 34
Figure 34: Upright RAE 2822 aerofoil, h/c = 1.00 – difference in steady state (left) and transient (right) results at (a) Mach 0.70, (b) Mach 0.85 and (c) Mach 1.10.....36
Figure 35: Upright RAE 2822 aerofoil, h/c = 1.00 - comparison of steady state (left) and transient acceleration (right) shock wave development and propagation. 37
Figure 36: Upright RAE 2822 aerofoil, h/c = 1.00 – (a) density contours and (b) Mach flood plots for the steady state (left) and transient (right) shock structures at Mach 1.30 37
Figure 37: Upright RAE 2822 aerofoil, h/c = 0.50 – lift (left) and pitching moment (right) performance curves at different angles of attack. 38
Figure 38: Upright RAE 2822 aerofoil, h/c = 0.50 – drag (left) and aerodynamic efficiency (right) performance curves at different angles of attack. 39
Figure 39: Density contour plots for angle of attack analysis of the RAE 2822 aerofoil at Mach 0.85 39
Figure 40: Density contour plots for angle of attack analysis of the RAE 2822 aerofoil at Mach 1.70. Angle of attack increases from left to right, $\boldsymbol{\alpha = 0.00°}$ (left), $\boldsymbol{\alpha = 2.79°}$ (middle), and $\boldsymbol{\alpha = 6.00°}$ (right).....40
Figure 41: Inverted RAE 2822 aerofoil - ground effect lift performance overall (left) and subsonic to transonic (right) comparison. 41
Figure 42: Inverted RAE 2822 aerofoil - ground effect drag performance overall (left) and subsonic to transonic (right) comparison. 42
Figure 43: Inverted RAE 2822 aerofoil - ground effect pitching moment performance comparison overview (left) and subsonic to transonic results (right).....43
Figure 44: Inverted RAE 2822 aerofoil – ground effect aerodynamic efficiency comparison overview (left) and supersonic results (right) 44
Figure 45: Pressure distributions at Mach 0.85 for two sets of ground clearances (a) free flight, h/c = 1.00 and h/c = 0.50 and (b) h/c = 0.25, 0.10 and 0.05. 44
Figure 46: Density contour plots for an inverted RAE 2822 aerofoil traveling Mach 2.00 at free stream (left), h/c = 1.00 (middle) and h/c = 0.50 (right).....45

Figure 47: Inverted RAE 2822 pressure distributions at Mach 2.00 for two sets of ground clearances (a) free stream, h/c = 1.00 and h/c = 0.50 and (b) h/c = 0.25, 0.10 and 0.05. 45
Figure 48: Density contour plots for an inverted RAE 2822 aerofoil traveling Mach 2.00 at h/c = 0.25 (left), h/c = 0.10 (middle) and h/c = 0.05 (right). 45
Figure 49: Density plots of the RAE 2822 shock wave development from Mach 0.40 (left) to Mach 2.40 (right) at free flight, h/c = 1.00 and h/c = 0.50. 46
Figure 50: Density plots of the RAE 2822 shock wave development from Mach 0.40 (left) to Mach 2.40 (right) at h/c = 0.25, h/c = 0.10 and h/c = 0.05. 47
Figure 51: Inverted RAE 2822 aerofoil, α = -2.79° and h/c = 1.00 - steady state, ± 176g acceleration 48
Figure 52: Inverted RAE 2822 aerofoil density contour plots at steady state, 176 g, and -176 g respectively, taken at Mach 1.20.....50
Figure 53: Inverted RAE 2822 ratio of transient to steady state downforce performance. 50
Figure 54: Inverted RAE 2822 percentage deviation of transient from steady state downforce performance under Mach 0.80. 51
Figure 55: Inverted RAE 2822 aerofoil, α = -2.79° and h/c = 1.00 - steady state, ± 176g acceleration drag performance 52
Figure 56: Inverted RAE 2822 ratio of transient to steady state drag performance. 52
Figure 57: Inverted RAE 2822 ratio of transient to steady state drag performance above Mach 1.00.....53
Figure 58: Inverted RAE 2822 aerofoil, α = -2.79° and h/c = 1.00 - steady state, 176g acceleration and 176g deceleration pitching moment performance 53
Figure 59: Inverted RAE 2822 ratio of transient to steady state pitching moment performance. 54
Figure 60: Inverted RAE 2822 aerofoil, α = -2.79°, h/c = 1.00 - steady state (left), 176g acceleration (middle) and 176g deceleration (right) Mach number flood plots and density contour plots at Mach 0.85.....55
Figure 61: Steady state (top left), 176g acceleration (top middle) and 176g deceleration (top right) coefficient of pressure plots for an inverted aerofoil at Mach 0.85 and α = -2.79°. 56
Figure 62: Inverted RAE 2822 aerofoil, h/c = 1.00 and α = -2.79° - steady state (left), 176g acceleration (middle) and 176g deceleration (right) density contour plots results at Mach 1.20.....57
Figure 63: Inverted RAE 2822 aerofoil, h/c = 1.00 and α = -2.79° - steady state vs transient ±176g shock locations along the aerofoil (left) and ground plane (right) at a Mach number of 1.20.....58
Figure 64: Inverted RAE 2822 aerofoil, α = -2.79°, h/c = 1.00 and - steady state (left), 176g acceleration (middle) and 176g deceleration (right) Mach number and density contour plots at Mach 1.50. 58
Figure 65: Inverted RAE 2822 aerofoil, h/c = 1.00 and α = -2.79° - steady state (left), 176g acceleration (middle) and 176g deceleration (right) density contour plots at Mach 0.50 58
Figure 66: Inverted RAE 2822 aerofoil, h/c = 1.00 and α = -2.79° - steady state (left), 176g acceleration (middle) and 176g deceleration (right) density contour plots results at Mach 0.50.....59

Figure 67: Inverted RAE 2822 aerofoil, h/c = 1.00 and α = -2.79 ° - steady state (left), 176g acceleration (middle) and 176g deceleration (right) coefficient of pressure plot comparison at Mach 0.50. 59
Figure 68: Inverted RAE 2822 aerofoil, h/c = 1.00 and α = -2.79 ° - steady state (left), 176g acceleration (middle) and 176g deceleration (right) density contour plots at Mach 0.50. 59
Figure 69: Inverted RAE 2822 aerofoil, h/c = 1.00 and α = -2.79 ° - steady state and 40 g acceleration downforce performance comparison. 60
Figure 70: Inverted RAE 2822 aerofoil, h/c = 1.00 and α = -2.79 ° - steady state and 40 g acceleration drag performance comparison. 61
Figure 71: Inverted RAE 2822 aerofoil, h/c = 1.00 and α = -2.79 ° - steady state, 40 g acceleration and 40 g deceleration pitching moment performance comparison. 61
Figure 72: Shock locations for 40 g deceleration at Mach 0.675 (left), Mach 0.70 (centre) and Mach 0.725 (right) 62
Figure 73: Inverted RAE 2822 aerofoil, h/c = 1.00 and α = -2.79 ° - steady state and 3 g acceleration downforce performance comparison. 63
Figure 74: Inverted RAE 2822 aerofoil, h/c = 1.00 and α = -2.79 ° - steady state, 3 g acceleration and 3 g deceleration downforce performance comparison between Mach 0.50 – 1.00 (top) and Mach 1.00 – 1.50 (bottom) 64
Figure 75: Percentage deviation in transient lift between Mach 0.50 and 1.00 (left) and Mach 1.00 and 1.50 (right) 64
Figure 76: Inverted RAE 2822 aerofoil, h/c = 1.00 and α = -2.79 ° - steady state, 3 g acceleration and 3 g deceleration drag performance comparison between Mach 0.50 – 1.00 (top) and Mach 1.00 – 1.50 (bottom) 65
Figure 77: Percentage deviation in transient drag between Mach 0.50 and 1.00 (left) and Mach 1.00 and 1.50 (right). 65
Figure 78: Inverted RAE 2822 aerofoil, h/c = 1.00 and α = -2.79 ° - steady state, 3 g acceleration and 3 g deceleration pitching moment performance comparison between Mach 0.50 – 1.00 (top) and Mach 1.00 – 1.50 (bottom) 66
Figure 79: Percentage deviation in transient pitching moment between Mach 0.50 and 1.00 (left) and Mach 1.00 and 1.50 (right). 66
Figure 80: Transient lift performance comparison for acceleration (left) and deceleration (right) 68
Figure 81: Transient drag performance comparison for acceleration (top) and deceleration (bottom) 68
Figure 82: Transient pitching moment performance comparison for acceleration (top) and deceleration (bottom) 69
Figure 83: Transient aerodynamic efficiency comparison for acceleration (top) and deceleration (bottom) cases 69
Figure 84: Transient case comparison against (a) steady state of the RAE 2822 aerofoil decelerating at: (b) -3 g, (c) -40 g, and (d) -176 g. Mach number contours are taken at Mach 0.70 71
Figure 85: Mach 0.70 coefficient of pressure plot comparison of steady state and transient deceleration results: (a) steady state, (b) -3 g, (c) -40 g, and (d) -176 g. 71

Figure 86: Mach 0.80 Mach number contour plot comparison of steady state and transient deceleration results: (a) steady state, (b) -3 g, (c) -40 g, and (d) -176 g. 72
Figure 87: Mach 0.80 density contour plot comparison of steady state and transient deceleration results: (a) steady state, (b) -3 g, (c) -40 g, and (d) -176 g. 72
Figure 88: Mach 0.80 coefficient of pressure plot comparison of steady state and transient deceleration results 73
Figure 89: Inverted RAE 2822 aerofoil, h/c = 0.50 – lift (left) and pitching moment (right) performance curves at different angles of attack. 74
Figure 90: Inverted RAE 2822 aerofoil, h/c = 0.50 – drag (left) and aerodynamic efficiency (right) performance curves at different angles of attack. 74

LIST OF TABLES

Table 1: Mesh independence study for the RAE 2822 Aerofoil.....22
Table 2: Validation results of an RAE 2822 aerofoil at AGARD "case 9" conditions.....22
Table 3: Variation in aerodynamic coefficients with increasing size of time step 25
Table 3: Summary of shock wave formation, shock wave propagation and lift inversions for an inverted RAE 2822 at different ground clearances. 42
Table 4: Shock locations on inverted RAE 2822 aerofoil at Mach 0.85 and different ground clearances. 44
Table 5: Comparison of the steady state and transient normalised shock locations (x/c) for the inverted RAE 2822 aerofoil at Mach 0.85. 55
Table 6: Comparison of normalised steady state and transient bow shock stand-off distances. 57
Table 7: Comparison of steady state and transient shock locations at Mach 0.70 and different rates of deceleration 70
Table 8: Comparison of steady state and transient shock locations at Mach 0.75 and different rates of deceleration 70
Table 9: Comparison of steady state and transient shock locations at Mach 0.80 and different rates of deceleration 70

NOMENCLATURE

m	Mass in kg
Vol	Volume in m^3
ρ	Density in kg/m^3
t	Time in seconds
$\boldsymbol{v}$	Velocity in m/s
$\boldsymbol{g}$	Acceleration in m/s^2
T	Static temperature in Kelvin
c_p	Specific heat capacity in J/kg.K
m_s	Mass source term
M_s	Momentum source term
E_s	Energy source term
C_L	Coefficient of lift
C_D	Coefficient of drag
C_m	Coefficient of pitching moment
C_p	Coefficient of pressure
h	Ground clearance distance between the aerofoil and the ground in m
c	Chord length in m
I	Incident shock wave
R	Reflected shock wave
M	Mach stem
θ	Angle of incident shock wave
θ_{max}	Maximum deflection angle
M_{cr}	Critical Mach number
M_b	Critical Mach number for the bow shock
δ	Bow shock wave stand-off distance

1 INTRODUCTION

1.1 Purpose of the Study

Develop a transient numerical model of an accelerating and decelerating flow field in order to investigate shock behaviour in ground effect, with relevance to the Thrust Supersonic Sonic Car (SSC).

1.2 Research Background

In September 1997, the Thrust SSC (Figure 1) set a new world land speed record of 714 mph (1149 km/h), exceeding the previous land speed record of 634 mph (1020 km/h) set by the Thrust 2. At a top speed of 763 mph (1228 km/h) the Thrust Supersonic Car (TSSC) became the first car to break the sound barrier (Figure 2) [3].



Figure 1: Thrust SSC in Black Rock Desert [3]



Figure 2: Aerial photo of the bow shockwave coming off the Thrust SSC [3]

Before attempting the world land speed record, extensive Computational Fluid Dynamics (CFD) simulations were carried out to prove the feasibility of building a supersonic car. To validate these results, a one twenty fifth scale model of the TSSC was tested using a rocket-powered sled on a railway in Pendine, Wales. The model was accelerated at 50 g from 0 – 800 mph in 0.8 s in order to replicate the pressures that would be present on the full scale TSSC [4]. Pressure taps were placed at multiple points along the length of the model and the pressure data was compared to the CFD pressure data. The pressure correlation between the CFD and Pendine test data is illustrated in Figure 3. The graph shows a high correlation between the two sets of data except for four outlying data points. The outliers all occurred at speeds close to the speed of sound M0.96, M1.05 and M1.08. This discrepancy could be as a result of transonic or supersonic flow features [5].

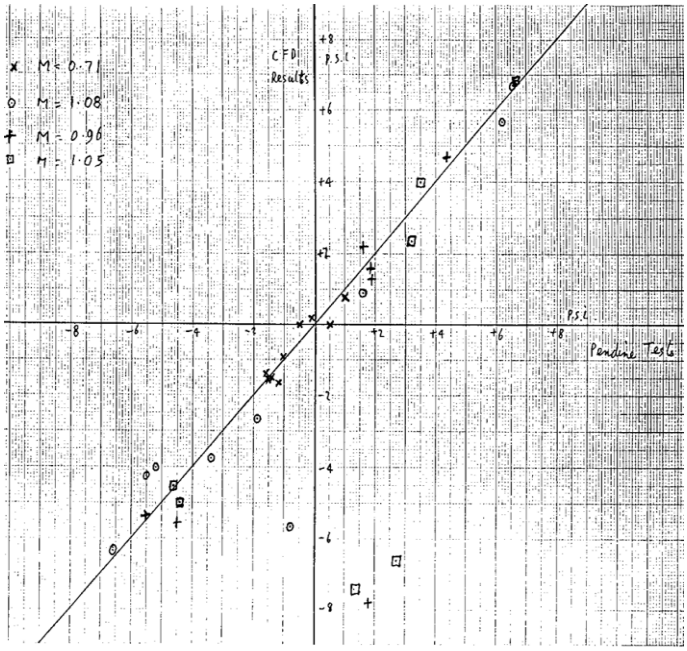


Figure 3: Correlation between CFD pressure results and Pendine test pressure readings at different Mach numbers [5].

Upon further inspection these outlying data points relate to pressure taps located near a large shock that developed across the center of the underbody as shown by Figure 4. The reason for this discrepancy is that the experimental results and simulation results predict slightly different positions of the underbody shock. The CFD predicts the shock to be behind the pressure tap while the experimental results indicate it to be in front [5]. These results were collected prior 1997 and unfortunately, most of the numerical and experimental results have been lost. Figure 3 as well as a couple of pressure measurements taken from the Pendine model were the only results recovered. The below CFD images were reproduced from the geometry of the TSSC model that was used in the Pendine tests.[1]

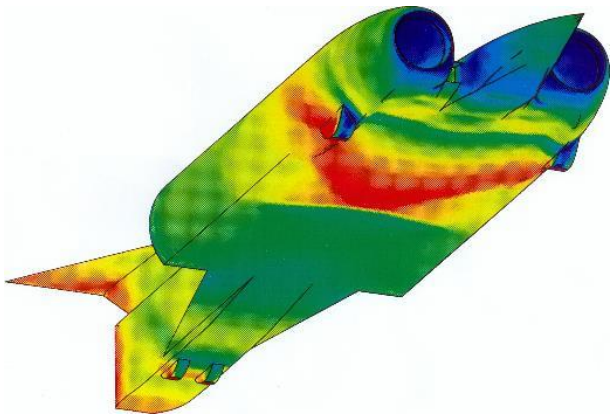


Figure 4: CFD pressure distribution across the lower surface of the Thrust SSC [5].

[1] The contour values were not provided by our collaborator at U. Swansea, Prof. B. Evans.

The CFD simulations were conducted by Prof. O. Hassan at the University of Swansea using a FLITE CFD modelling system, where an inviscid steady state solver was used [5]. The development of transonic flow features may not be accurately predicted by the steady state inviscid CFD models used.

The Bloodhound SSC (BSSC) is attempting to break the current world land speed record by exceeding 1000 mph (1609 km/h) approximately Mach 1.4. The CFD conducted on the Thrust SSC above, was vital in the development of the BSSC [4]. The TSSC and BSSC are unique examples of accelerating and decelerating transonic and supersonic flow near a stationary boundary and offer an ideal opportunity in future to obtain the validation data required to verify a numerical model of accelerating and decelerating supersonic flow near a stationary boundary. The BSSC was initially designed with programmable winglets to counter the variations in wheel loading as the aerodynamic forces and pitching moment vary with the velocity of the vehicle [4].

1.3 Research Motivation

Produce a transient CFD model of an accelerating and decelerating ground level supersonic flow field and analyse the shock wave formation and boundary layer interaction. Such a model could be used to study the flow field of other objects travelling at transonic and supersonic speeds in ground effect. For example ballistic projectiles, high speed trains [6], low flying aircraft, wing-in-ground (WIG) vehicles [7], maglev launched space vehicles [8] and tube transport systems.

Validation data in accelerating aerodynamics is extremely rare, as explained below. The present project will therefore work from validation in free flight and acceleration towards an understanding of ground effect in the transonic range. Based on the present work, a comparison with the Pendine rocket sled data would be possible in future work, providing a unique addition to the validation literature.

1.4 Problem Statement

The investigation of how acceleration and deceleration affect the development of flow around an object travelling at subsonic, transonic, and supersonic speeds, with close proximity to the ground.

1.5 Research Objectives

The following objectives have been set for this research:

- Determine the influence of ground effect on the flow field around an object and the resulting shock system as it approaches the ground in subsonic, transonic, and supersonic flow conditions.
- Investigate the effects of acceleration and deceleration on shock wave formation and development on an aerofoil travelling near a stationary boundary.

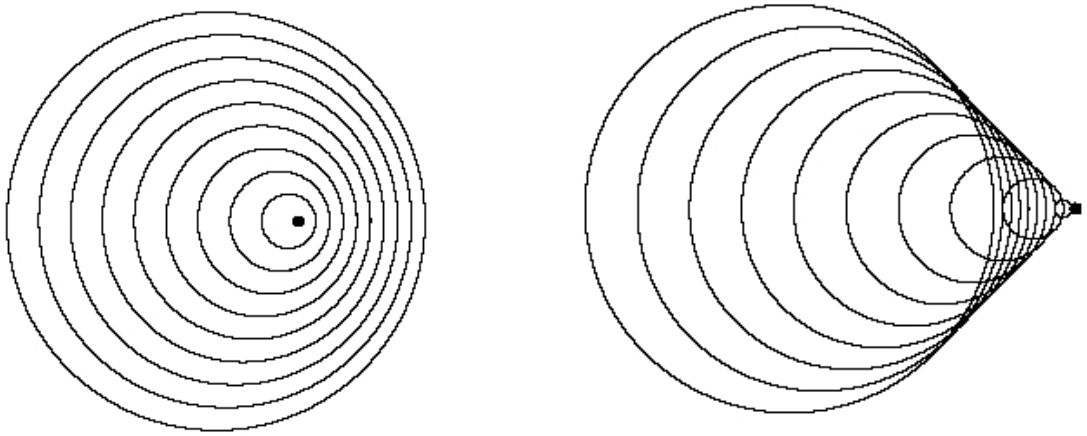
2 LITERATURE REVIEW

In order to break the world land speed record, the Bloodhound SSC accelerates and decelerates at up to 3 g and -3 g, to reach its top speed and then stops safely. In this case the flow field is constantly changing and there is no time for the flow to reach a steady state of motion. As the vehicle would be accelerating to and decelerating from supersonic speeds, it will experience subsonic, transonic, and supersonic flow conditions. Throughout this acceleration, the vehicle will be traveling in ground effect and it is possible that acceleration effects may contribute to unexpected loads on the vehicle.. As such, any disruption to the downforce or pitching moment would be extremely dangerous and potentially catastrophic.

The research question is to determine how rapid acceleration and deceleration affects the shock formation on lifting bodies in transonic and supersonic ground effect. In turn, how would these effects impact on the aerodynamic performance and stability of the lifting body?

2.1 Unsteady flow effects due to acceleration and deceleration

Early work considered the flow field around a particle moving at constant velocity or steady state velocity can be described by Figure 5. The particle on the left is travelling to the right at a constant subsonic velocity while the particle on the right is traveling at a constant supersonic velocity.



(a) **(b)**

Figure 5: A particle moving at a) constant subsonic velocity and b) constant supersonic velocity [9].

Now consider a particle accelerating from subsonic to supersonic velocities as per Figure 6; the resulting flow field would consist of subsonic effects propagating forward at the speed of sound and supersonic effects caused by the shock waves catching up and over taking the subsonic effects. As the particle then decelerates from the supersonic to subsonic conditions,

the shock waves continue to propagate slowly dissipating as they progress; with the particle now falling behind as it continues to decelerate [9].

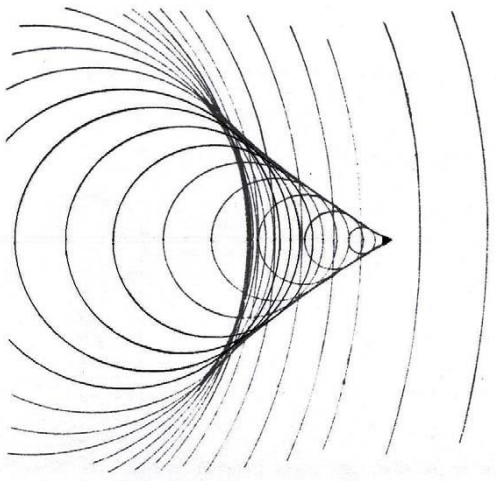


Figure 6: A particle accelerating from subsonic to supersonic velocity [9].

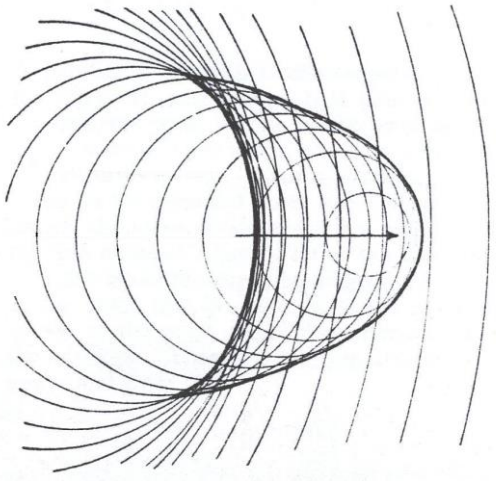


Figure 7: An accelerated particle decelerating from supersonic velocity to subsonic velocity [9].

By comparing the two cases, it is evident that the flow field at a chosen constant velocity will yield different results to the flow that has been accelerated or decelerated to attain that same chosen velocity. The extent to how the differences in the constant velocity case and acceleration and deceleration cases impact on the formation and dissipation of the resulting shock system were investigated.

Research over the last 15 years has identified that the above differences in the steady and unsteady case are primarily due to either transient flow history or inertial effects [10], [11]. Transient flow effects arise from the fact that when a body is accelerating from one state to another the flow field does not have sufficient time to develop to a flow field that would be present at the higher steady state or constant velocity conditions. Instead, the developing flow field at a given velocity resembles that of a lower constant velocity. As the flow continues to accelerate the developing flow is unable to reach the new flow conditions and the difference between the developing flow and constant velocity flow increases.

Transient studies conducted on a RAE 2822 aerofoil at free flight conditions revealed that the accelerating aerofoil featured a reduction in lift and an increase in drag in the subsonic region, while for the decelerating aerofoil the inverse was true. The effects in the transonic and supersonic regions fluctuated, with the biggest differences featuring in the transonic region [10].

The inertial effects of acceleration are the changes in the apparent mass and inertia of a body due to its motion. These effects can have a significant impact on the aerodynamics of a wing, especially at high speeds and angles of attack. One of the main inertial effects of linear forward acceleration is the increase in and movement of the stagnation pressure on the leading edge of a wing or aerofoil [12]. Another inertial effect is the change in the pressure distribution over the wing due to the acceleration-induced flow. This can affect the stability and control of the wing, as well as the generation of shock waves and wave drag [10]. A third inertial effect is the variation in the Reynolds number due to the acceleration of the wing. This can alter the boundary layer behavior and the transition from laminar to turbulent flow, which can affect the skin friction drag and the heat transfer on the wing [13].

During the uniform acceleration of an RAE 2822 aerofoil, inertial effects were shown to dominate the subsonic and transonic flow field right up until the bow shock forms ahead of the aerofoil. Thereafter, the flow history effects dominate. The same was true for uniform deceleration, but with the inertial effects dominating further into the subsonic region as the surface shocks over take the aerofoil and propagate ahead of the aerofoil [12].

2.2 Transonic Flow

The transonic flow regime is considered to exist between Mach 0.7 and 1.2 and is dominated by both subsonic and supersonic flow physics. This means that transient flow fields are highly non-linear and difficult to model mathematically. However, with the recent use of acceleration models in CFD, more light has been shed on this area of flow research. All CFD models require experimental results in order to validate the obtained numerical results.

Validation data is the next major obstruction to analysing accelerating transonic flow. The best data currently available is from a Japanese ballistic range [14] for a decelerating sphere. Available rocket sled data appears to be limited to the test results conducted at the Pendine facility on a $1/25^{th}$ scale model of the Thrust SSC.

In some applications, supersonic and subsonic flow regimes may be modeled as inviscid, as the inertia and pressure effects dominate the viscous effects. This is true for most of the bulk flow field. However, in this research the viscous effects on the transonic flow are an important consideration, as the flow of interest is in the gap between the object and the ground, and separation and boundary layer effects may influence the position of shock wave and the type of shock system.

2.3 Shock Wave Theory

2.3.1 Normal Shock Waves

A normal shock is an irreversible discontinuity in an otherwise ideal gas flow, where the upstream and downstream velocity vectors of the flow remain perpendicular to the shock. Although the flow does not change direction, there is an almost discontinuous change in the magnitude of the flow velocity, pressure, temperature and density across the shock as illustrated by Figure 8 [15].

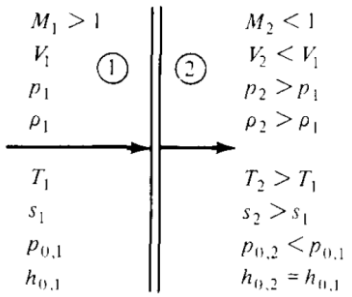


Figure 8: Qualitative illustration of the variation of flow field properties across a normal shock wave [15]

2.3.2 Oblique Shock Waves

An oblique shock wave occurs when the downstream flow makes an oblique angle with the upstream flow; this can occur when supersonic flow is forced to turn into or away from itself. When a corner in the wall turns towards the flow direction in a concave corner, a single discontinuous shock wave is formed, while a series of oblique expansion waves occur as the wall turns away from the flow direction or expands over a convex corner forming an expansion fan – as illustrated in Figure 9. Unlike the single discontinuous oblique shock, the flow properties change continuously throughout the expansion fan. For the flow to remain parallel to the wall, the flow is rotated by the deflection angle θ as it crosses the oblique shock wave or expansion fan [15].

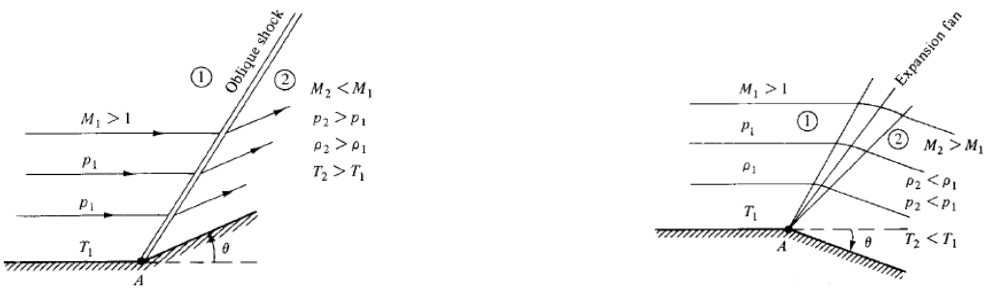


Figure 9: Supersonic flow over a (a) concave corner and a convex corner (b) causing a single oblique shock wave and expansion fan respectively [15].

2.3.3 Detached Shock Waves

In the previous section, the oblique shock and expansion fan are considered attached shocks as in both cases the shock originates from the corner. A detached shock wave forms when the deflection angle θ is too large for the flow to rotate parallel to the wall via a straight oblique shock wave. As a result, a curved and detached shock wave forms ahead of the corner to rotate the flow – as illustrated on the right of Figure 10 (a). The maximum deflection angle for the flow to remain attached is defined as θ_{max} for a given Mach number. The maximum allowable deflection angle increases as the Mach number of the flow increases. The same physics apply for supersonic flow over a wedge, Figure 10 (b), where the shock waves are attached to the nose of the wedge and detach further upstream when the deflection angle of the wedge is greater than maximum deflection angle: $\theta > \theta_{max}$.

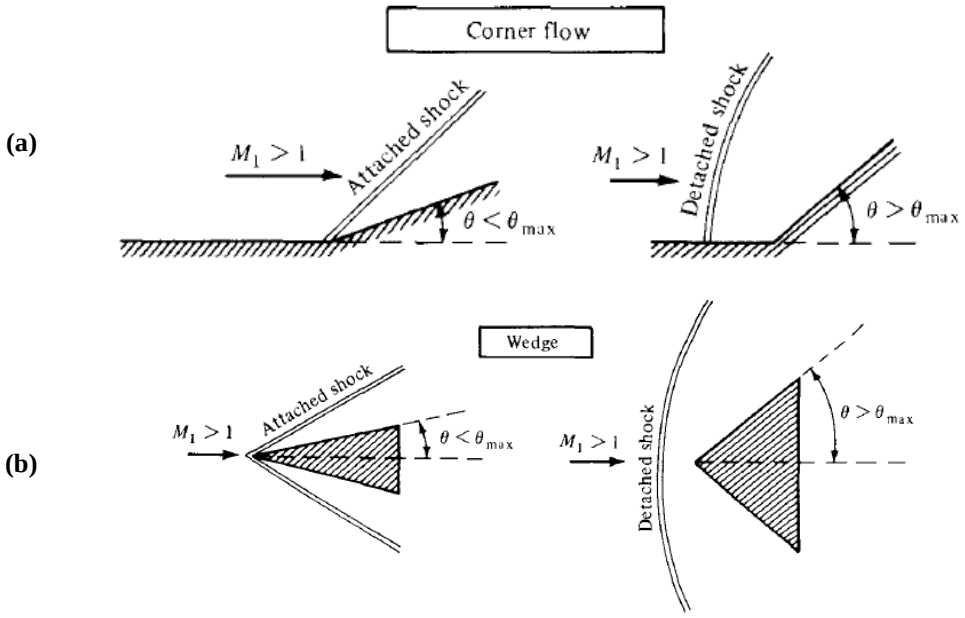


Figure 10: Attached and detached shock waves for corner flow and around a wedge [15].

In the case of a blunt body, where the leading edge is curved and does not have a defined corner at the leading edge, a curved detached bow shock wave is formed upstream. The bow shock is displaced from the nose of the body by distance, δ, which is defined as the shock detachment distance, or stand-off distance, as shown in Figure 11.

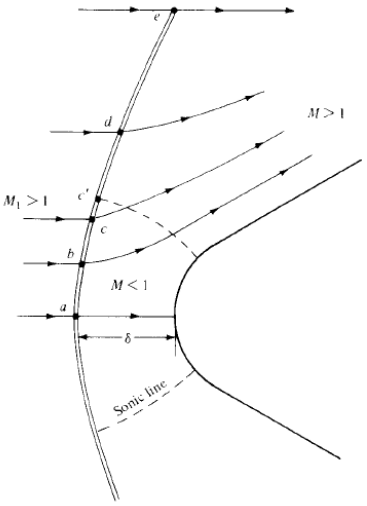


Figure 11: Supersonic flow over a blunt body [15].

At point ‘a’ in Figure 11, the downstream and upstream flow is perpendicular to the shock wave and thus a normal shock wave occurs. The shock wave starts to curve and weaken as it moves away from this point. The upstream flow coming from point ‘a’ decelerates as it approaches the wall and impacts perpendicularly to the leading edge, thus stagnating at this point. Flow is deflected along the wall from this point. As the flow diverts around the blunt body, the flow accelerates as it moves downstream of the nose and eventually becomes supersonic again, hence forming a small region of subsonic flow at the nose of the body [15].

2.3.4 Shock Formation on an Aerofoil

Consider an aerofoil in subsonic flow, illustrated in Figure 12, as the flow passes over the upper surface of an aerofoil it expands and starts to accelerate. If the subsonic free stream velocity is high enough, this acceleration can cause the flow to become locally supersonic, forming a region of supersonic flow. The velocity at which the flow over the aerofoil first becomes sonic is considered the critical Mach number and varies depending on the aerodynamic profile of the aerofoil. Downstream of this supersonic region of flow, a normal shock wave forms as the flow returns to subsonic conditions. As the free stream velocity increases, a shock wave on the lower surface of the aerofoil starts to form. Increasing the velocity even further causes both supersonic regions to grow and the normal shocks move towards the trailing edge of the aerofoil. As the free stream flow becomes supersonic, a bow shock forms at the leading edge. Figure 13 illustrates the regions of separated flow that form behind the normal shock wave when the adverse pressure gradient near the surface is large enough to cause reversed flow [15].

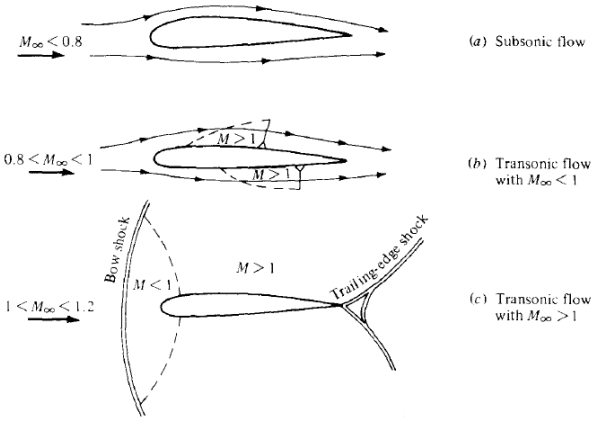


Figure 12: Shock wave formation on an aerofoil [15].

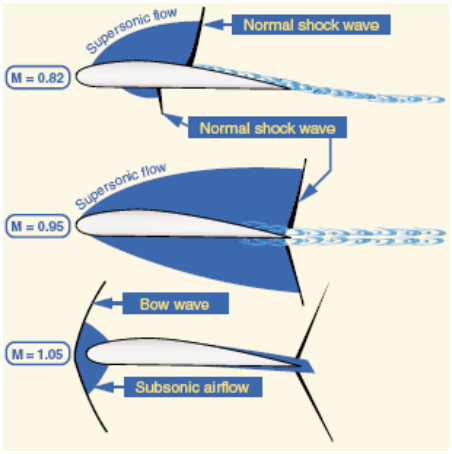
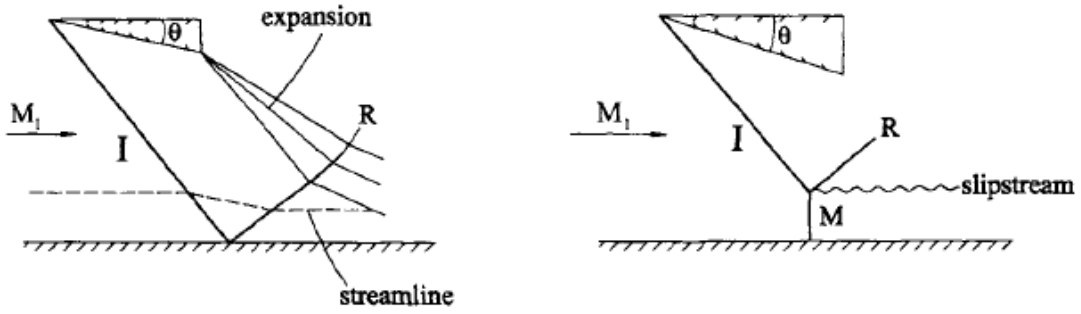


Figure 13: Shock wave formation on an aerofoil with flow separation [16].

2.3.5 Shock Wave Reflections

An important consideration when investigating objects traveling supersonic near the ground is the way in which the shock waves that develop from the body interact with the ground. In the case of an oblique shock wave developing on a wedge, as shown in Figure 14, two shock patterns are possible. The first case, on the left, is a regular reflection where the incident wave labeled, **I** rotates the flow down towards the ground. For the flow to remain parallel to the wall, the reflected shock **R** forms to rotate the flow upwards and parallel with the wall again – as illustrated by the dashed streamline.

The second case is a Mach reflection, where the wedge angle is larger, and the incident shock is too strong for a regular reflection to rotate the flow parallel to the surface. As a result, a Mach stem **M** is created normal to the surface, ensuring the flow remains parallel to the wall, with the incident and reflected shock forming above the Mach stem. This three-shock system is called a lambda shock. The reflected shock and Mach stem have different strengths and as a result, the velocities of the flow behind these shock waves are different. The viscous interaction between these two flow regions of differing velocities results in the formation of a slipstream, separating the different regions. The streamline initiates from where these three shocks meet, known as the triple point [17].



Regular reflection (RR) **Mach reflection (MR)**

Figure 14: Regular and Mach oblique shock reflections [17].

Transitions are summarised by Matheis and Hickel [18].

2.3.6 Boundary Layer Interaction

An important consideration is what happens as a shock wave interacts with a boundary layer. Two types of interaction are possible and depend on whether separation occurs at the wall. Separation occurs when the adverse pressure gradient is large enough to cause the flow near the wall to reverse in direction, thus creating a separation bubble of rotational flow. Figure 15 illustrates a boundary shock wave interaction without separation and how the boundary layer starts to decelerate the normal shock wave as it approaches the wall [17].

As Figure 16 illustrates, the flow near the wall has reversed in direction as it flows over the curved surface, forming a small region of separated flow. This region of separated flow forces the flow to turn in on itself and an oblique shock wave (C1) is formed as a result. The oblique shock propagates to the normal shock wave (C3) and by compatibility conditions a third trailing shock (C2) is formed as the flow transitions back to subsonic conditions. These three shocks form a lambda shock system and the separated flow causes a significant increase in drag [17].

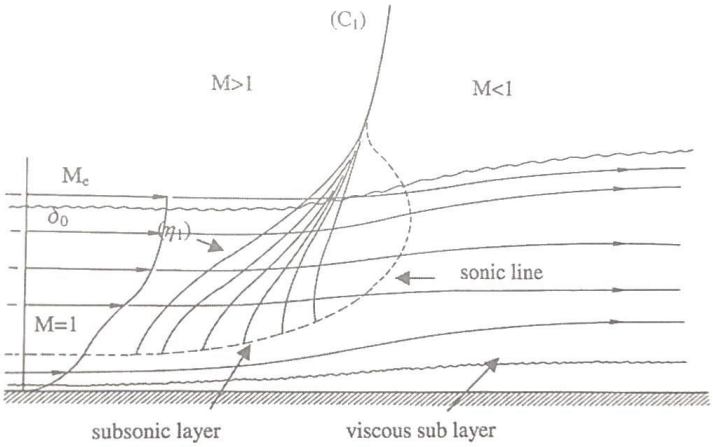


Figure 15: A normal shock wave without boundary layer separation. Ben-Dor *et al.* (2001) [17]

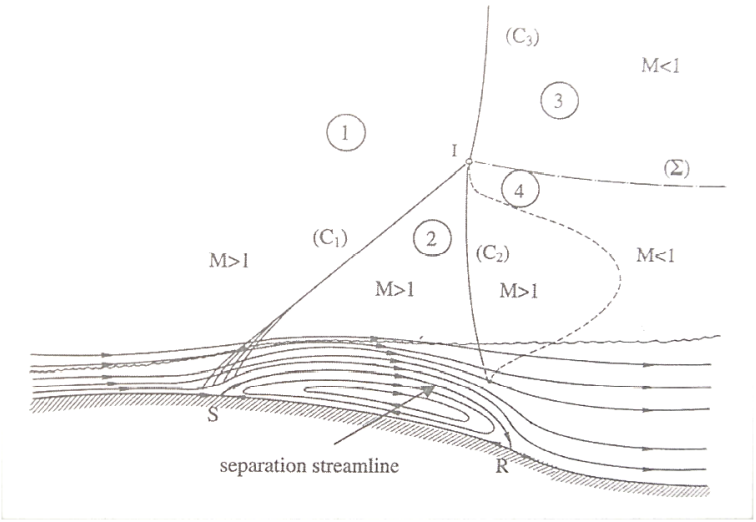


Figure 16: A normal shock wave with boundary layer separation, forming a lambda shock. Ben-Dor *et al.* (2001) [17]

The detailed modelling of such a system has not been a focus of this broader research but could be included in further work [17].

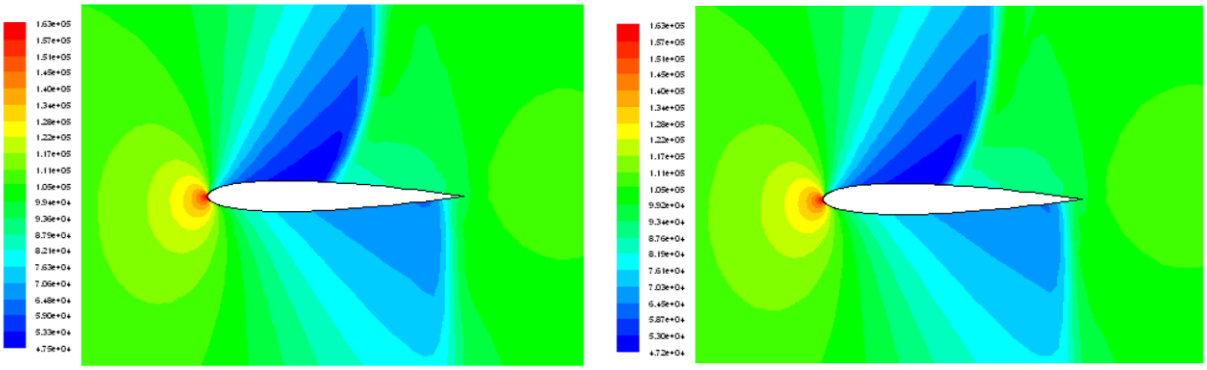
2.4 Numerical modelling techniques

The CFD software chosen to simulate the flow is Ansys Fluent and the following techniques were recommended, by Fluent, to investigate the constant velocity and accelerating flow fields. Roohani 2011, investigated the unsteady aerodynamics of accelerating bodies at free stream conditions by using and expanding upon these techniques. The research focused primarily on the aerodynamics and shock wave dynamics of bi-convex and RAE 2822 aerofoils accelerating and decelerating at an extreme and moderate magnitude of 106 g and 8.845 g respectively [19].

The current research builds on this research by using the same techniques and user-defined function (UDF) to investigate the transient effects of acceleration and deceleration in combination with ground effect and the orientation of the RAE 2822 aerofoil.

2.4.1 Techniques for constant velocity cases

The flow around an object can be modeled numerically by either moving the body through a stationary fluid in an inertial frame or by moving the fluid in the opposite direction over the stationary body to produce the equivalent result. The former case is known as the moving reference frame technique and can be set up by moving the object and the numerical grid simultaneously at the chosen velocity, while keeping the fluid stationary at the upstream and ground boundaries. Alternatively, the model and the grid must be set up such that the object is kept stationary and the fluid is moved around the object in the non-inertial relative frame. When modelling an object moving at constant velocity in compressible flow in the relative frame, pressure-far-field boundary conditions are appropriate. With this method, the free stream velocity, which may be a function of time, is set at the boundaries of the domain. Thus, the flow field generated by the relative frame technique matches that of the moving reference frame technique: as shown by comparing the following pressure plots generated by each technique, in Figure 17.



(a) **(b)**

Figure 17: Pressure flood plot comparison of an aerofoil moving at M0.85; modelled using (a) the moving reference technique and (b) the pressure-far-field technique [19].

The above results were obtained using the CFD solver Fluent for both techniques. These results were for an aerofoil moving at constant velocity.

2.4.2 Technique for accelerating objects in compressible fluids.

To model acceleration in a non-inertial reference frame, the pressure-far-field boundary condition technique can no longer be used without source terms. The reason for this is that the velocity changes at the boundary propagate through the fluid at the speed of sound. Therefore, as the flow develops, a pressure gradient is set up through the flow field that is not representative of the flow. An example of this pressure gradient is given by Figure 18.

The flow is now transient and the boundary velocity increases and decreases instantaneously as the flow accelerates and decelerates. In order for the pressure-far-field technique to be used and simulate the physical case in reality; the velocity of the entire flow field must be increased uniformly and not just at the boundary. This uniform acceleration can be achieved by applying a UDF that incrementally accelerates each particle in the flow field at every time step. This model can be constructed by including source terms into the UDF.

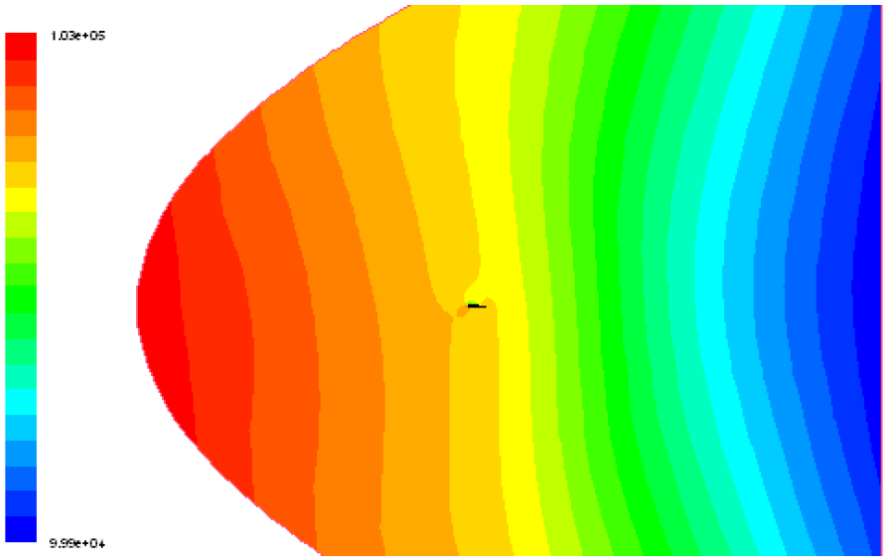


Figure 18: Pressure flood plot produced by the constant acceleration of the fluid at the upstream pressure-far-field boundary [19].

These source terms are based on the mass, momentum and energy equations and were derived by considering the rate of change of these properties at each point in the flow [19]:

Mass source [kg/m^3/s]

$$m_s = \frac{dm/dt}{Vol}$$

$$= \frac{d\rho}{dt}$$

Momentum source [N/m^3]

$$M_s = \frac{d(mv)/dt}{Vol}$$
$$= \frac{d(\rho.Vol.v)/dt}{Vol}$$
$$= \frac{d(\rho v)}{dt}$$
$$= \rho\left(\frac{dv}{dt}\right) + v\left(\frac{d\rho}{dt}\right)$$

Energy source [W/m^3]

$$E_s = \frac{de/dt}{Vol}$$
$$= \frac{d\left(mc_pT + mv^2/2\right)/dt}{Vol}$$
$$= \frac{d\left(\rho c_pT + \rho v^2/2\right)}{dt}$$
$$= \rho c_p\left(\frac{dT}{dt}\right) + Tc_p\left(\frac{d\rho}{dt}\right) + \frac{1}{2}v^2\left(\frac{d\rho}{dt}\right) + \rho v\left(\frac{dv}{dt}\right)$$

In reality, the object is being accelerated and not the fluid around it. Therefore, in order to correctly model the flow physics, the acceleration terms in each of the above equations were imposed on the fluid. It is also important to note that the velocity term in the above equations refer to the velocity of object relative to the ground or in this case, the ground relative to the stationary object. All other property changes develop in the flow naturally; as they would in reality. Hence, by retaining only the terms with acceleration, the above source term equations simplify down to:

Momentum source [N/m^3]

$$M_s = \rho\left(\frac{dv}{dt}\right)$$

Energy source [W/m^3]

$$E_s = \rho v\left(\frac{dv}{dt}\right)$$

By including the above source terms to the relative frame technique above, the flow field throughout the domain is now simultaneously accelerated, as can be seen in Figure 19. The same domain was used as the case in Figure 18, but the pressure distribution is now uniform throughout the domain, except for the localized effects of the aerofoil. The acceleration and deceleration effects can now be more accurately simulated using this technique. This method of acceleration is known as the source term technique [20] and has been validated and verified by experimental data and a moving reference frame technique developed to study decelerating supersonic flow fields [21].

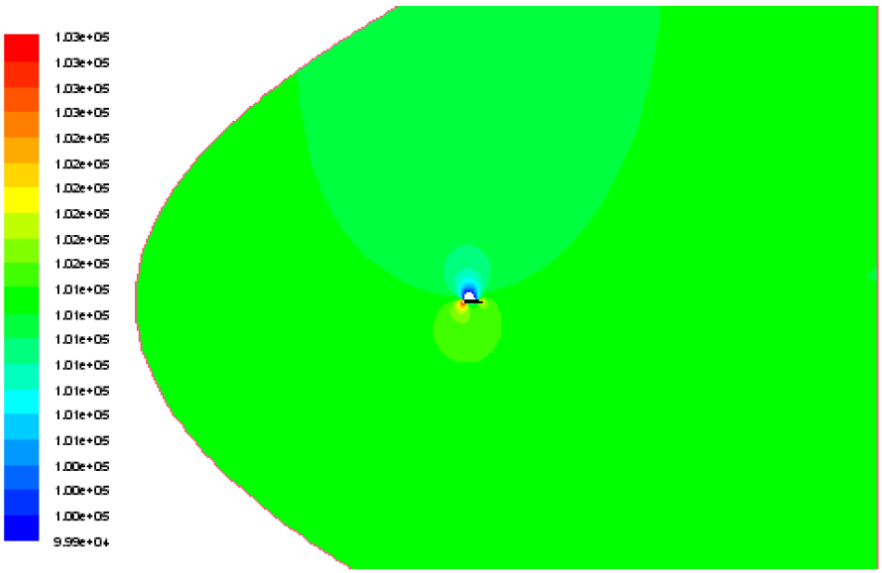


Figure 19: Pressure flood plot of a uniformly accelerated fluid using the pressure-far-field technique with source terms [19].

2.5 Ground Effect

In free flight the flow field around the aerofoil is unrestricted. With increasing proximity to the ground, the flow field below the aerofoil is altered as the phenomenon of ground effect comes into consideration. Various studies have been conducted on the aerodynamic performance of lifting bodies near a stationary boundary, both for upright wings or aerofoils producing positive lift and inverted wings or aerofoils producing negative lift or downforce [22], [23], [24], [25], [26], [27]. In both cases it was shown that the increased proximity to the ground enhanced the lift and downforce produced by the aerofoil. However, for the upright aerofoil the increase lift was due to the rise in pressure of the constricted flow under the aerofoil, while for the inverted aerofoil the flow under the aerofoil is accelerated increasing the suction pressure on the lower surface of the aerofoil [28].

Prior research has been conducted on aerofoils in ground effect travelling at subsonic [22], [29], [30], [31], [32], [33], transonic [34], [35] and supersonic [36], [37], [38] speeds. The shock formation on the lower surface of a RAE 2822 aerofoil was shown by Doig *et al.* to have a destabilizing effect on the pitching moment and a significant loss in aerodynamic efficiency once the shock was formed. Aerodynamic efficiency is defined as the ratio of the lift produced by an aerodynamic body or aerofoil to the aerodynamic drag caused by that body or aerofoil moving through the air [15]. Proximity with the ground also lowers the critical Mach number, causing the shock on the lower surface to form earlier and further

decrease the aerodynamic efficiency and lift-producing range of the aerofoil [34]. The above studies were all conducted at steady state conditions and the transient effects from acceleration and deceleration were not considered.

Previously published investigations, by the present author, on a NACA 0012 [1] and RAE 2822 aerofoil [2] accelerating at 176 g in ground effect confirmed that the accelerating flow field resembled the flow field of a lower constant velocity case. Two ground clearances were considered in the RAE 2822 aerofoil investigation to show that the reduced ground clearance increased the pressure under the aerofoil and delayed the movement of the bow shock and its reflection under the aerofoil. The NACA 0012 study also identified that viscous effects slightly delayed the bow shock wave as it interacted with the ground ahead of the aerofoil. This investigation combines both studies by further analysing the influence of acceleration, deceleration and ground effect on shock location and the resulting aerodynamics.

3 NUMERICAL MODELLING

The CFD software chosen to simulate the flow is Ansys Fluent. The pressure far field technique was used to set the free stream velocity for both the steady state and transient numerical simulations. In order to accurately capture the shock formation and location, a viscous, density-based solver was used to account for the compressibility and viscosity of the fluid. The fluid was modelled as an ideal gas and the Sutherland law was used to calculate the viscosity changes with temperature.

The main velocity range of interest is that of the TSSC and BSSC, from Mach 0.05 up to Mach 1.40; however, to further understand the influence of ground effect this was extended up to velocities of Mach 3. Due to the complexity and computational resources required to study the full TSSC geometry, the study focuses mainly on the shock development on and aerodynamics of a supercritical RAE 2822 aerofoil. The RAE 2822 aerofoil was chosen due to the large extent of literature and validation cases run on this aerofoil.

The following model of a 2-D RAE 2822 aerofoil was set up and an example of the domain used is shown in Figure 20. To allow for any local flow field effects to dissipate and reach far field conditions, the domain was set with 15 chord lengths above the aerofoil and 20 chord lengths before and after the aerofoil.

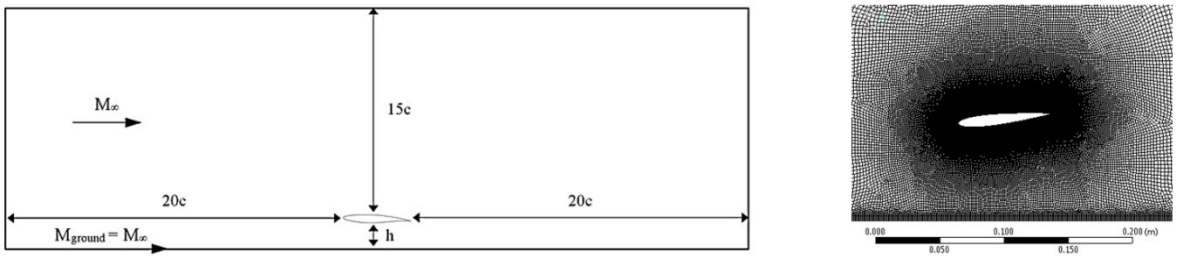


Figure 20: Domain, boundary settings and meshing technique used for all the aerofoil models.

The domain was set up with a moving ground wall below the object. Different ground clearances were used and compared against a free flight (no ground effect) case to investigate the influence ground effect had on the flow field and shock wave development. The ground clearance (h) was reduced from one characteristic chord length (c) down to 5 % of the chord. The chord was scaled up from the AGARD case 9 geometry by a factor of 5 and set at 3.05 m to increase the Reynolds numbers to a more practical value that is reflective of real-world flight conditions. From this point forward the ground clearance is referred to by the ratio, h/c, for example for a ground clearance of 5 % of the chord length, h/c = 0.05. Inflation layers

were applied to the walls of the aerofoil to ensure y-plus values were either below 1 or above 30. The sizing for the elements closest to the surface of each model is based on the distance covered by the flow field in a single time step at the highest velocity considered at Mach 2.4. For consistency the same mesh is used for the steady state and transient analysis. With the final time step used being $5x10^{-6}$ s, the aerofoil has an edge sizing of 4.9 mm (0.16 % c) along the profile of the aerofoil and the immediate ground plane under the aerofoil. The sizing was also bias slightly with smaller elements being used near the nose of the aerofoil and larger elements towards the tail.

The following sign conventions were used in this investigation: right as the positive direction of the horizontal flow over the aerofoil, lift as the positive normal force upwards, downforce as the negative normal force downwards, drag as the positive tangential force to the right, and angle of attack and pitching moment as positive in a nose-down or anti-clockwise direction.

3.1 Steady state flow analysis

For the steady state cases, the velocity was incremented by Mach 0.1 through the subsonic region, Mach 0.05 through the transonic and then Mach 0.1 again in the supersonic. Where further detail of the development of the flow and shock waves was required, these intervals were reduced, and the mesh refined to better understand and capture the flow physics. The flow Mach number was set at the pressure far field and the corresponding velocity was set at the ground wall, with the velocity of the aerofoil set to zero.

3.2 Transient flow analysis

In order to investigate the acceleration and deceleration effects, non-inertial reference frame, transient simulations are necessary to model the flow. Fluent is unable to model non-inertial reference frames and user-defined functions (UDF's) were required to model the acceleration. The pressure-far-field technique and the added momentum and energy source terms (derived in section 2.4.2) were used to model the flow. This UDF is interpreted by Fluent and works in conjunction with the solver to uniformly increment or decrease the velocity of the fluid throughout the domain and apply the momentum and energy source terms at every time step. Multiple iterations at each time step were considered, in order to correctly simulate the flow physics and allow for adequate convergence of the fluid properties for each time step. The flow is accelerated from Mach 0.20 up to Mach 2.40 and snapshots of the flow were taken at

various speeds and compared against the constant velocity results to determine the acceleration effects. The same procedure was adopted to analyse the deceleration effects.

Three different accelerations were used in the transient study. An extreme acceleration of approximately 176 g based on surface-to-air and air-to-air missiles, a moderate acceleration of 40 g taken as the average acceleration and deceleration of the Pendine rocket sled and a relatively low acceleration of 3 g applicable to fighter jets and the Bloodhound and Thrust SSC vehicles.

3.3 Applying the Source Terms

The source terms were applied to the flow by a UDF that features a series of programming loops that continuously update the Mach number, momentum, and energy of the flow, as it accelerates and decelerates. A function was defined to increase or decrease the Mach number of the flow at every time step. Next, functions for updating the momentum and energy in each element of the fluid were defined using the simplified momentum and energy source term equations derived in section 2.4.2.

As only constant acceleration and deceleration cases were considered, the momentum source term remained constant and only the energy source term was updated with each time step. An example of the code used to update this energy source term for constant acceleration is given in Appendix A.

3.4 Validation

Due to the scarcity of validation models for acceleration and deceleration models for an aerofoil in ground effect, the validation has been broken into three phases. The first phase was to validate the RAE 2822 aerofoil model against experimental and numerical studies at free flight and steady state conditions. In the second phase, ground effect was introduced, and these results were compared against ground effect studies of the aerofoil at steady state conditions. The last phase was the use of individually validated source term and moving ground plane models to produce the transient acceleration and deceleration results.

3.4.1 Mesh Independence

The RAE 2822 validation model was set to match the geometry and parameters of case 9 of the AGARD experimental study [39]: Mach 0.73, a wind tunnel corrected angle of attack of 2.79° [34] and Reynolds number of 6.5 x 10^6 (based on a chord length of 0.61 m). Four meshes were considered for the RAE 2822 aerofoil and the results have been summarized in Table 1.

Table 1: Mesh independence study for the RAE 2822 Aerofoil

Mesh	Coarse	Intermediate	Fine	Intermediate mesh with adaption
Elements	~ 600 000	~ 1 800 000	~ 3 200 000	~ 2 400 000
C_L	0.820	0.816	0.815	0.815
C_D	0.0186	0.0182	0.0176	0.0178

The intermediate mesh with adaption was chosen as the results were comparable to the finer meshes and overall, more efficient, especially when used for the transient runs. Grid adaptions were then applied to improve the resolution of the shock waves.

3.4.2 Steady state free flight conditions

The results from the adapted intermediate mesh were validated against the experimental data from case 9 of the AGARD experimental study [39] and the Validation 11 case provided by Fluent for a transonic flow over an RAE 2822 aerofoil. The meshes of the Validation 11 case are discussed in further detail by Coakley [40]. The results are summarized in Table 2 and showed good correlation with the experimental and numerical data.

Table 2: Validation results of an RAE 2822 aerofoil at AGARD "case 9" conditions.

	Mesh	Model	Lift (C_L)	Drag (C_D)	Shock (x/c)
	Adapted mesh	Spalart-Allmaras	0.815	0.0178	0.53
		Experiment	0.803	0.0168	0.52
Validation 11	Hybrid	Realizable k-ε	0.825	0.0181	0.52
		SST k-ω	0.781	0.0164	0.50
		Spalart-Allmaras	0.815	0.0171	0.52
	Quadrilateral	Realizable k-ε	0.828	0.0181	0.52
		SST k-ω	0.782	0.0163	0.50
		Spalart-Allmaras	0.817	0.0170	0.52

3.4.3 Turbulence models

The Spalart-Allmaras turbulence model was shown to be the most applicable model for the free-stream transient study [41] and with reference to Table 2 this proved to be the case in this investigation as well. Out of the three turbulence models considered the Spalart-Allmaras results on average had the lowest deviation from the experimental results.

3.4.4 Transonic flow features in ground effect

The numerical results obtained on an aerofoil in increasing ground effect are validated against various sources for subsonic, transonic, and supersonic flow by comparing the results and shock structures. Subsonic results were validated against research conducted by Vogt *et al.* on subsonic upright and inverted aerofoils at various ground clearances [28]. Higher transonic and supersonic velocities were validated against the research on transonic and supersonic ground effect and shock reflections investigated by Doig [42]. For example, the correlation in shock structures found in the transonic study conducted by Doig *et al*. are illustrated by Figure 21 to Figure 23 at two different Mach numbers and clearances.

The moving ground wall model used in this investigation and by Doig *et al.*, shows strong correlation with the mirror-image method that features a symmetrical ground plane under the aerofoil and experimental data, where a moving conveyor belt was set-up underneath the stationary aerofoil to represent the moving ground [43].

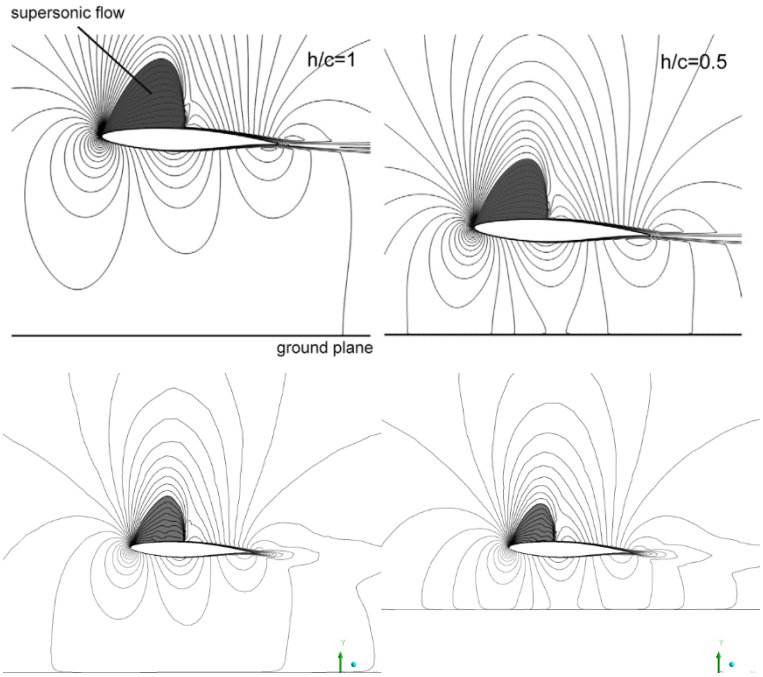


Figure 21: AGARD case 9 validation with ground effect, validation model (bottom) against validated results from literature (top). Ground clearances of h/c = 1.00 (left) and 0.50 (right) [34].

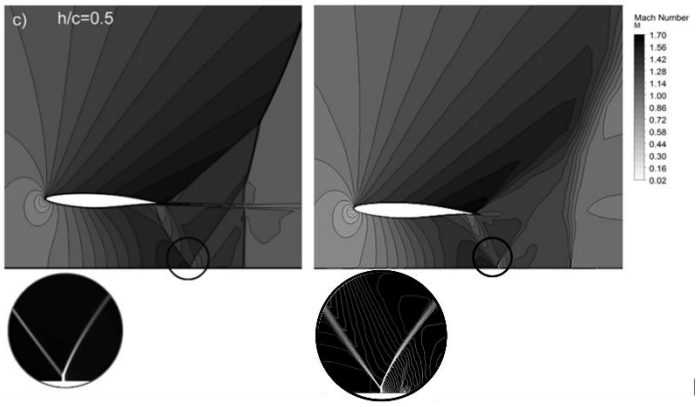


Figure 22: Comparison of the Mach number contours produced by the validation model (right) against existing validated research (left, [34])

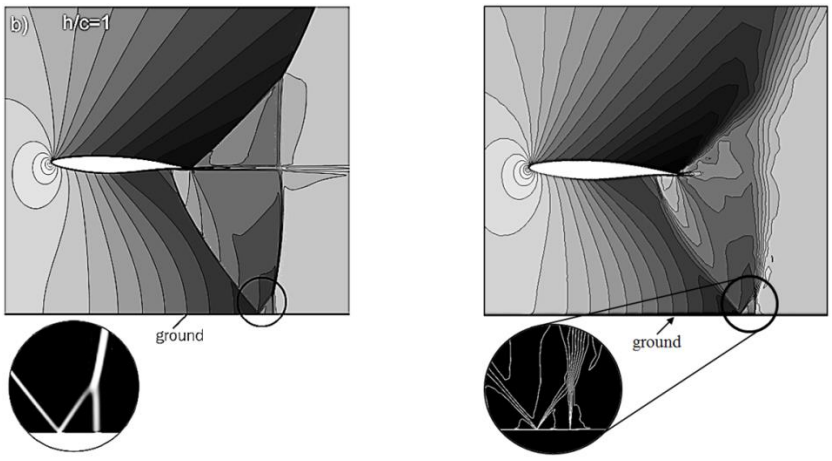


Figure 23: Comparison of the Mach number contours produced by Doig *et al.* (2012) left and the validation model (right).

3.4.5 Time step independence

For each transient simulation the time step size was estimated by calculating the approximate time for the flow to pass through an element on the surface of the geometry at the maximum flow velocity for the case being considered. For the RAE 2822 aerofoils the maximum speed considered for the transient runs was Mach 2.40. With such a large speed range the overall simulation run time became a factor in the sizing of the time step. The time step size chosen for the maximum acceleration case of 176g was $5x10^{-6}$ s, as this led to a stable solution and allowed 4000 time steps per Mach 0.05 increase in the velocity of the flow. For the 3g acceleration cases, the time step was increased to 3.69 $x10^{-5}$ s. The much lower acceleration allowed for a more stable solution and the larger time step significantly decrease simulation run time. For the 40 g acceleration, the considered speed range was from Mach 0.05 up to Mach 1.60 and the most efficient time step size was 4.9 x 10^{-5} s (8000 timesteps per Mach 0.05 interval). For each time step a maximum of 100 iterations was required for the solutions to converge.

To improve computational efficiency and evaluate time step independence, the sensitivity of the aerodynamic coefficients to time step size was evaluated using the 3 g acceleration case of the inverted 2-D RAE 2822 aerofoil and the results are summarized in Table 4. In each case the aerofoil was accelerated from Mach 0.20 to 0.25. The coefficient of drag featured the greatest sensitivity, -1.72%, to the increase in time step size followed by pitching moment, -0.65%, and then lift, -0.35%. A strong correlation was shown across the cases; however, the larger time steps lead to minor fluctuations in the aerodynamic performance and in some of the cases the transient solution diverged. The smallest time step was chosen in order to minimize these fluctuations and increase the stability of the transient solution. As such, the simulations were computationally expensive and had to the run over larger periods of time.

Table 3: Variation in aerodynamic coefficients with increasing size of time step

Case	Time steps per Mach 0.05	Time step size (s)	C_l	C_d	C_m	ΔC_l	ΔC_d	ΔC_m
1	16000	3.69E-05	-0.9321	0.0144	-0.1222	0.00%	0.00%	0.00%
2	8000	7.37E-05	-0.9301	0.0144	-0.1218	-0.21%	-0.58%	-0.36%
3	4000	1.47E-04	-0.9289	0.0143	-0.1215	-0.35%	-1.15%	-0.59%
4	2000	2.95E-04	-0.9287	0.0142	-0.1214	-0.37%	-1.46%	-0.64%
5	1000	5.90E-04	-0.9289	0.0142	-0.1214	-0.35%	-1.72%	-0.65%

3.4.6 Source term technique

Saito *et al.* validated a body-fixed, source term based, numerical model of a decelerating sphere against experimental results of a projectile decelerating in a ballistics range [14]. The same experimental results were then used to validate the numerical study done by Roohani *et al.* [44] on a decelerating sphere using the source term model described in section 3.3. Both models showed good correlation with the experimental results. The latter source term technique has also been validated against a numerical moving reference technique in a study on supersonic accelerating bodies [20] and experimental results from a ballistic range, where the flow field of a decelerating bluff body were studied at varying decelerations [21].

4 RESULTS

This chapter has been broken into two sections; the first focuses on the upright RAE 2822 aerofoil and the second on the inverted RAE 2822. These cases are then further broken down into the results that focus on ground effect, transient effects and then influence of angle of attack for an upright and inverted aerofoil. Both orientations have been investigated in order to obtain a comprehensive understanding of the impact of ground effect on the aerodynamics of an accelerating or decelerating aerofoil, as in the cases of: a wing in ground effect vehicle, low-flying aircraft, sea-skimming cruise missiles, high performance race cars or the BSSC, where programmable winglets vary their angle of attack in accordance with the stabilization of the wheel loading. Each case was subjected to a free-stream temperature of 300 K and an atmospheric pressure of 101 325 Pa. The pitching moment is calculated around the quarter chord of the aerofoil or moment reference center, which is assumed to be at 25 % of the chord length and along the chord line. The aerodynamic performance has been given in terms of the aerodynamic forces and pitching moments acting on the body. These values have not been given as non-dimensional coefficients as the numerator in the non-dimensional force varies with the velocity of the aerofoil as it accelerates and decelerates.

4.1 Upright RAE 2822 aerofoil

Here the RAE 2822 aerofoil was orientated in the upright position and at an angle of attack of 2.79° to produce positive lift.

4.1.1 Ground Effect

The following steady state ground clearance cases were considered: h/c = 1.00, 0.50, 0.25, 0.10, and 0.05, and then compared against free flight conditions. Throughout the subsonic region (up to Mach 0.70) there was only a slight gain in lift and aerodynamic efficiency due to ground effect, with the largest increase in lift occurring in the supersonic region. However, this was negated by a significant drop in aerodynamic efficiency with the increase in wave drag.

Figure 24 to Figure 30 show how the reduced ground clearance affects the aerodynamic performance of the aerofoil. In each case, the aerodynamic performance for each ground clearance has been plotted on the same set of axes in order to directly compare the results. In the transonic and supersonic regions, each change in performance is connected to a new shock formation or reflection on the aerofoil. Figure 26 shows the formation and propagation

of the shock waves on the aerofoil at a ground clearance of h/c = 0.50 as the free stream velocity is increased from rest up to Mach 2.80.

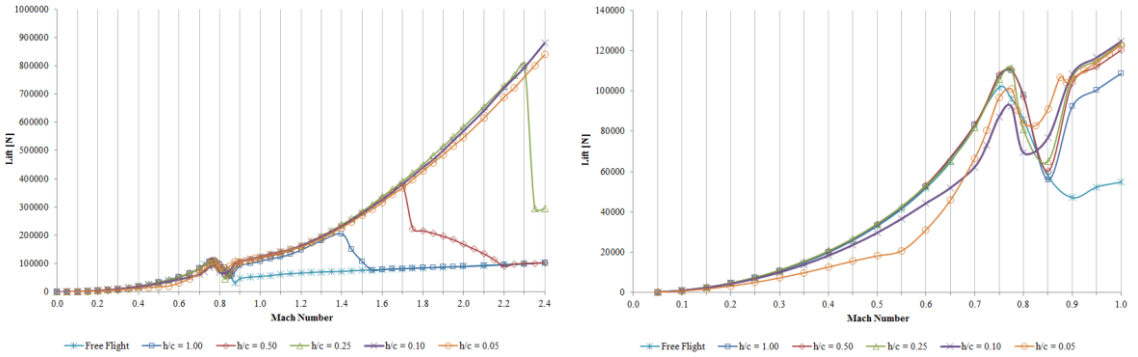


Figure 24: Overall (left) and subsonic and transonic (right) lift performance for the upright RAE 2822 aerofoil at different ground clearances.

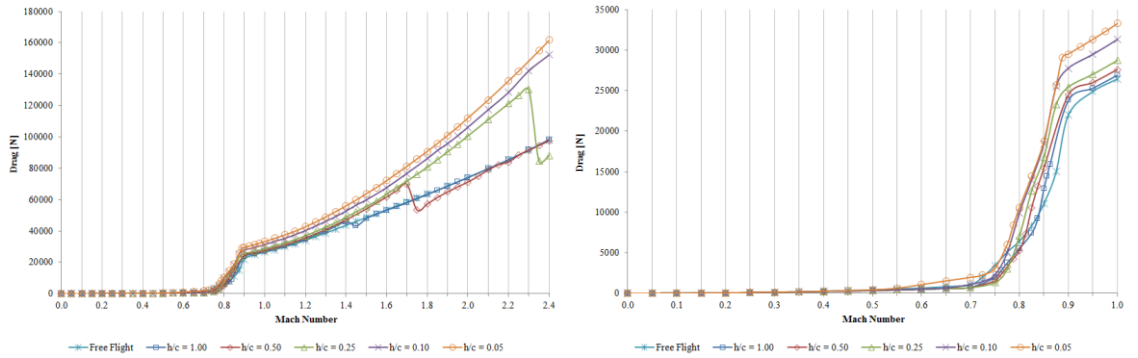
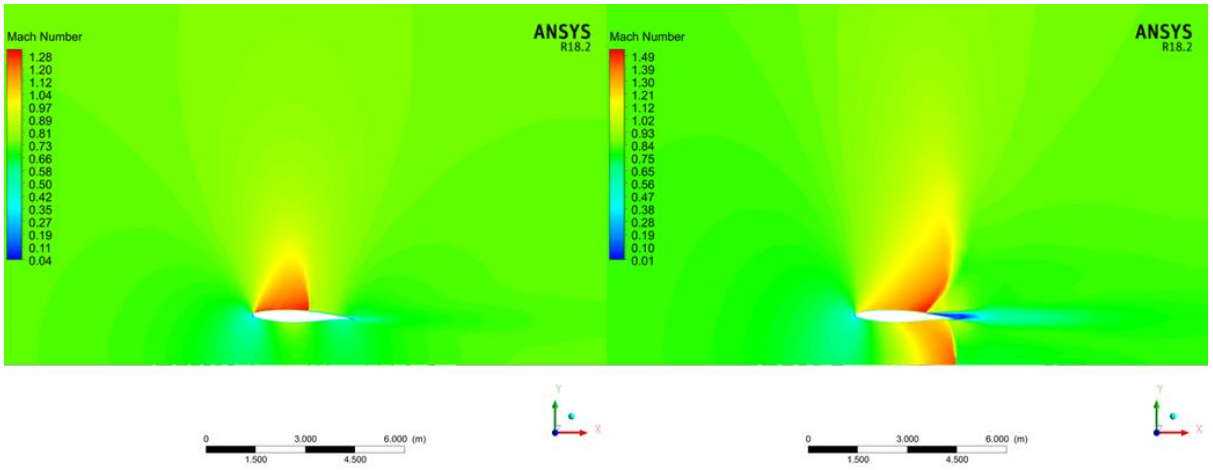


Figure 25: Overall (left) and subsonic and transonic (right) drag performance for the upright RAE 2822 aerofoil at different ground clearances.

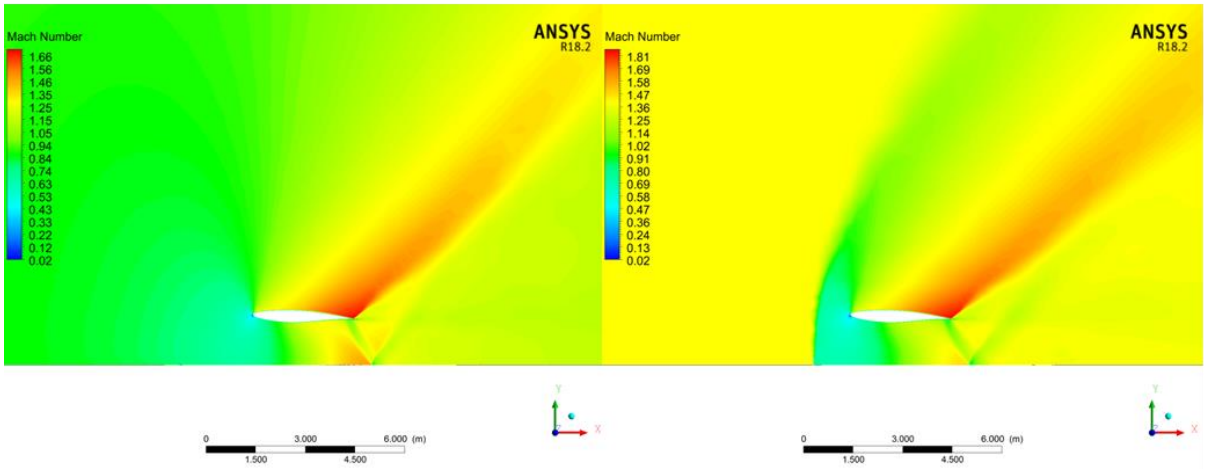
At Mach 0.65 the flow accelerating over the top of the aerofoil becomes supersonic and a normal shock forms on the upper surface. As the supersonic region of the shock wave grows in size over the top of the aerofoil, the pressure differential across the aerofoil decreases and there is rapid drop in lift. Due to the asymmetry introduced by the ground plane, the ground effect cases diverge from the free-stream case at this point. At approximately Mach 0.85 a normal shock forms on the lower surface of the aerofoil and as the supersonic region is smaller on the lower surface the lift starts to increase again.

From Mach 0.90 the shock locations stabilise, and the lift starts to increase exponentially as the velocity increases. Rapid drops in lift occur just after Mach 1.40, 1.70, and 2.30 respectively for each ground clearance. This is due to delayed reflection of the bow shock under the aerofoil and is discussed in more detail in the next chapter. The lift then drops more gradually as the reflected shock wave moves along the lower surface of the aerofoil, disrupting the pressure distribution as it goes. The h/c = 1.00 and h/c = 0.50 lift results then tend towards the lift performance results obtained at free flight conditions.



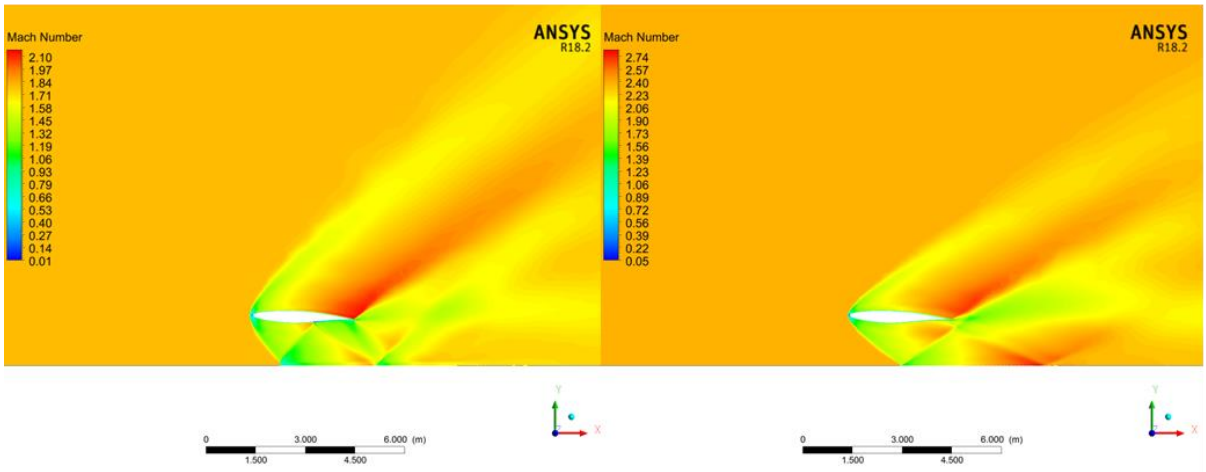
(a) Mach 0.75

(b) Mach 0.85



(c) Mach 1.00

(d) Mach 1.40



(e) Mach 1.80

(f) Mach 2.40

Figure 26: Mach flood plots of the development of flow field and shock formations for the upright aerofoil at different Mach numbers and constant ground clearance of h/c = 0.50.

The lowest ground clearance cases h/c = 0.10 and h/c = 0.05, the aerodynamic performance start diverging from the other cases as of Mach 0.40 and Mach 0.25 respectively. The lower clearance results in a steady drop in lift and promotes the formation of the normal shock underneath the aerofoil. As such the critical Mach number of the lower normal shock drops from Mach 0.75 to approximately 0.65 and 0.50 respectively.

With reference to Figure 25, the impact of ground effect on the drag performance is more straight forward with the ground effect cases only differing from the free-stream case after Mach 1.20. As discussed in the previous conference paper that focused on tri-sonic ground effect on the ground clearance cases: h/c = 1.00 and h/c = 0.50, the only changes in drag come from the induced drag component [2]. This is further confirmed by the convergence of these two ground clearances with free flight drag results. As with the lift case, the drag performance for the lower three ground clearances: h/c = 0.25, 0.10 and 0.05 is predicted to converge to the free flight conditions.

Figure 27 shows that increasing ground effect results in an average reduction in drag of 16 % of the subsonic results. Up to Mach 0.30 the drag reduction is 10%, but this steadily increases to 27 % at Mach 0.65 where the shock wave on the upper surface starts to form. The drag increases rapidly for the h/c = 0.10 and 0.05 cases as the wave drag increases with the earlier formation of the shock wave. At Mach 0.50, the drag of the h/c = 0.05 aerofoil increases as a normal shock forms between the ground and lower surface of the aerofoil. The strength of this shock wave intensifies, and the wave drag steadily increases until approximately Mach 0.725 when the shock on the upper surface develops. From this point the drag performance increases rapidly with the wave drag as with the other ground clearances and temporarily plateaus with the highest drag value at Mach 0.80, Figure 25. This case features the highest drag throughout the supersonic range.

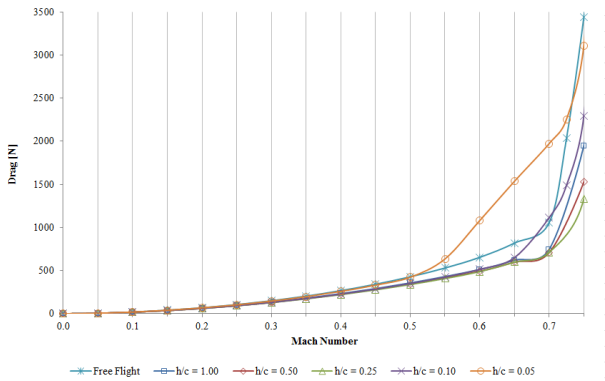


Figure 27: Subsonic drag performance for the upright RAE 2822 aerofoil at different ground clearances.

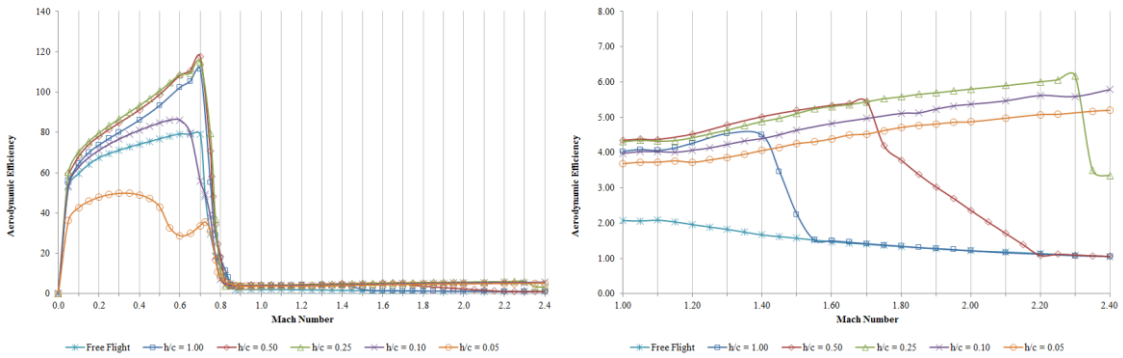


Figure 28: Overall (left) and supersonic (right) aerodynamic efficiency for the upright RAE 2822 aerofoil at different ground clearances.

The benefit of ground effect can clearly be seen in the subsonic region of Figure 28, with the aerodynamic efficiency increasing by an average of 45 % at Mach 0.70 when compared to free flight. In the supersonic region there is also a noticeable increase in aerodynamic efficiency, reaching a maximum increase of 170 % at Mach 1.40, 288% at Mach 1.70 and 464 % at Mach 2.30 for each respective ground clearance. However, the drag penalty for this increase in lift is severe, making it a less viable option. For h/c = 0.10 there is only a minor gain in aerodynamic efficiency. At h/c = 0.05 there is no benefit of ground effect, with the aerodynamic efficiency dropping to almost half the aerodynamic efficiency at free flight conditions.

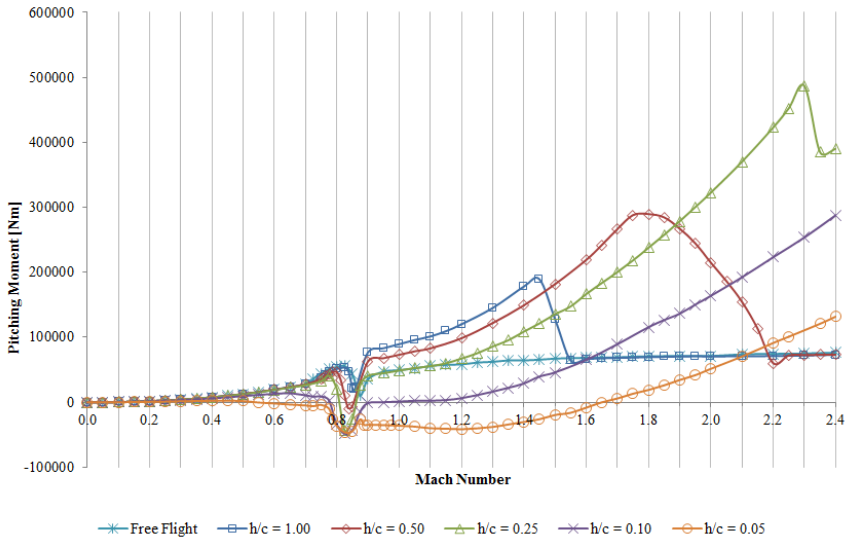


Figure 29: Pitching moment performance for the upright RAE 2822 aerofoil at different ground clearances.

In contrast to the lift and drag performance, Figure 29, illustrates a steady drop in the supersonic pitching moment with each reduction in ground clearance. The pitching moment also decreases significantly at Mach 0.85 as the upper and lower shocks form on the aerofoil. This loss increases as the ground clearance is reduced, with the moment in the lower cases

h/c = 0.50 to h/c = 0.10 temporarily reversing direction. The lowest clearance of h/c = 0.05 recovered the least from this drop and only becomes positive again at approximately Mach 1.65. This is shown in more detail in Figure 30. In the supersonic region the pitching moment initially increases and then drops off respectively at Mach 1.45, 1.75 and 2.30 as the ground clearance is reduced from free flight conditions. The supersonic pitching moment produced at the two lowest clearances is significantly lower than at the higher clearances and does not drop off within the range of Mach numbers considered for this study.

After the formation of the shock waves the lift and drag results for each ground clearance recovered to be within similar values, however, the pitching moment performance recovered to different values. With the lowest clearance only being 1.20 % less than the pitching moment at free flight conditions from Mach 1.00 to 1.10, as compared to an average increase of 49 % and 82 % for the two higher ground clearances. The lower recovery of the pitching moment continues into the supersonic region and the h/c = 0.25 results only surpass the higher ground clearances when the bow shock moves and reflects underneath each aerofoil, Mach 1.90, and Mach 1.50 respectively.

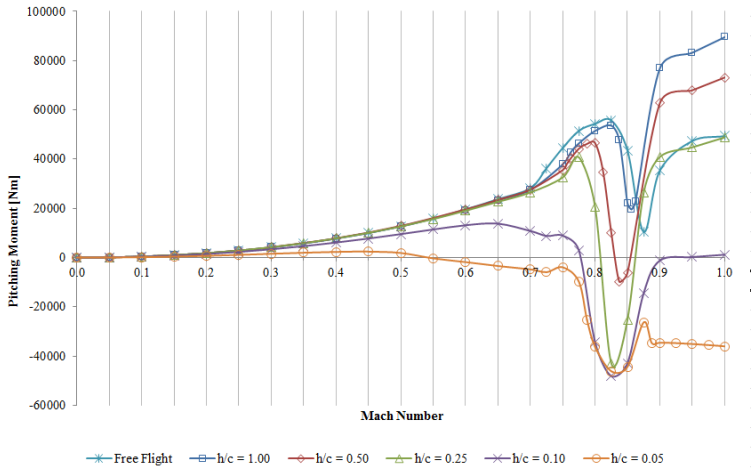


Figure 30: Subsonic and transonic pitching moment performance for the upright RAE 2822 aerofoil at different ground clearances.

As expected, the pitching moment reflects the rapid changes in lift as the bow shock passes under the aerofoil. However, as discussed later, the movement of the reflected shock wave **R** (as defined in Figure 14**)** on the lower surface of aerofoil at h/c = 0.50 reduces the severity of the drop in pitching moment. Figure 31 shows the progression of the shock as it strikes the aerofoil and then propagates past the trailing edge.

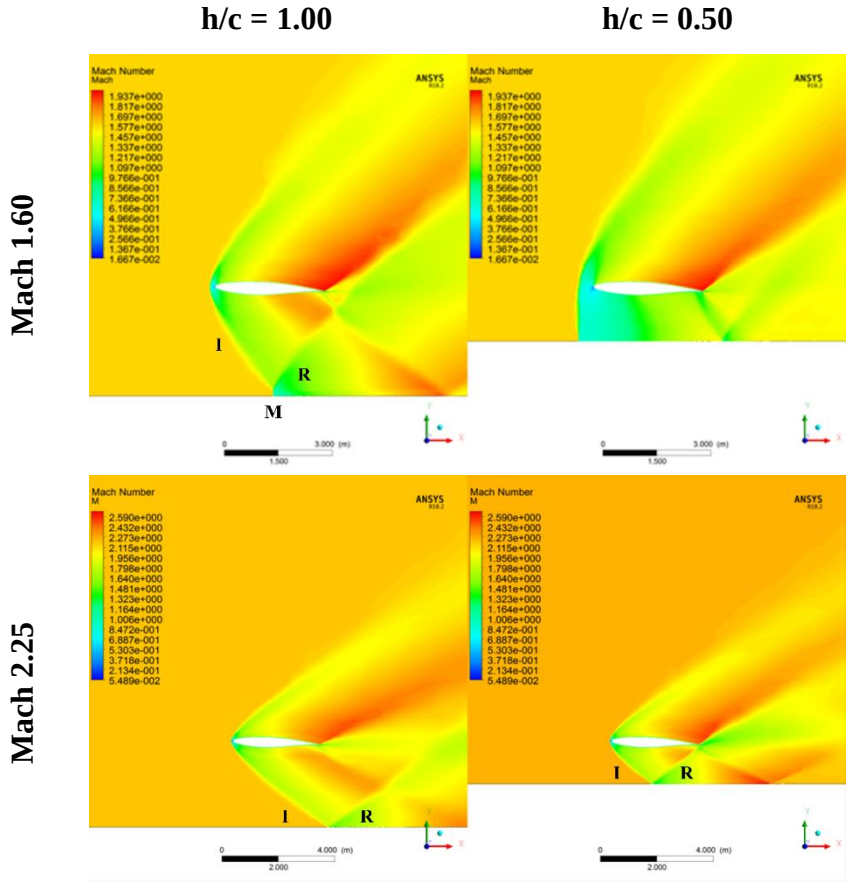


Figure 31: Mach number plot comparison of the propagation of the reflected bow shock under the upright RAE 2822 aerofoil at two different ground clearances.

4.1.2 Transient Effects

The transient acceleration results of the upright RAE 2822 aerofoil accelerating at a ground clearance of h/c = 1.00 are detailed here. The transient simulations were initiated using the steady state results at Mach 0.20 and the extreme acceleration case of 176 g was used to further highlight the transient effects on the aerodynamic performance. As discussed in section 3.2, the aerodynamic performance of the steady state and transient results are compared to identify the differences in two cases. In Figure 32 and Figure 33, the performance peaks and subsequent decreases in performance identified in the previous section occur at higher Mach numbers in the transient case. For example, the peak lift performance in the transonic and supersonic regimes occurred respectively at Mach 0.90 and 1.55 for the transient results, instead of Mach 0.75 and 1.35 as in the steady state results. In a previous publication by the current author [2], this shift in the lift and drag performance is shown to be caused by the differences in the shock location and strength of the shock waves on and ahead of the aerofoil and is discussed in detail in the next chapter.

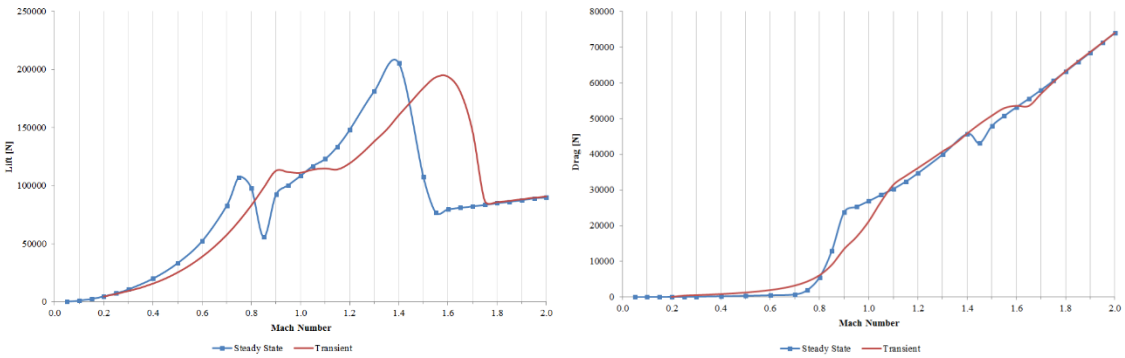


Figure 32: Upright RAE 2822 aerofoil, h/c = 1.0 - steady state and transient 176 g lift (left) and drag (right) performance curves

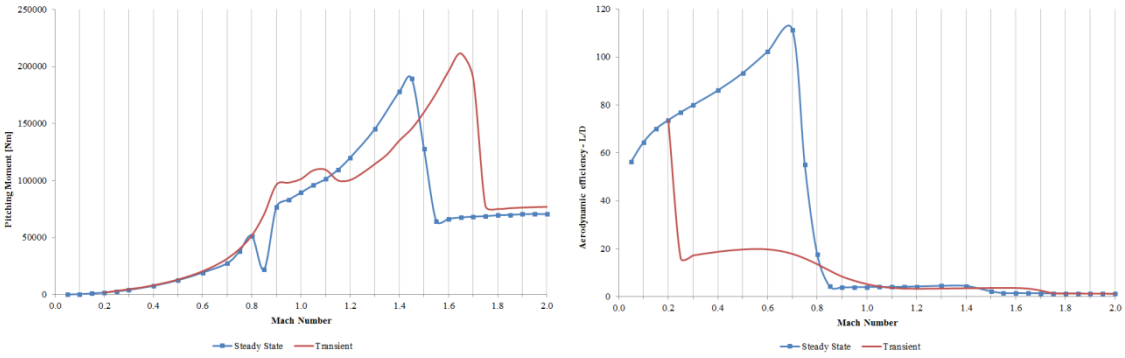


Figure 33: Upright RAE 2822 aerofoil, h/c = 1.0 - steady state and transient 176 g pitching moment (left) and aerodynamic efficiency (right) performance curves

Figure 33 shows that in the subsonic region, the transient pitching moment follows the steady state results quite closely, with the first deviation coming in at about Mach 0.60. At this point, the flow starts becoming supersonic on the upper surface of the steady state aerofoil and the supersonic bubble starts to grow over the leading edge of the aerofoil as per Figure 34 (a). This region of supersonic flow continues to grow along the upper surface of the aerofoil and the pressure differential across the aerofoil increases. Consequently, the pitching moment increases again up until Mach 0.80 where the lower shock starts to form on the lower surface of the aerofoil. From the pressure distribution on the aerofoil at Mach 0.85, Figure 34 (b), it can be seen that the supersonic regions of flow on either side of the aerofoil reduce the positive pitching moment. With the shock waves still developing in the transient case, the pitching moment continues to rise, as per the lift performance, without this drastic drop. Consequently, the transient pitching moment is higher than that of the steady state case from Mach 0.80 to approximately Mach 1.125, where the shock locations and pressure distributions of the two cases almost overlap.

Between Mach 1.00 and Mach 1.15 there is an additional increase in pitching moment. As the bow shock starts to form the higher pressures from the subsonic region under the nose of the

aerofoil further increase the pitching moment. From this point until Mach 1.60 the pitching moment continues to increase with the lift performance. Between Mach 1.60 and 1.65, the lift starts to drop while the pitching moment continues to increase, momentarily surpassing the steady state pitching moment. By Mach 1.65 the bow shock reflects under the aerofoil and the pitching moment drops significantly. Unlike the aerodynamic forces the pitching moment does not converge with the steady state results once the trailing shock has moved passed the trailing edge.

Figure 35 highlights the reduction of the propagation of the transient shockwaves into the surrounding flow field. The bow shock on the accelerating aerofoil forms with a smaller stand-off than that seen on the steady state case. Previous research discussed in section 2.1, has shown that the bow shock stand-off distance for an accelerating object is larger than that formed at steady state [12].

(a)

(b)

(c)

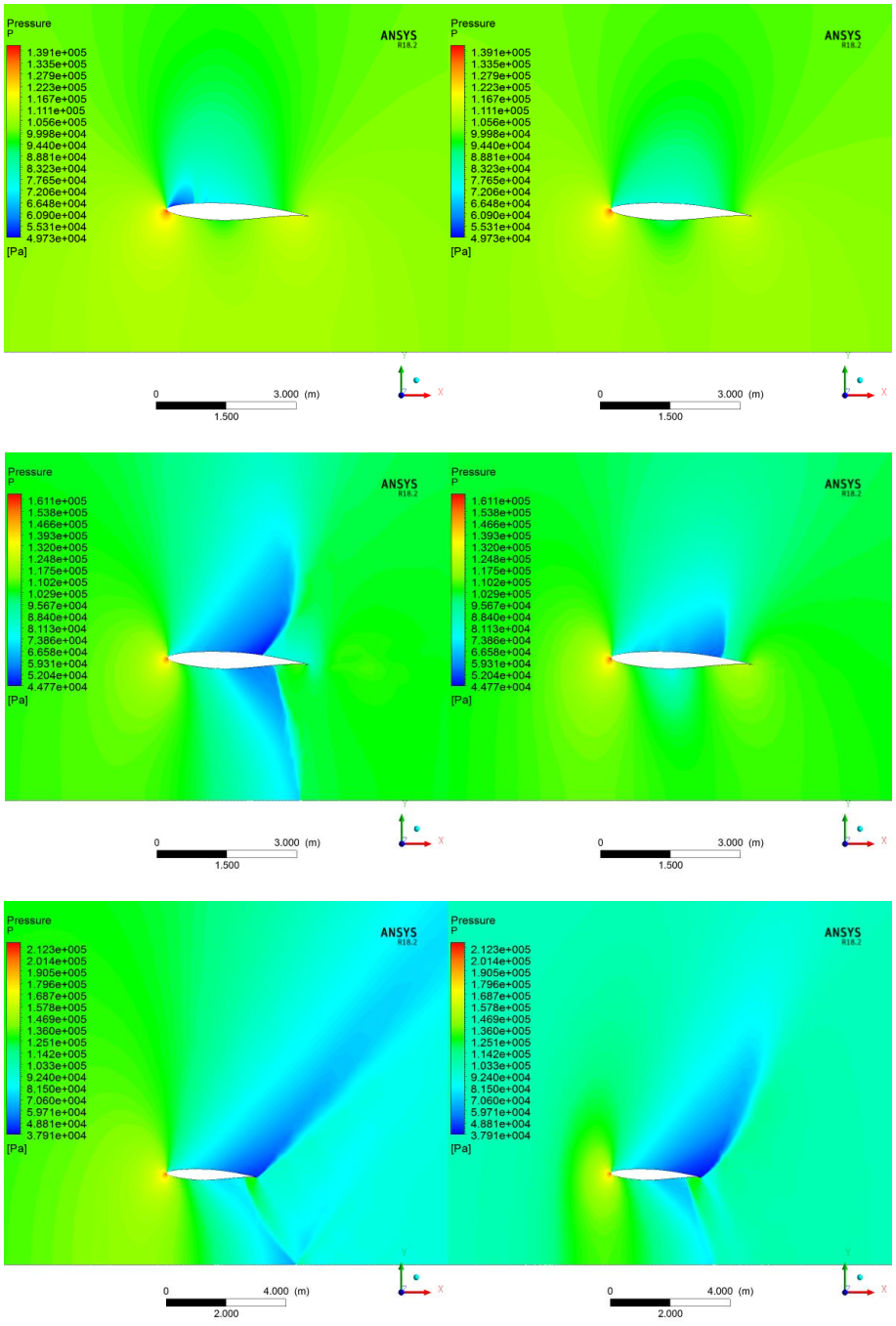


Figure 34: Upright RAE 2822 aerofoil, h/c = 1.00 – difference in steady state (left) and transient 176 g (right) results at (a) Mach 0.70, (b) Mach 0.85 and (c) Mach 1.10.

At Mach 1.30, the stand-off distances are more comparable; however, the steady state shock has a greater curvature. The inverse is true for the lower normal shock wave, which also forms on the aerofoil later and reflects off the ground with a lower incident angle, reflected angle and an additional trailing shock, as shown by the density plots in Figure 36. The upper normal shock is stronger and has a lower Mach angle, as the velocity of the flow approaching the trailing edge of the aerofoil is higher.

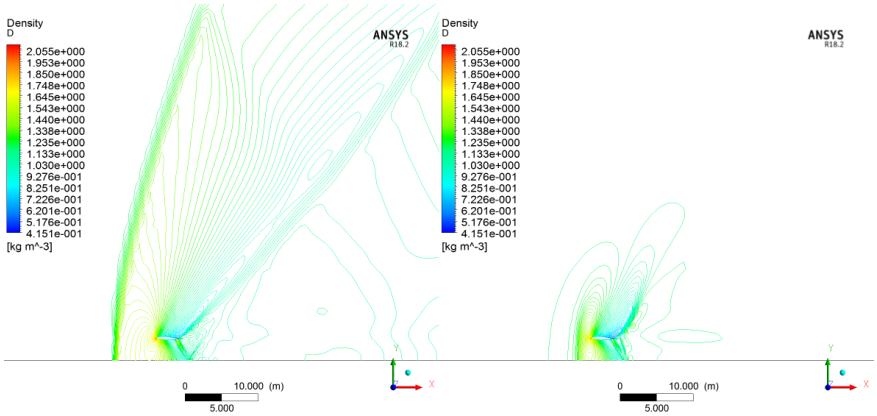
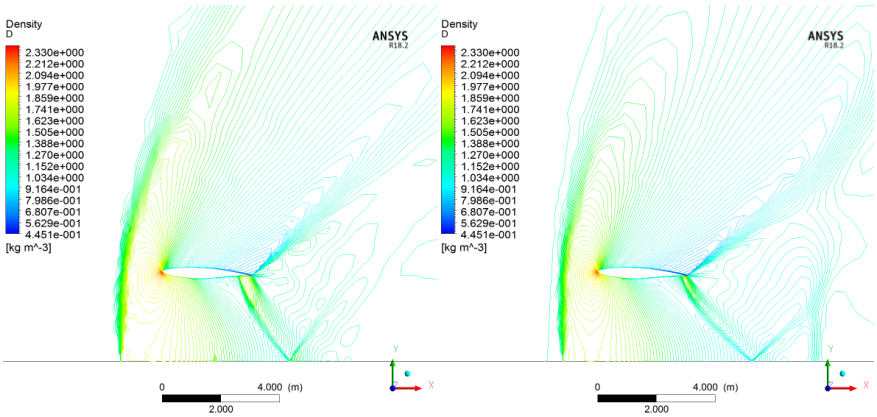


Figure 35: Upright RAE 2822 aerofoil, h/c = 1.00 - comparison of steady state (left) and transient 176 g acceleration (right) shock wave development and propagation.

(a)



(b)

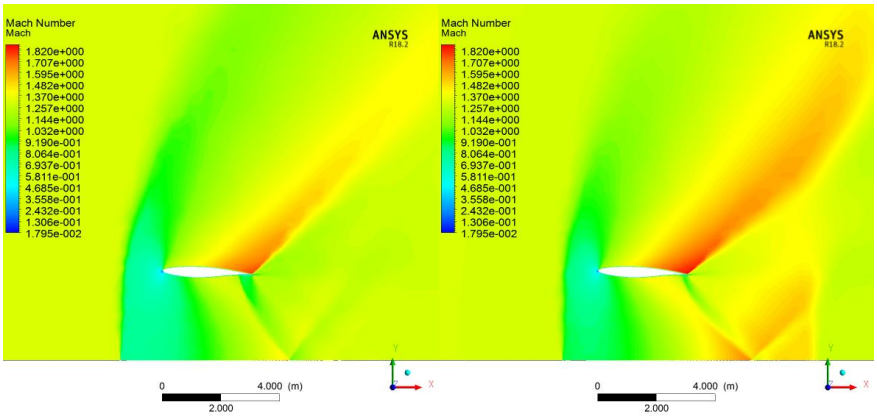


Figure 36: Upright RAE 2822 aerofoil, h/c = 1.00 – (a) density contours and (b) Mach flood plots for the steady state (left) and transient 176 g (right) shock structures at Mach 1.30

From Mach 1.30 onwards the stand-off distance of the accelerating bow shock is less than the steady state case. This is as expected with reference to the current literature [12]. Therefore, the extreme acceleration has introduced additional inertial effects causing the bow shock wave to form later and closer to the leading edge of the aerofoil.

4.1.3 Angle of Attack

Two additional angles of attack steady state cases were considered, $\alpha = 0.0°$ and $\alpha = 6.0°$, in order to evaluate the effects of angle of attack on the overall aerodynamics and shock locations for a specific ground clearance. The ground clearance was kept constant at $h/c = 0.50$ to increase the effects of ground effect without shock waves forming prematurely between the aerofoil and the ground, especially at the largest angle of attack. The chosen angles of attack were based on the range of the programmable winglets of the BSSC [4].

The lift and pitching moment performance is given in Figure 37 and the drag and aerodynamic efficiency performance in Figure 38. As to be expected the overall lift, pitching moment and drag increased with angle of attack. The increasing angle of attack also accelerated the flow over the top of the aerofoil and reduced the critical Mach number for the upper shock. Consequently, the upper shock forms further forward on the aerofoil, a larger supersonic bubble forms above the aerofoil and a stronger shock also develops with a greater region of separated flow. However, as per the shock structures shown in Figure 39 at Mach 0.85, the reduced flow under the aerofoil delays the formation of the lower trailing edge shock – approximately a normal shock at this point, which is almost absent from the $\alpha = 6.0°$ case, as seen in Figure 39 (c). As seen with the pitching moment performance in Figure 37, the later development of the lower means that there is no sudden drop in pitching moment at Mach 0.85. In this case though, the lower shock develops at the trailing edge of the aerofoil and thus does not disrupt the pressure distribution as seen at the lower angles of attack.

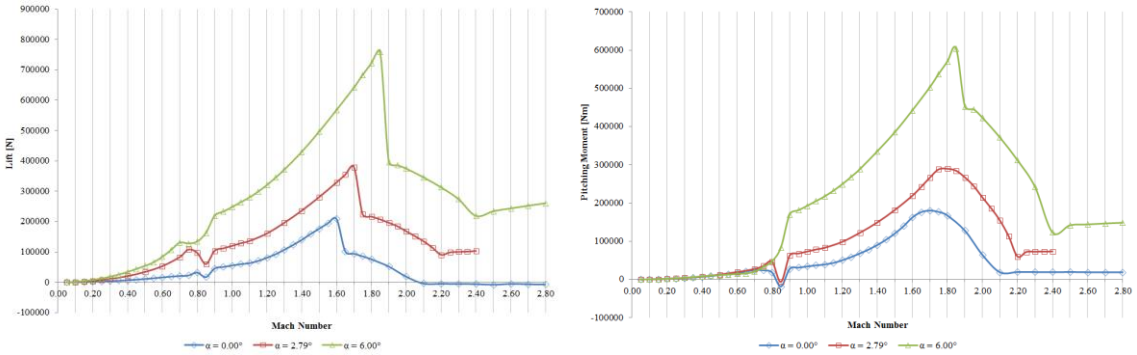


Figure 37: Upright RAE 2822 aerofoil, h/c = 0.50 – lift (left) and pitching moment (right) performance curves at different angles of attack.

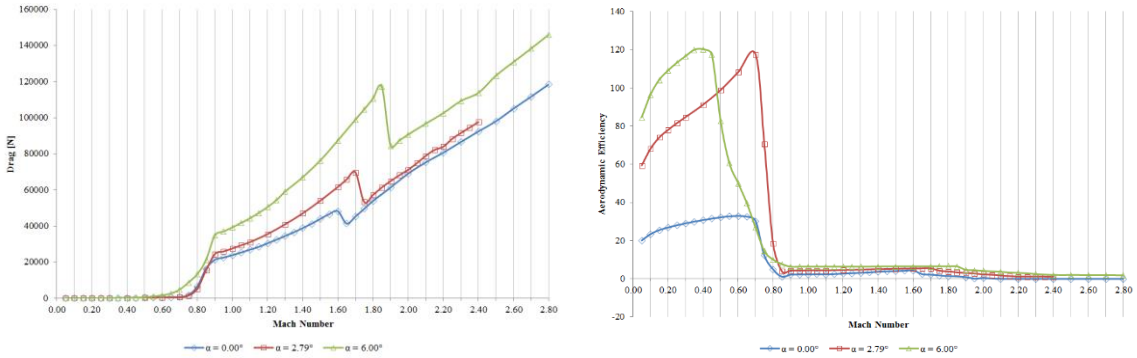
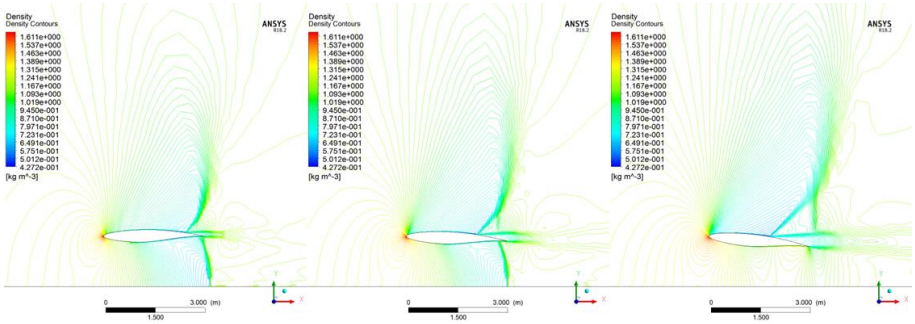


Figure 38: Upright RAE 2822 aerofoil, h/c = 0.50 – drag (left) and aerodynamic efficiency (right) performance curves at different angles of attack.

In the subsonic region, there is a large gain aerodynamic efficiency when the angle of attack is increased. This gain is limited by the formation of the lower normal shock and since this shock forms earlier at the higher angle of attack, the increased angle of attack is no longer beneficial from approximately Mach 0.50 and onwards.



(a) α = 0.00° **(b) α = 2.79°** **(c) α = 6.00°**

Figure 39: Density contour plots for angle of attack analysis of the RAE 2822 aerofoil at Mach 0.85

In the supersonic region, the reflection of the bow shock under the aerofoil occurs earlier for the lower angle of attack and later for the higher angle of attack, as seen in Figure 40. The stand-off distance is also seen to increase with the angle of attack. When this shock does reflect, the higher angle of attack leads to a much stronger reflection forming under the aerofoil, as indicated by the rapid drop in pitching moment performance. Once the reflection passes the aerodynamic center of the aerofoil the pitching moment decreases as per the other two lower angles of attack, as discussed in section 4.1.1.

Figure 40 shows that the bow shock stand-off distance also increases with increasing angle of attack.

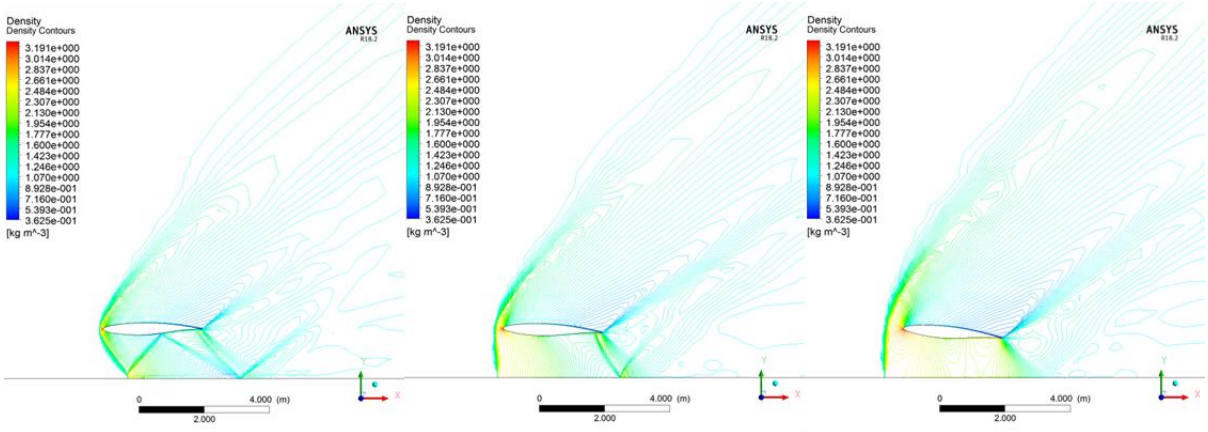


Figure 40: Density contour plots for angle of attack analysis of the RAE 2822 aerofoil at Mach 1.70. Angle of attack increases from left to right, $\alpha = 0.00°$ (left), $\alpha = 2.79°$ (middle), and $\alpha = 6.00°$ (right).

4.2 Inverted RAE 2822 aerofoil

In this case the aerofoil has an inverted orientation and has a negative (nose down) angle of attack of -2.79° to produce negative lift or downforce.

4.2.1 Ground Effect

As with the upright aerofoil the following ground clearance cases were covered h/c = 1.00, h/c = 0.50 and h/c = 0.25 and compared against free flight. An additional two ground clearances were studied h/c = 0.10 and h/c = 0.05. Figure 49 - Figure 50 show the key points in the shock wave formation and propagation on the inverted aerofoil. The aerodynamic performance of the inverted aerofoil is given in Figure 41 - Figure 43. The ground effect cases were split into two sets with the free flight and higher ground clearances h/c = 1.00 and h/c = 0.50 in one and the lower ground clearances h/c = 0.25, 0.10 and 0.05 in the other. Density contour plots at key points in the development of the flow field for each set of ground clearance have been given respectively in Figure 49 and Figure 50.

On the right of Figure 41 the downforce is shown to increase with the reduced ground clearance. This increase in downforce reaches a maximum and then steadily declines after the normal shock forms on the lower surface of the aerofoil. The rate of this decline decreases with the reduction in ground clearance. After Mach 0.70 the decline in downforce becomes more severe and for the lower ground clearances the normal force component reverses and the aerofoil starts producing lift. The decline in downforce reaches a minimum and then temporarily increases before plateauing, between Mach 0.90 and 1.20, and declining again as

the free stream flow becomes supersonic. After Mach 0.90 the ground effect results diverge from the free flight results. However, the higher ground clearance cases, h/c = 1.00, h/c = 0.50 tend towards and then overlap the free flight results. The same trend is initially seen with the h/c = 0.25 normal force results, but the convergence is predicted to occur at much higher free stream velocities. For the lowest two ground clearances the normal force, now acting as lift, continues to increase with Mach numbers as high as Mach 3.00.

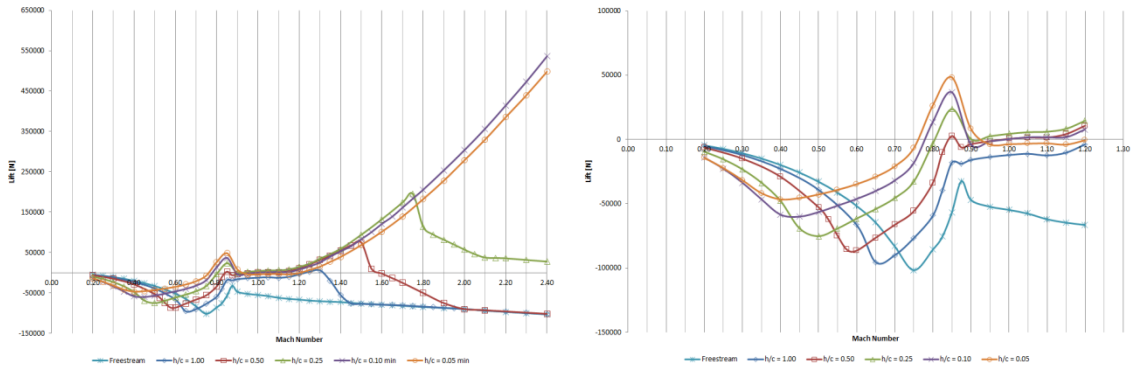


Figure 41: Inverted RAE 2822 aerofoil - ground effect lift performance overall (left) and subsonic to transonic (right) comparison.

Key free stream Mach numbers; such as the critical Mach numbers for the lower, $M_{cr\text{-}l}$ and upper surfaces of the aerofoil $M_{cr\text{-}u}$, Mach numbers for each inversion of the normal force and the reflection of the bow shock under the aerofoil M_R are defined here and summarized in Table 4 for further discussion in the next chapter.

The drag performance results for the different ground clearances are shown in Figure 42, with a closer view of the subsonic and transonic drag results given on the right of this image. The drag is seen to rise at progressively lower Mach numbers with each decrease in ground clearance. Between Mach 0.75 and 0.90 the drag divergence occurs almost simultaneously across all the cases, with the ground effect cases rising consistently ahead of the free flight case. After the drag divergence, a consistent increase in drag is seen with each reduction in ground clearance. For the two lowest ground clearance cases this trend continues for the rest of the speed range. As with the upright aerofoil the rest of the drag results fluctuate with the induced drag component and eventually tend toward the free flight results.

Table 4: Summary of shock wave formation, shock wave propagation and lift inversions for an inverted RAE 2822 at different steady state ground clearances.

Ground Clearance, h/c	Critical Mach Number Lower, M_{cr-l}	Critical Mach Number Upper, M_{cr-u}	Mach number for each lift inversion	Bow shock passing under aerofoil, M_R
Free flight	0.70	0.83	N/A	1.00
1.00	0.60	0.80	1.225, 1.325	1.30
0.50	0.55	0.78	0.85, 1.00, 1.58	1.50
0.25	0.45	0.75	0.80, 0.90, 0.92	1.75
0.10	0.40	0.74	0.78, 0.90, 1.00	> 2.80
0.05	0.40	0.73	0.76, 0.92, 1.20	> 2.80

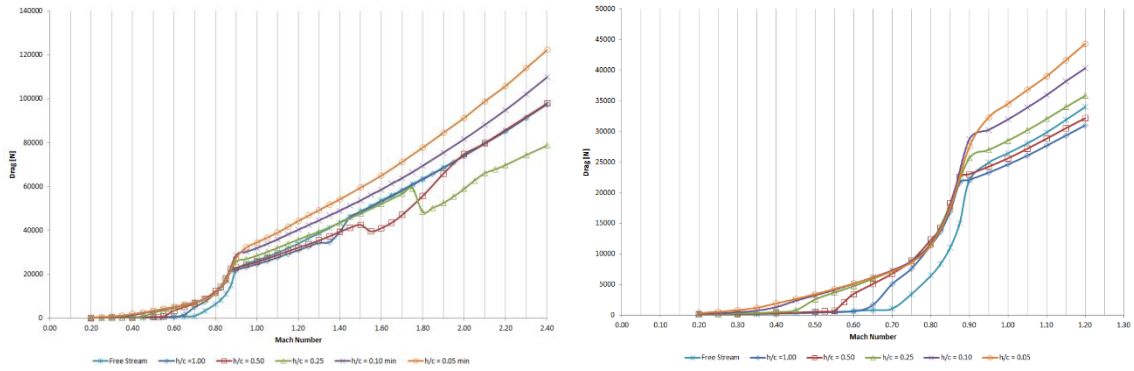


Figure 42: Inverted RAE 2822 aerofoil - ground effect drag performance overall (left) and subsonic to transonic (right) comparison.

The pitching moment performance is shown in Figure 43 and is negative, acting to rotate the aerofoil nose down. Unlike the upright aerofoil, the subsonic pitching moment increases with reducing ground clearance. However, there appears to be a limit to this increase with the pitching moment at the two lowest ground clearances converging between Mach 0.20 and Mach 0.40. The next highest ground clearance also follows a similar trend. The pitching moment increases as each formation of the lower shock occurs at a different location on the aerofoil. Between Mach 0.75 and 0.90 the upper shock forms and the supersonic regions above and below the aerofoil greatly reduce the pressure distribution across the aerofoil and the pitching moment drops drastically.

As with the drag two different trends appear for the higher and lower sets of ground clearances. The higher clearances have a decreased pitching moment than at free flight, while the lower clearances have an increased pitching moment. Overall, as the ground clearance is reduced the pitching moment increases. However, for each ground clearance, the pitching moment increases to a point before it starts decreasing and in the cases below h/c = 1.00 changing direction. This decrease comes in as the pressure build underneath the nose of the

aerofoil and once this pressure build up is disrupted the higher ground clearances, h/c = 1.00 and h/c = 0.50, tend to back to the free flight case, at Mach 1.50 and Mach 2.00, and ground effect no longer effects the pitching moment. For the lower ground clearances, the pitching moment remains negative up to higher supersonic Mach numbers: 1.65, 2.10 and above Mach 3.00 respectively as the ground clearance decreases. For the h/c = 0.25 there is a large increase in pitching moment due to reflected shock striking the aerofoil ahead of the aerodynamic center and drastically changing the pressure distribution in favour of a nose up pitching moment.

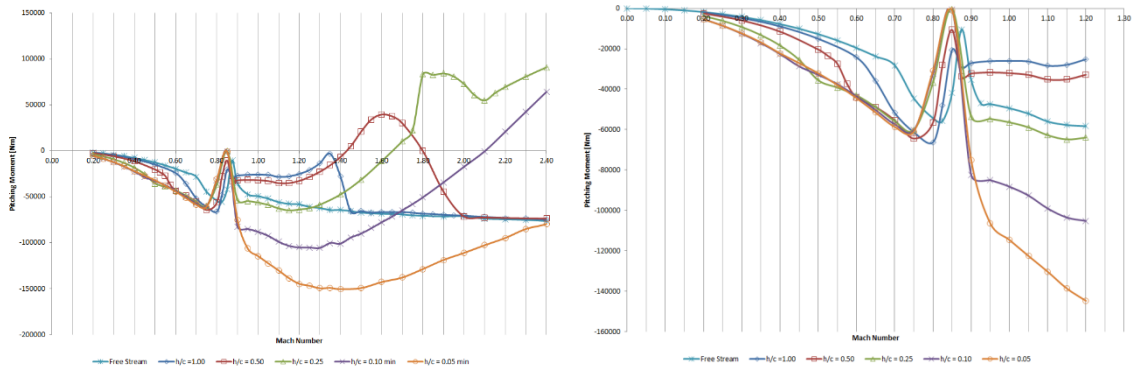


Figure 43: Inverted RAE 2822 aerofoil - ground effect pitching moment performance comparison overview (left) and subsonic to transonic results (right)

Ground effect has a greater impact on the aerodynamic efficiency of the inverted aerofoil, see Figure 44, and not only does the earlier shock wave increase the drag, but it also decreases the downforce produced by the aerofoil. As such, there is no gain in aerodynamic efficiency for the lowest ground clearance – in fact there is a 36 % loss in aerodynamic efficiency. The greatest gain in subsonic aerodynamic efficiency was 37 % and occurs at Mach 0.55 and h/c = 0.50.

The pressure distribution and shock locations on the upper and lower surface of the aerofoil are given in Figure 45 and Table 5. For the higher ground clearances, the shock waves form further downstream with decreasing ground clearance, while for the lower ground clearances the shock waves form further forward.

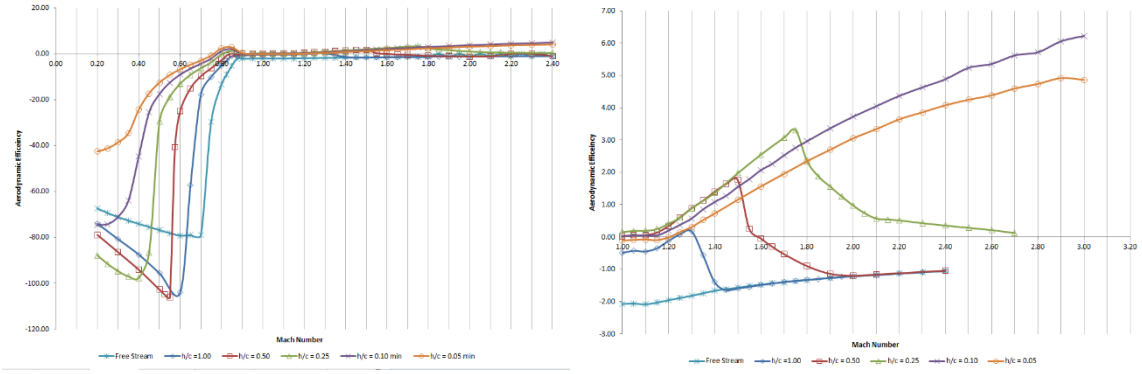
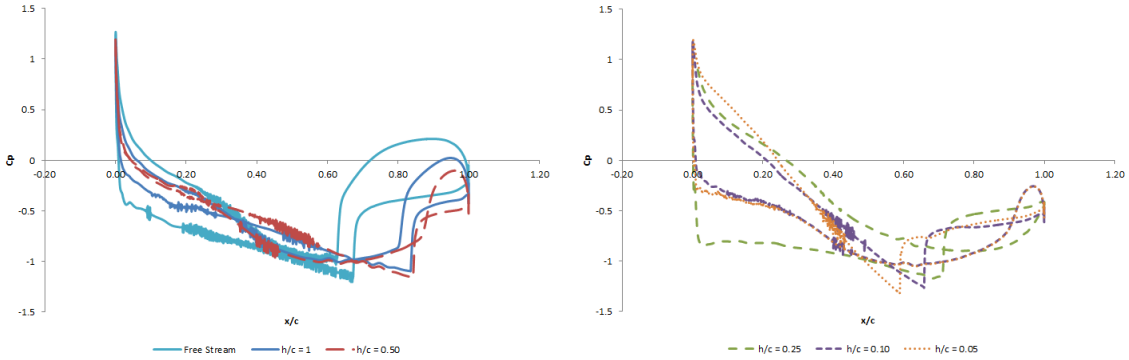


Figure 44: Inverted RAE 2822 aerofoil – ground effect aerodynamic efficiency comparison overview (left) and supersonic results (right)

Table 5: Shock locations on inverted RAE 2822 aerofoil at Mach 0.85 and different ground clearances.

	Ground Clearance					
Surface	**Free**	**h/c = 1.00**	**h/c = 0.50**	**h/c = 0.25**	**h/c = 0.10**	**h/c = 0.05**
Upper	0.660	0.840	0.843	0.694	0.646	0.574
Lower	0.615	0.804	0.855	0.934	0.904	0.904



(a) **(b)**

Figure 45: Pressure distributions at Mach 0.85 for two sets of ground clearances (a) free flight, h/c = 1.00 and h/c = 0.50 and (b) h/c = 0.25, 0.10 and 0.05.

In the supersonic region and for the h/c = 1.00 and h/c = 0.50 cases, the pitching moment drops when the bow shock passes under the aerofoil and then after Mach 2.20 the results match up with the free stream case. Figure 47 shows that as the reflected shock leaves the trailing edge of the aerofoil, the pressure distributions of the h/c = 1.00 and h/c = 0.50 cases match up with the free stream.

The increase in pitching moment between Mach 1.75 and 2.10 is caused by the initial build up in pressure before the bow shock reflects underneath the aerofoil. Once the bow shock

propagates under the aerofoil it reflects twice, striking the aerofoil at x/c = 0.296 and x/c = 0.837. Above Mach 2.10, the second reflection passes the trailing edge of the aerofoil and the pitching moment continues to increase.

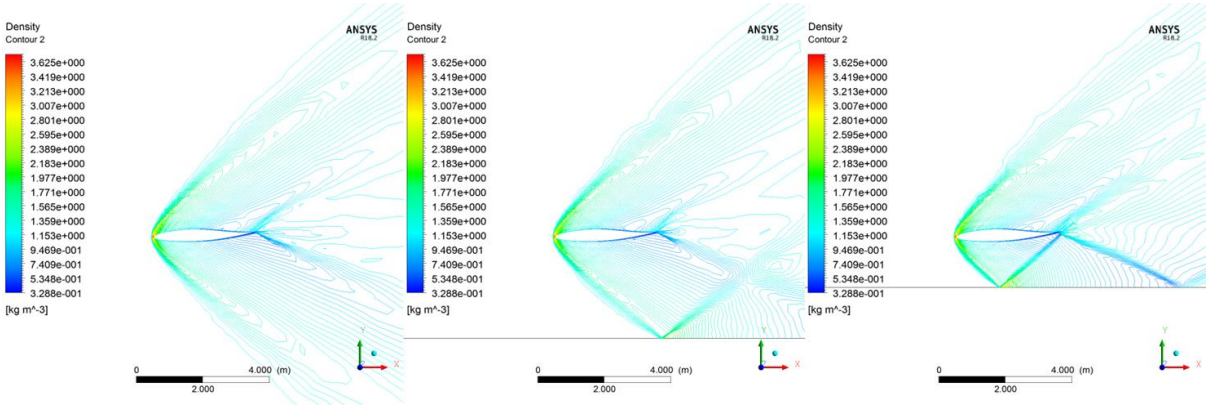
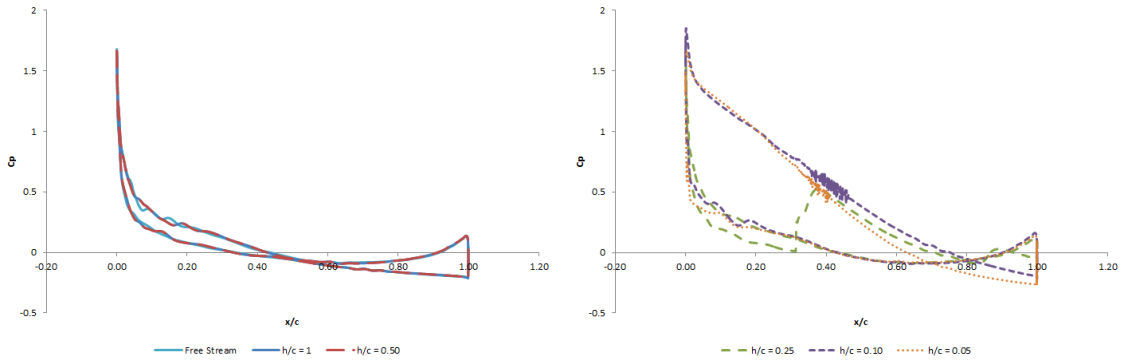


Figure 46: Density contour plots for an inverted RAE 2822 aerofoil traveling Mach 2.00 at free stream (left), h/c = 1.00 (middle) and h/c = 0.50 (right).



(a) **(b)**

Figure 47: Inverted RAE 2822 pressure distributions at Mach 2.00 for two sets of ground clearances (a) free stream, h/c = 1.00 and h/c = 0.50 and (b) h/c = 0.25, 0.10 and 0.05.

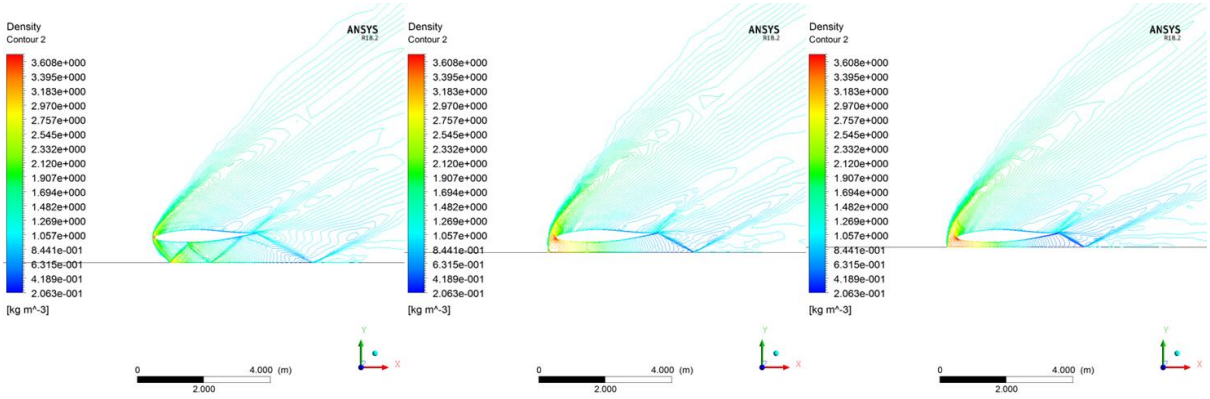


Figure 48: Density contour plots for an inverted RAE 2822 aerofoil traveling Mach 2.00 at h/c = 0.25 (left), h/c = 0.10 (middle) and h/c = 0.05 (right).

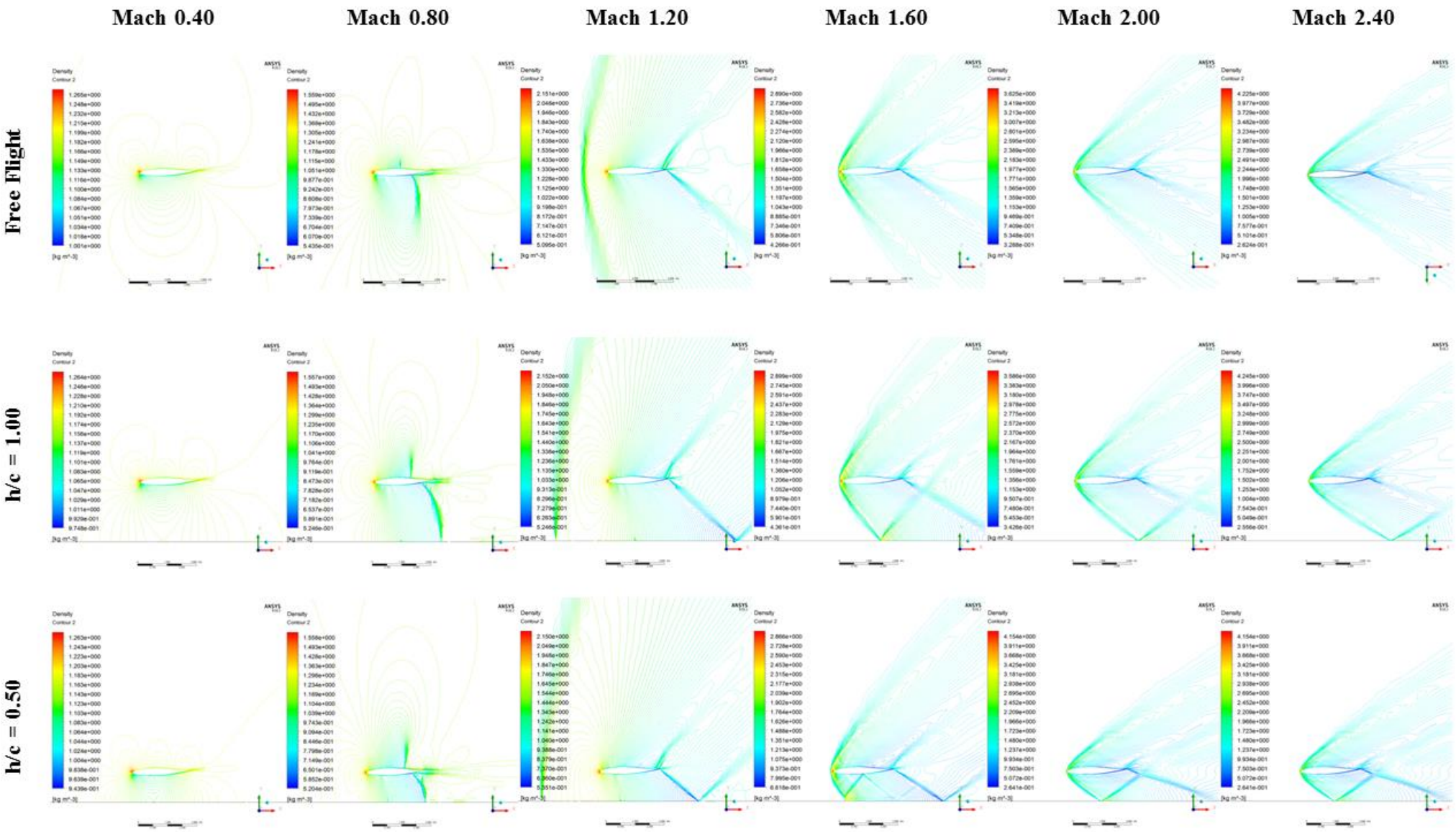


Figure 49: Density plots of the RAE 2822 shock wave development from Mach 0.40 (left) to Mach 2.40 (right) at free flight, h/c = 1.00 and h/c = 0.50.

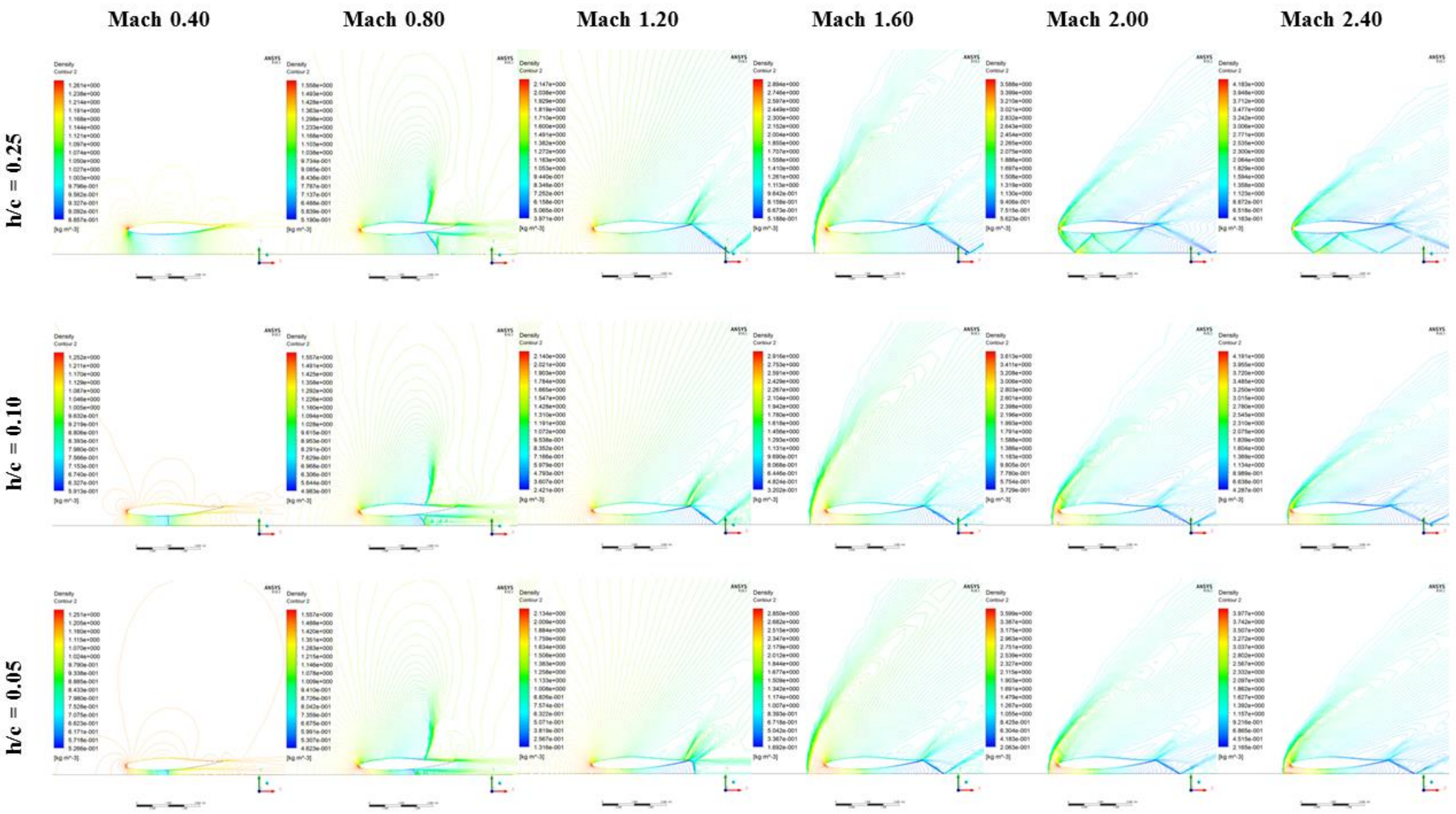


Figure 50: Density plots of the RAE 2822 shock wave development from Mach 0.40 (left) to Mach 2.40 (right) at h/c = 0.25, h/c = 0.10 and h/c = 0.05.

4.2.2 Transient Effects

Three different acceleration cases were considered: 176 g, 40 g, and 3 g, with the latter two cases being chosen based on the accelerations of the TSSC vehicle and the TSSC model used in the Pendine tests. The former is based on typical acceleration rates for ballistic missiles. The RAE 2822 aerofoil was kept at a constant angle of attack of -2.79° and ground clearance of h/c = 1.00. In each case, the aerofoil is decelerated back down to initial conditions to evaluate the transient effects of the deceleration of an accelerated particle, as illustrated in Figure 7. Key features from these results have been presented below:

176 g Results

Figure 51 shows the downforce performance of the aerofoil at constant steady state velocities, under 176 g acceleration from an initial speed of Mach 0.20 up to Mach 2.00 and then decelerating back down to Mach 0.20. The shift in the transient acceleration results identified in section 4.1.2 is seen here in the deceleration results as well. These results confirm those obtained in the unsteady free flight investigation mentioned in 2.1. For subsonic Mach numbers up to Mach 0.65, acceleration leads to a decrease in downforce and from Figure 56 an increase in drag. With the delay in the shock formations on the accelerating aerofoil, explained later in terms of Figure 60 (left) and by the associated drop in downforce, the transonic downforce for the accelerating aerofoil is greater than that at the equivalent instantaneous steady state velocity.

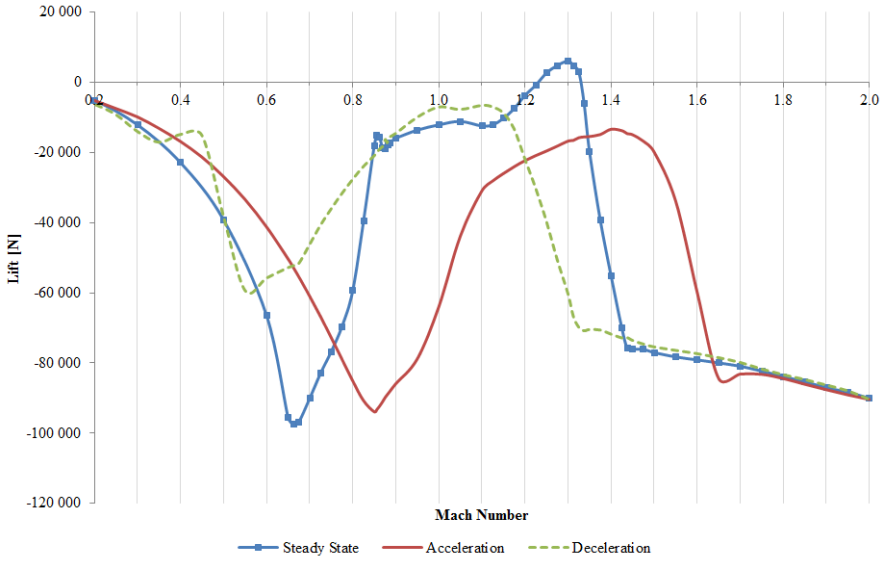


Figure 51: Downforce performance of the inverted RAE 2822 aerofoil, α = -2.79° and h/c = 1.00 - steady state, ± 176g acceleration

In both the acceleration and deceleration cases the lagging development of the transient flow field is further seen by the transient result not reaching the same maximum downforce values seen at steady state. In addition, the maximum downforce in the subsonic range occurs at Mach 0.65 for constant velocity, lags until Mach 0.85 under acceleration, and lags in deceleration to Mach 0.55. The same lags are seen for the minimum downforce in the supersonic regime at Mach 1.30, with the minimum value being reached at Mach 1.40 under acceleration and Mach 1.10 under deceleration. The lag is evident by comparing the Mach numbers at which the reflections passing under the aerofoil no longer impact on the lift performance: Mach 1.50 at steady state, Mach 1.75 under acceleration and then Mach 1.35 under deceleration. Notably, the lag in the transient acceleration results differs from that of the deceleration results.

The underdeveloped flow is also shown by the reduced impact the shock formations and propagations have on the downforce. For example, the sharp fluctuations seen between Mach 0.85 and 0.90 and the inversion in the normal force are not featured in the transient results. The momentary increase in downforce due to the formation and approach of the bow shock at Mach 1.10 is only reflected later at Mach 1.35 in the acceleration results. The bow shock starts forming with a lower stand-off distance than the steady state results. This is evident when comparing the bow shock locations in the steady state and acceleration density contour plots taken at a free stream Mach number of Mach 1.20 on the left of Figure 52. By Mach 1.30 the steady state bow shock stand-off drops below that of the accelerating aerofoil. Between Mach 1.35 and 1.65, the transient flow history again leads to less downforce being produced. After Mach 1.80 enough time has past that the transient local flow field is fully developed and matches that at steady state and the aerodynamic performance curves overlap from this speed onwards.

The deceleration was initiated from the transient results at Mach 2.00. As the aerofoil decelerates there is a delay in the development of the shock reflections under the aerofoil. This means that between approximately Mach 1.42 and 1.15 the downforce is greater than that at the steady state conditions (Figure 51).

It is noted that in Figure 52 the stand-off distance of the decelerating bow shock is the smallest of the three instances shown, as the flow history means it is reflecting the position and shape of a bow shock at a higher Mach number.

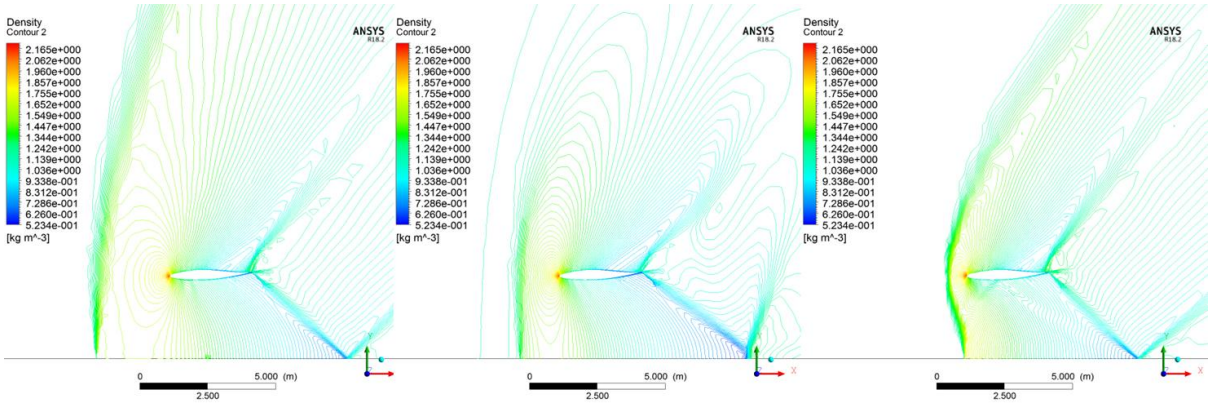


Figure 52: Inverted RAE 2822 aerofoil density contour plots at steady state, 176 g, and -176 g respectively, taken at Mach 1.20.

After Mach 1.15 the downforce slowly increases again until Mach 1.05 as the bow shock stand-off distance slowly increases. From Mach 1.00 the normal shock wave on the upper surface moves upstream of the trailing edge of the aerofoil and as the supersonic regions start to shrink above and below the aerofoil the pressure differential across the aerofoil is gradually restored. By Mach 0.65 the normal shock on the lower surface starts moving towards the leading edge of the aerofoil. At Mach 0.55, the normal shock on the upper surface detaches and then propagates upstream as a curved shock. At this point the downforce drops rapidly, until the lower shock approaches the leading edge and detaches at approximately Mach 0.45. Without the shock waves on the aerofoil the immediate flow around the aerofoil becomes subsonic and between Mach 0.45 and 0.35 the pressure distribution tends back towards the steady state conditions. However, the down wash of the supersonic flow is extremely turbulent, and the aerodynamics fluctuate above and below the steady state case.

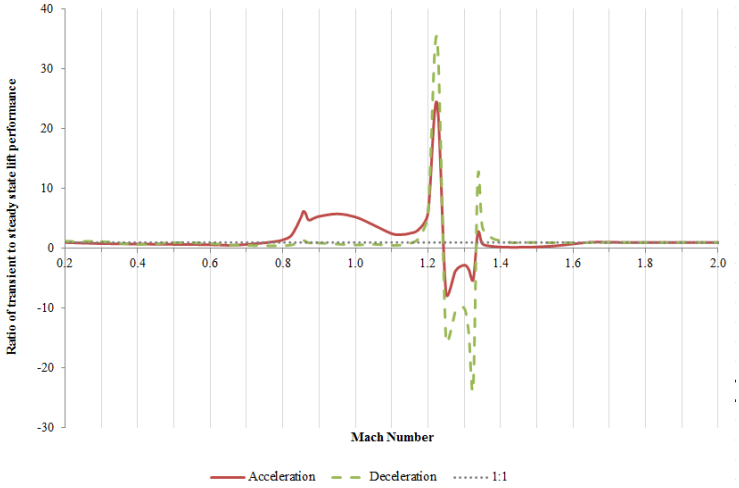


Figure 53: Inverted RAE 2822 ratio of transient to steady state downforce performance.

Figure 53 is a direct comparison of the transient and steady state downforce performance. The maximum deviation for both the acceleration and deceleration cases occurs between Mach 1.20 and 1.35, where the steady state results produce lift instead of downforce. In each case the transient downforce differs by a maximum factor of 24.4 and 35.2 respectively. Between Mach 0.80 and 1.60, the downforce differs by an average factor of 2.11 under acceleration and 0.25 under deceleration. Thereafter the deviations in downforce respectively drop to an average of 1.60 % and 1.04 % respectively.

Figure 53 shows that the transient effects are greatest within the transonic and supersonic regions. Transient flow history is the dominant unsteady effect responsible for this deviation. Transient effects are still present below Mach 0.80 with the maximum deviation of the transient performance fluctuating above and below the steady state by 47 % and 54 % respectively. These fluctuations have been represented in Figure 54 and are dominated by flow history effects. The fluctuation in the acceleration results comes from the underdeveloped flow while the fluctuations in the deceleration results come from the higher velocity flow field overtaking the aerofoil and the resulting down wash.

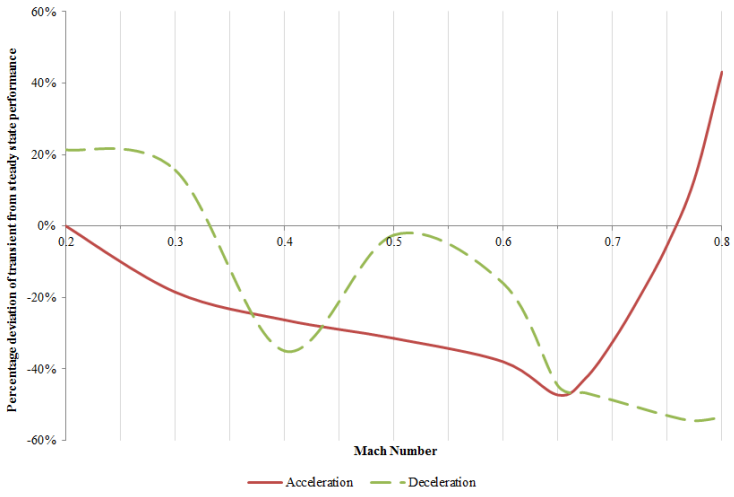


Figure 54: Inverted RAE 2822 percentage deviation of transient from steady state downforce performance under Mach 0.80.

In contrast, the greatest difference for the drag results is in the subsonic region, as in Figure 55 and Figure 56. The subsonic acceleration results, between Mach 0.20 and 0.65, increase from steady state by an average factor of 2.94. While the deceleration results fluctuate between maximum ratios of -10.6 and 4.62 and decrease from the steady state by an average factor of -2.37 for the same speed range. Here the increased drag results during acceleration come from the increased inertia of the fluid. However, the fluctuations in the deceleration results come from a combination of flow history and the inertia of the fluid. This is seen by

the reversal in the direction of the drag force in Figure 55 with the flow pulling the aerofoil forward between Mach 0.60 and 0.40 and again below Mach 0.35.

In the supersonic region the fluctuations in drag drop to an average of 7 % under acceleration and 5 % under deceleration as shown in Figure 57. The deviations in drag come primarily from the induced drag component and thus the flow history effects associated with the downforce.

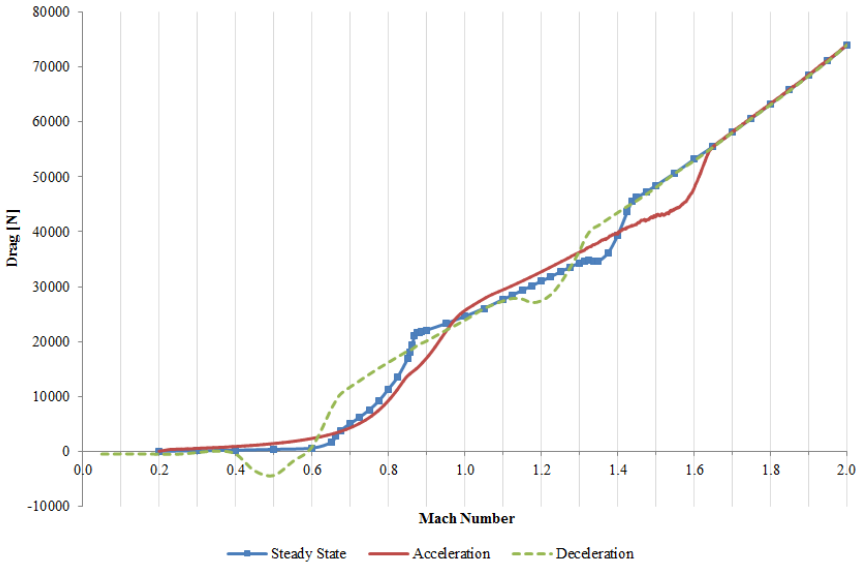


Figure 55: Inverted RAE 2822 aerofoil, α = -2.79° and h/c = 1.00 - steady state, ± 176g acceleration drag performance

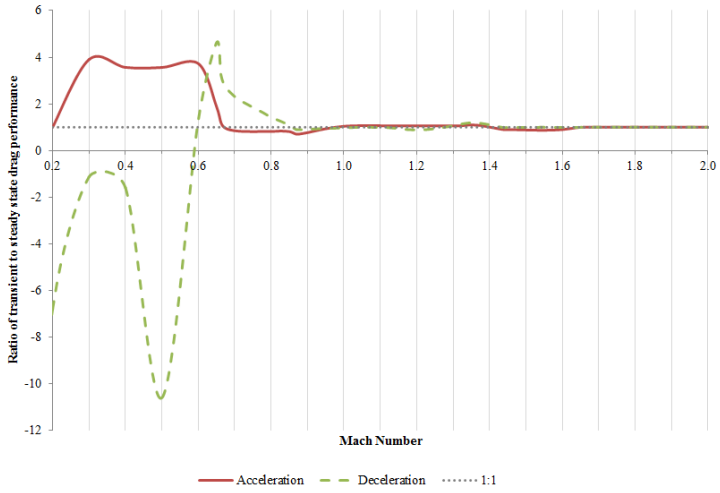


Figure 56: Inverted RAE 2822 ratio of transient 176 g to steady state drag performance.

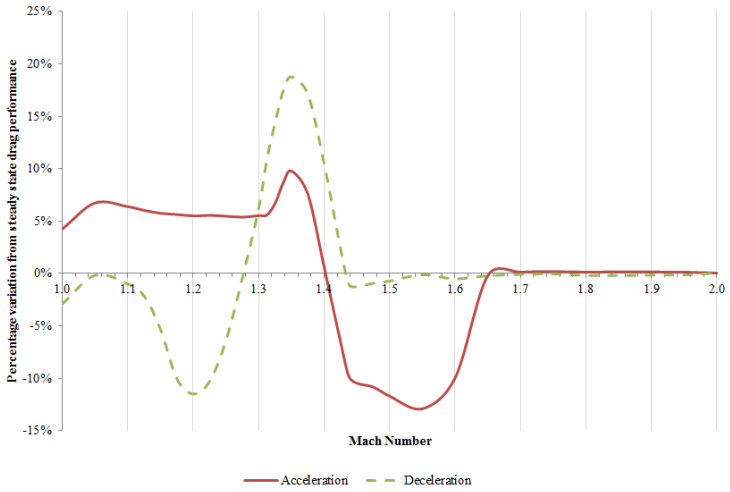


Figure 57: Inverted RAE 2822 ratio of transient 176 g to steady state drag performance above Mach 1.00.

The pitching moment performance for an accelerating and decelerating aerofoil is compared to the steady state pitching moment in Figure 58 and Figure 59. The delay in shock formation is clearly seen by the offset in the loss and rapid gain in pitching moment associated with the shock formations and bow reflection under the aerofoil. Thus, the transient pitching moment is dominated by flow history effects, with the greatest differences coming in at Mach 1.35. In the subsonic region, the variations in the acceleration results are much lower with an average decrease of 12 %. As with the drag performance the effects of deceleration on the pitching moment in the subsonic region are more difficult to determine.

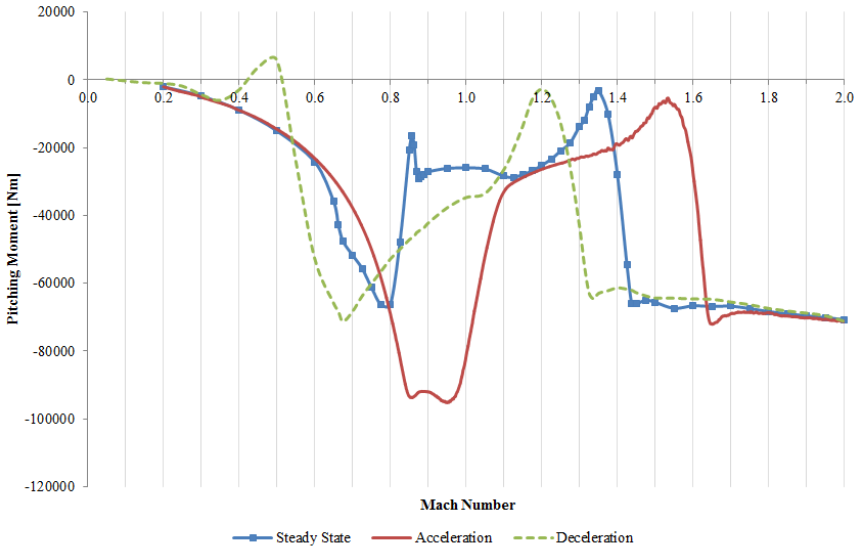


Figure 58: Inverted RAE 2822 aerofoil, α = -2.79° and h/c = 1.00 - steady state, 176g acceleration and 176g deceleration pitching moment performance

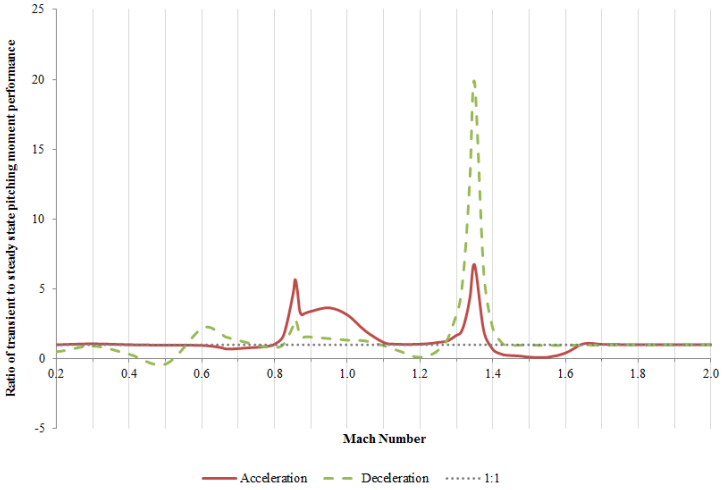


Figure 59: Inverted RAE 2822 ratio of transient 176 g to steady state pitching moment performance.

As discussed earlier, the shift in the transient results can be seen by comparing the resulting shock structures on the accelerating and decelerating aerofoils in Figure 60. Mach number flood and density contour plots of each aerofoil are used to compare the shock systems. The shock locations are determined by analyzing the coefficient of pressure on the surface of the aerofoil or on the ground underneath the aerofoil. The normalized shock locations (x/c) and differences in shock position (Δ x/c) at a free stream Mach number of 0.85 have been summarized in Table 6. During acceleration a negative difference in shock location indicates that the transient shock is ahead of the position it would be at steady state, while during deceleration a negative difference indicates that the transient shock is behind the position it would be at steady state.

In the acceleration (middle) case of Figure 60 the shock on the upper surface has started to form near the half chord position of the aerofoil. The shock in the steady state case is much larger and has already started moving towards the trailing edge of the aerofoil. Thus, the accelerating shock not only forms at a higher speed than the steady state but also further forward. This is seen by comparing the coefficient of pressure plots in Figure 61 and occurs as the accelerating flow field has not had time to fully develop and reflects the flow field of a lower instantaneous velocity. Meanwhile, the shock waves in the deceleration (right) case are seen on both surfaces with the upper shock located further ahead of the steady state case by 3 % of the chord length and the lower shock further back by 9.1 % of the chord length. In each case the shock structures are slightly different. The deceleration case differs the most as the bow shock is seen ahead of the aerofoil and the lower normal shock is reflecting off the ground. The wave angles of the decelerating shock waves are also slightly steeper, and the

decelerating lower shock has a straighter almost concave shape as it starts to move under the aerofoil. In the combined coefficient of pressure diagram in Figure 61, the accelerating lower shock almost overlaps with the steady state case. Such a result goes against the flow history effects seen with the other shock locations. However, even though the shock locations are almost identical, the structure of the shock near the aerofoil wall is different. Upon closer inspection of Figure 60 (left), a lambda shock system forms in the steady state case and the separation bubble in the boundary layers causes the oblique shock C1 of the lambda shock, as defined in Figure 13, to strike the aerofoil slightly further ahead. As a result, the difference in the shock wave locations due to flow history is almost cancelled out.

Table 6: Comparison of the steady state and transient normalised shock locations (x/c) for the inverted RAE 2822 aerofoil at Mach 0.85.

	x/c			Δ x/c	
Surface	**Steady**	**Acceleration**	**Deceleration**	**Acceleration**	**Deceleration**
Lower	0.836	0.835	0.927	- 0.001	- 0.091
Upper	0.794	0.494	0.762	- 0.292	0.031

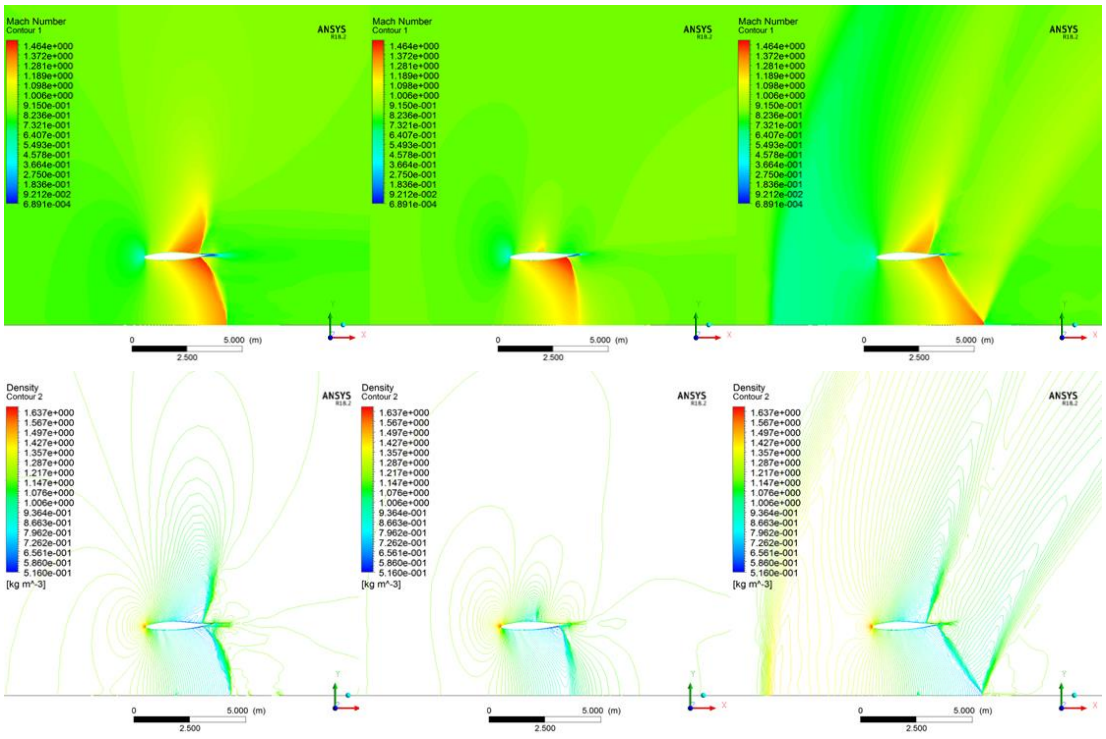


Figure 60: Inverted RAE 2822 aerofoil, α = -2.79°, h/c = 1.00 - steady state (left), 176g acceleration (middle) and 176g deceleration (right) Mach number flood plots and density contour plots at Mach 0.85.

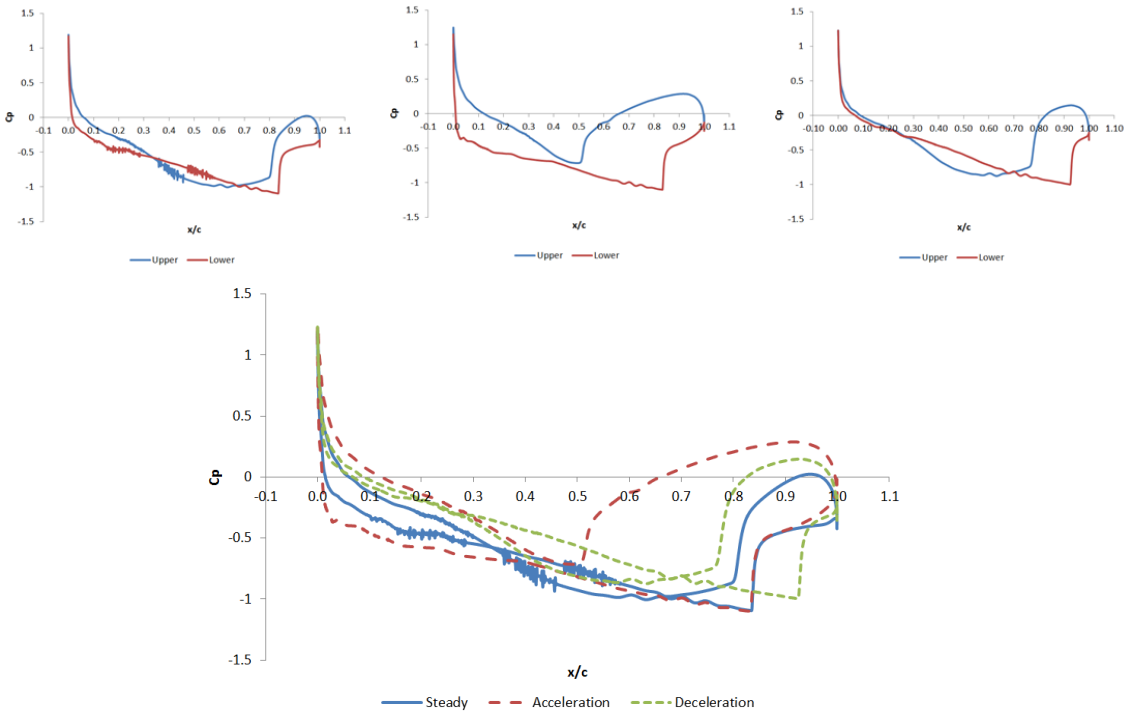


Figure 61: Steady state (top left), 176g acceleration (top middle) and 176g deceleration (top right) coefficient of pressure plots for an inverted aerofoil at Mach 0.85 and α = -2.79°.

Figure 62 shows the variation in the shock structures for the steady state and transient results at a free stream Mach number of 1.20. The shock locations and reflections are further analysed using the coefficient of pressure plots of the aerofoil and the ground directly under the aerofoil, shown in Figure 63. These figures also show how the stand-off distance of the aerofoil decreases from left to right across the results, with the steady state results having the largest stand-off distance and the deceleration the smallest ($\delta_s > \delta_a > \delta_d$). With transient flow history effects, the stand-off distance in positive acceleration should be greater than that of the steady state as the results should resemble the flow field from a lower instantaneous velocity. However, below sonic conditions in acceleration there is no bow shock and as the flow continues to accelerate the bow shock starts forming closer to the aerofoil than it does under steady conditions. To track the development of the steady and unsteady bow shock waves, the stand-off distances from Mach 1.10 to Mach 1.50 have been summarised in Table 7. By approximately Mach 1.30 the stand-off distance of the steady state bow shock drops below that of the accelerating aerofoil, as expected with the flow history effects. The shock locations of the bow shock and normal shock reflection are shown in the pressure distribution along the ground underneath the aerofoil on the right of Figure 63. The less severe pressure gradient of the accelerating bow shock indicates that this shock is still developing. Another interesting development is that the trailing edge shock of the acceleration case features a Mach reflection, which is not seen in the steady state or deceleration cases.

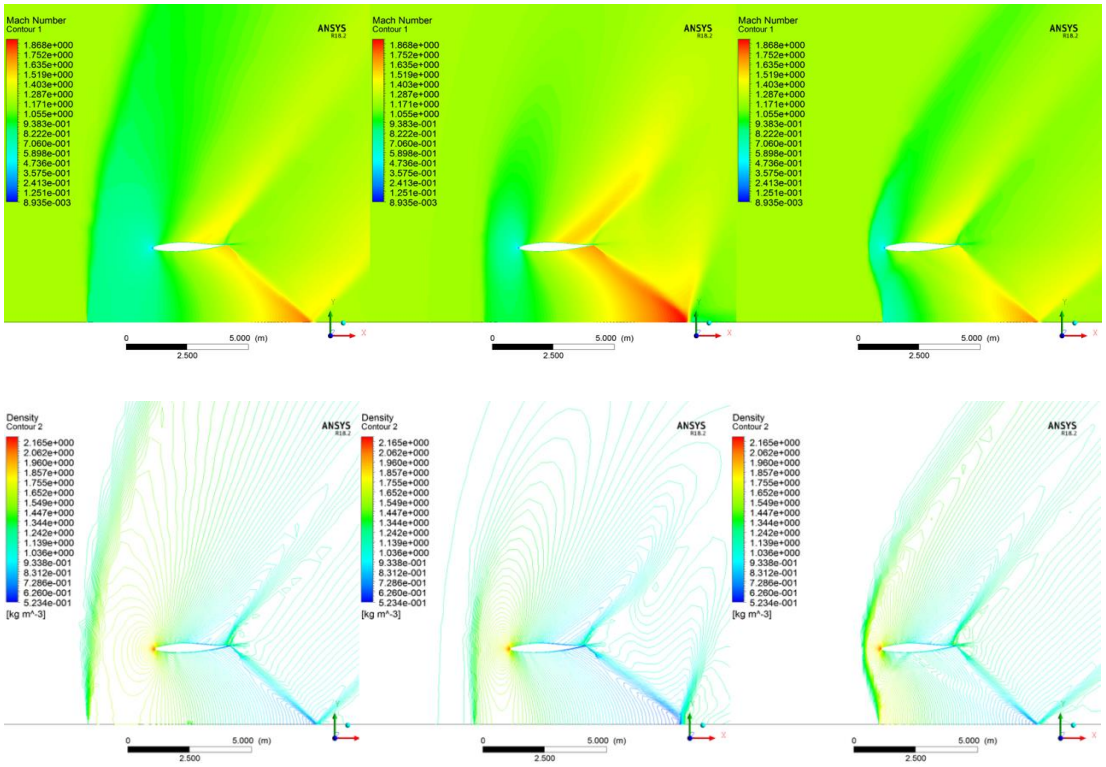


Figure 62: Inverted RAE 2822 aerofoil, h/c = 1.00 and α = -2.79° - steady state (left), 176g acceleration (middle) and 176g deceleration (right) density contour plots results at Mach 1.20.

Figure 64 shows the different stages of the bow shock reflection and how the stand-off distance of the accelerating aerofoil is greater than that of the both the steady state and decelerating aerofoil. The difference is less clear but after analysising the pressure distribution directly ahead of the aerofoil, the results in Table 7 confirm that the stand-off distance of the decelerating aerofoil is slightly less. Figure 64 to Figure 68 show further insight into the difference in the shock formation, propagation and pressure distributions as the aerofoil accelerates and decelerates. At Mach 0.50 the normal shocks are shown to move forward, overtake and eventually detaches from the leading edge of the aerofoil. These results are discussed in more detail in the next chapter.

Table 7: Comparison of normalised steady state and transient bow shock stand-off distances.

	Bow shock stand-off in terms of δ/c				
Mach Number	**1.1**	**1.2**	**1.3**	**1.4**	**1.5**
Steady State, δ_s	-3.18	-0.82	-0.33	-0.11	-0.08
Acceleration, δ_a	N/A	-0.45	-0.39	-0.25	-0.11
Deceleration, δ_d	-0.36	-0.24	-0.16	-0.10	-0.07

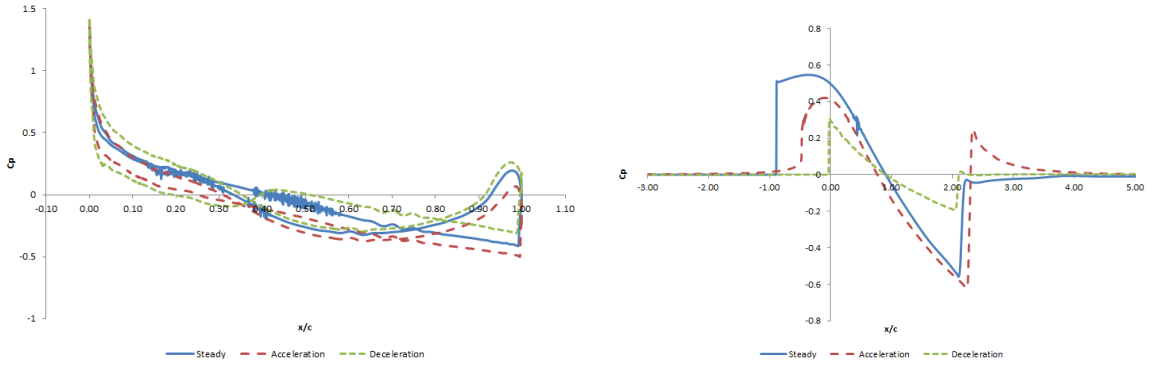


Figure 63: Inverted RAE 2822 aerofoil, h/c = 1.00 and α = -2.79° - steady state vs transient ±176g shock locations along the aerofoil (left) and ground plane (right) at a Mach number of 1.20.

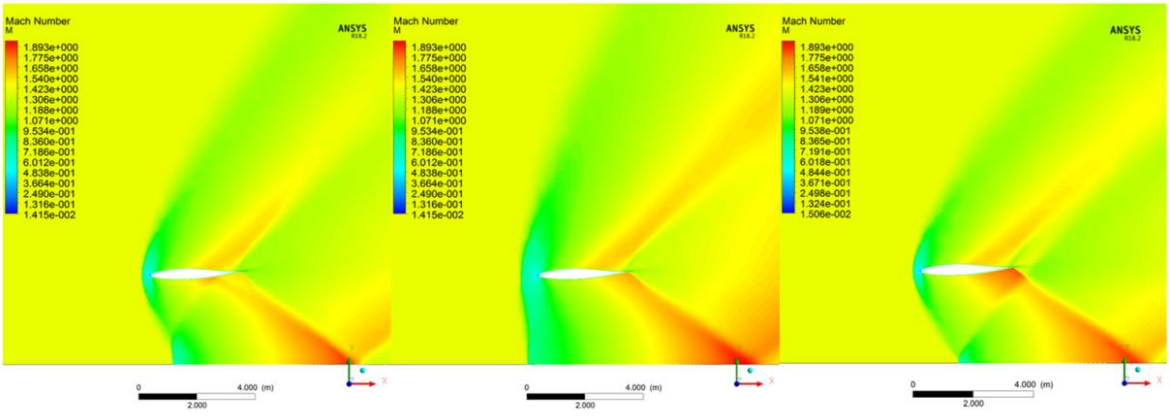


Figure 64: Inverted RAE 2822 aerofoil, α = -2.79°, h/c = 1.00 and - steady state (left), 176g acceleration (middle) and 176g deceleration (right) Mach number and density contour plots at Mach 1.50.

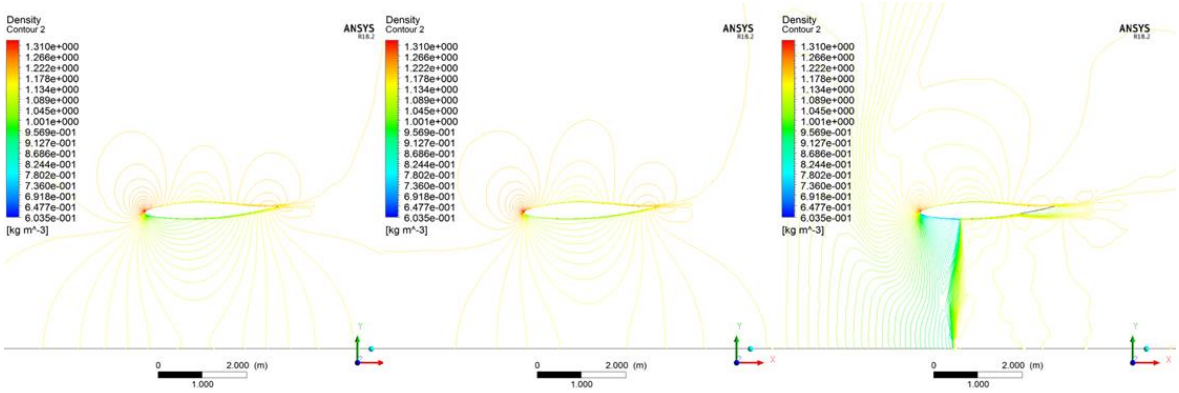


Figure 65: Inverted RAE 2822 aerofoil, h/c = 1.00 and α = -2.79° - steady state (left), 176g acceleration (middle) and 176g deceleration (right) density contour plots at Mach 0.50

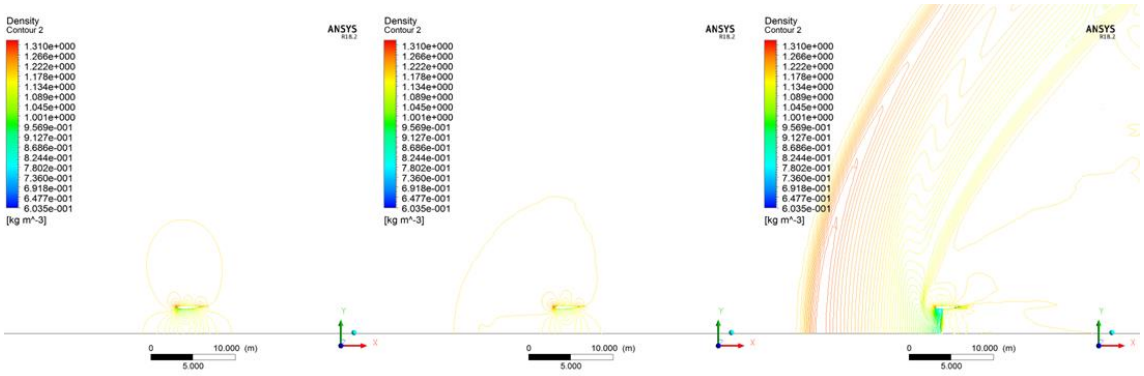


Figure 66: Inverted RAE 2822 aerofoil, h/c = 1.00 and α = -2.79° - steady state (left), 176g acceleration (middle) and 176g deceleration (right) density contour plots results at Mach 0.50.

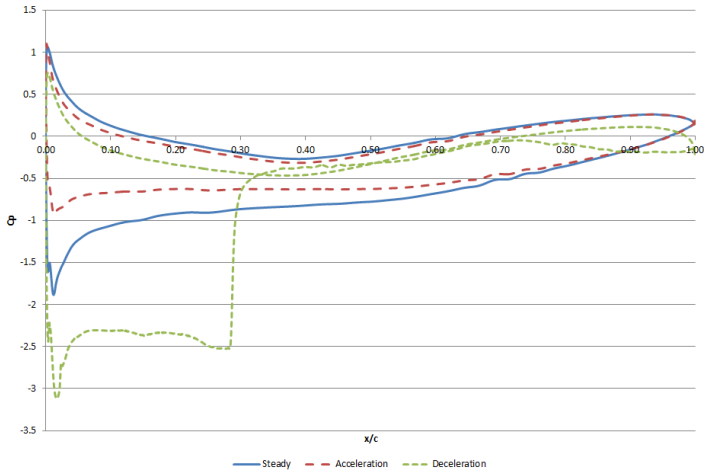


Figure 67: Inverted RAE 2822 aerofoil, h/c = 1.00 and α = -2.79 ° - steady state (left), 176g acceleration (middle) and 176g deceleration (right) coefficient of pressure plot comparison at Mach 0.50.

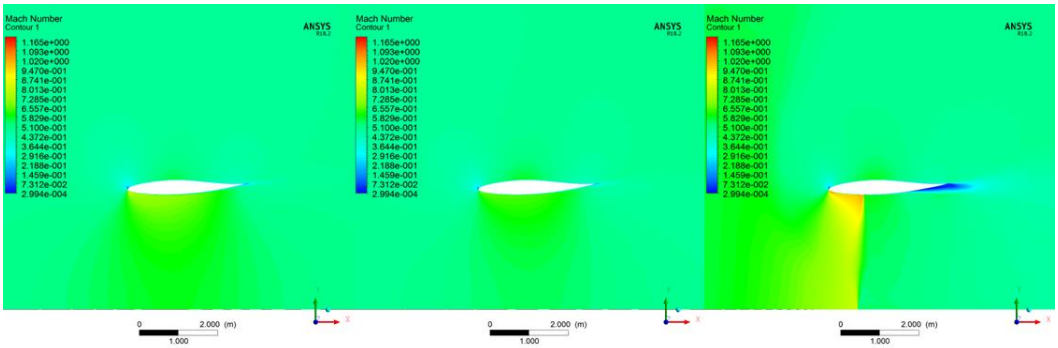


Figure 68: Inverted RAE 2822 aerofoil, h/c = 1.00 and α = -2.79 ° - steady state (left), 176g acceleration (middle) and 176g deceleration (right) density contour plots at Mach 0.50.

40 g Results

As the Pendine test was run with an acceleration of 50 g and deceleration of 30 g, the transient results were run at 40 g to get an indication of the transient effects and differences in the shock locations between these two cases. As the experimental Pendine results were run at a maximum Mach number of Mach 1.08, the RAE 2822 aerofoil was initially accelerated from Mach 0.05 up to Mach 1.20 to cover this range. This range was extended to Mach 1.60 to allow for the transient results to converge with the steady state conditions. Figure 69 provides a comparison of the steady state and transient downforce results. The transient results are slightly shifted to higher Mach numbers than the steady state results and up until Mach 0.70 this leads to a reduction in downforce at each instantaneous velocity. The shift in the transient results means that for most of the remaining speed range the instantaneous value of the transient is greater than that at the steady state velocity.

In the case of deceleration, the shift is reversed with a sudden drop-off in downforce as the trailing edge shock wave overtakes the aerofoil. During this period, the drag is higher than at steady state conditions. Thereafter the drag drops dramatically and between Mach 0.70 and 0.50, two periods of thrust are produced as the air flows upstream over the aerofoil, as illustrated by the negative drag values seen in Figure 70. As the aerofoil continues to decelerate, the downstream features from the wake overtake the aerofoil and sporadically disrupt the pressure distribution over the aerofoil.

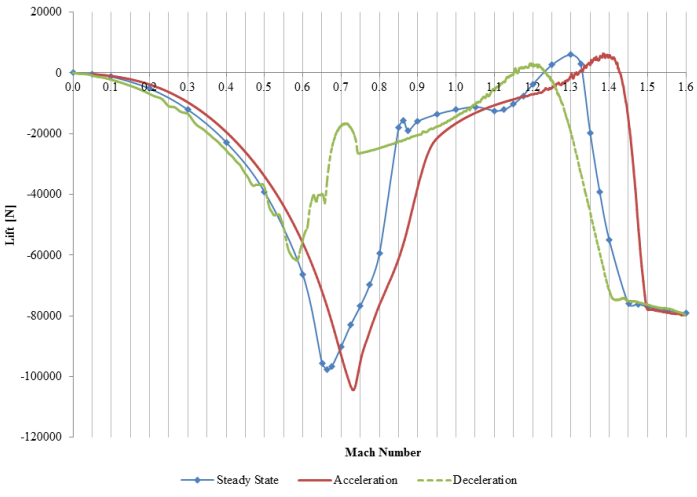


Figure 69: Inverted RAE 2822 aerofoil, h/c = 1.00 and α = -2.79° - steady state and 40 g acceleration downforce performance comparison.

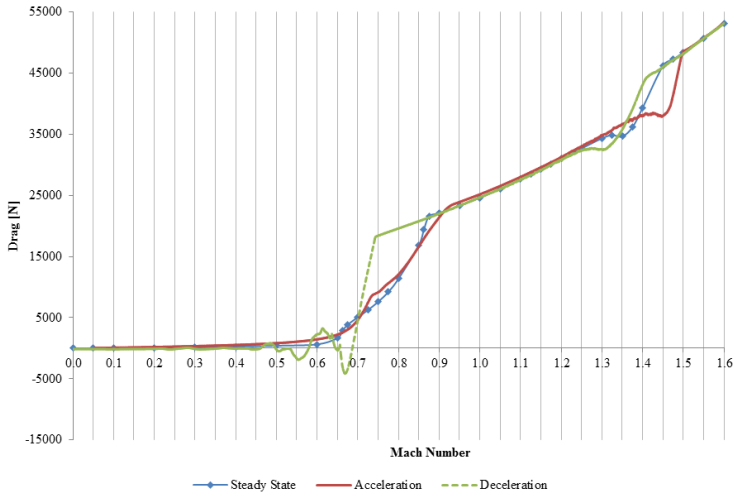


Figure 70: Inverted RAE 2822 aerofoil, h/c = 1.00 and α = -2.79° - steady state and 40 g acceleration drag performance comparison.

The steady state and transient drag and pitching moment performance is compared respectively in Figure 70 and Figure 71. The transient drag and pitching moment results fluctuate above and below the steady state results in both the subsonic and transonic regions and are discussed in more detail in the next chapter. The similarity in the upper and lower shock locations during the 40 g deceleration from Mach 0.75 to 0.65 have been illustrated in Figure 72.

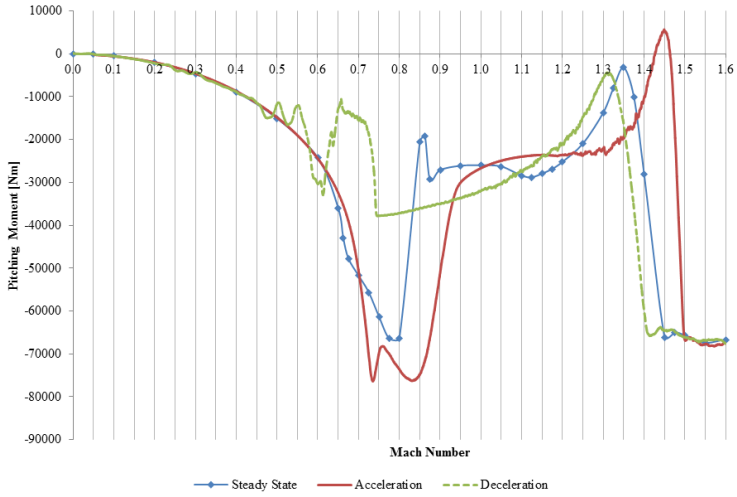


Figure 71: Inverted RAE 2822 aerofoil, h/c = 1.00 and α = -2.79° - steady state, 40 g acceleration and 40 g deceleration pitching moment performance comparison.

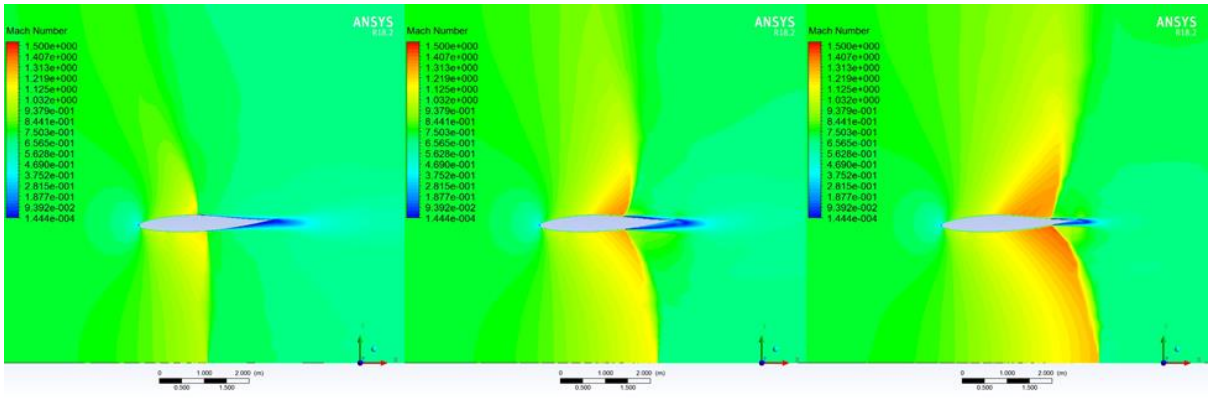


Figure 72: Shock locations for 40 g deceleration at Mach 0.675 (left), Mach 0.70 (centre) and Mach 0.725 (right)

3 g Results

In this section the RAE 2822 aerofoil was accelerated at a much lower acceleration of 3 g, which is more realistic of the Bloodhound SSC case. The unsteady downforce results for the accelerating and decelerating aerofoil are compared against the steady state results in Figure 73. The variations in the two sets of transient results are less evident but notable differences were identified in transonic and supersonic regimes. In the transonic regime the differences came about due to the formation and dynamics of the normal shocks above and below the aerofoil. In the supersonic regime, the differences were caused by the formation of the bow shock and its subsequent reflection under the aerofoil. The effects of deceleration were also evaluated in the above ranges and are considered with the acceleration results in more detail in Figure 74 - Figure 77.

Here the transient flow history effects of acceleration and deceleration can be seen more clearly as there is a much smaller difference in the development of the flow field. In Figure 74, acceleration is seen to cause a decrease in the downforce prior to Mach 0.65 where the flow is subsonic. The opposite is seen to be true for the deceleration. Overall, the underdeveloped flow field in the acceleration results shifts the downforce performance slightly to the right of the steady state results and the underdeveloped flow field shifts the deceleration results to the left of the steady state. Between Mach 0.70 and 0.775 the difference in the transient results falls away as the results overlap. As the upper shock starts to form between Mach 0.775 and 0.90 the transient results again trail behind the steady state. At Mach 0.85, the minimum downforce in the deceleration case decreases below the minimum downforce at steady state.

More detail of the shift in the transient results can be seen in percentage deviation curves in Figure 75 for the Mach number range 1.00 to 1.50. Similar trends are seen in the differences of the transient results – with the downforce results clearly showing that these effects are the inverse of each other and impact the flow field differently. The deceleration results proved to be slightly more unsteady than the acceleration results, as shown by the fluctuations that arise after the shock dissipates at Mach 0.85.

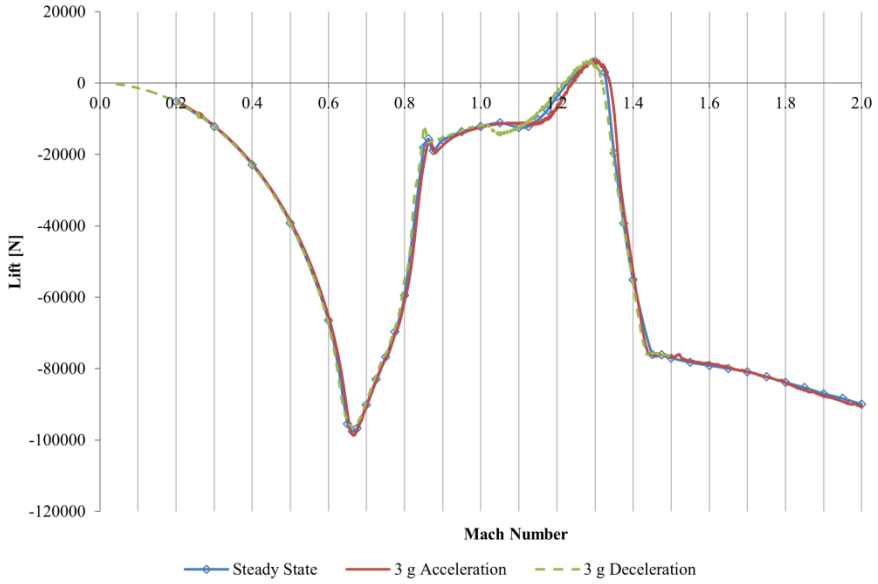


Figure 73: Inverted RAE 2822 aerofoil, h/c = 1.00 and α = -2.79° - steady state and 3 g acceleration downforce performance comparison.

The drag performance was the least sensitive to transient effects, with the maximum deviation of the transient results from the steady state reaching ~17.5% above and below at approximately Mach 0.60. The transient effects of acceleration on the supersonic drag results are significantly lower, Figure 77, as seen by the variations in the results being no more than ±1.50%. For the most part these variations are shown to be the inverse of each other, but at this scale other numerical errors could be responsible for the additional fluctuations in these results.

The pitching moment approached a potentially dangerous nose-up pitching moment (change in sign) at Mach 0.85 and 1.35. In the transonic region, the lowest pitching moment was produced during acceleration, while in the supersonic regime, the lowest was featured during acceleration. Pitching moment proved to be the most sensitive to changes in the flow field as per the fluctuations seen in the pitching moment results, shown in Figure 79. Some of the transient effects of the downforce and drag are reflected in the pitching moment results.

However, further investigation is required to determine the overall effects of acceleration and deceleration on the pitching moment performance.

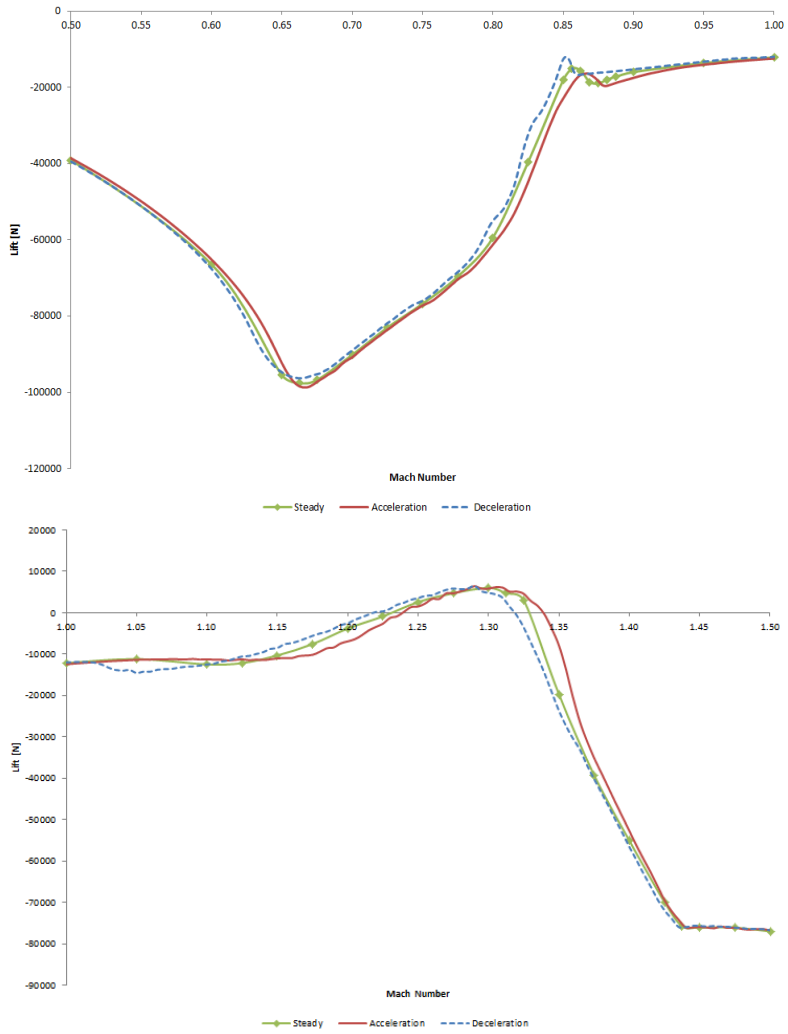


Figure 74: Inverted RAE 2822 aerofoil, h/c = 1.00 and α = -2.79° - steady state, 3 g acceleration and 3 g deceleration downforce performance comparison between Mach 0.50 – 1.00 (top) and Mach 1.00 – 1.50 (bottom)

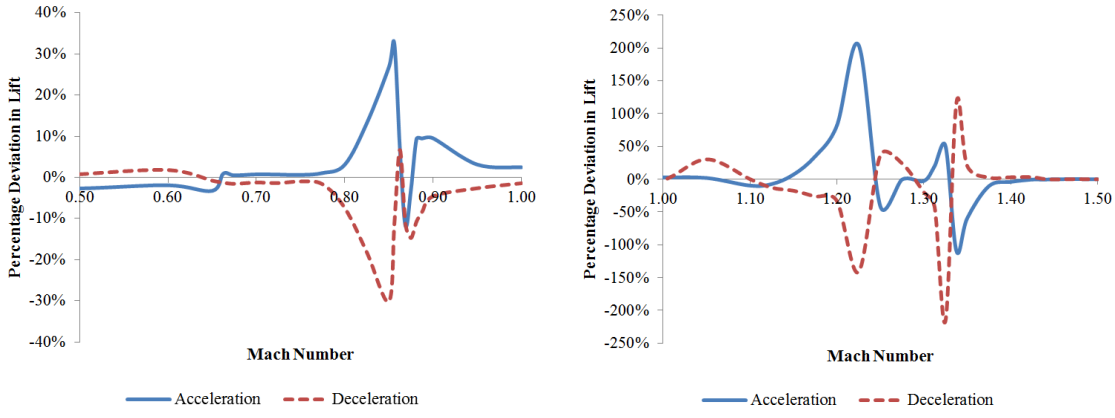


Figure 75: Percentage deviation in transient 3 g lift between Mach 0.50 and 1.00 (left) and Mach 1.00 and 1.50 (right).

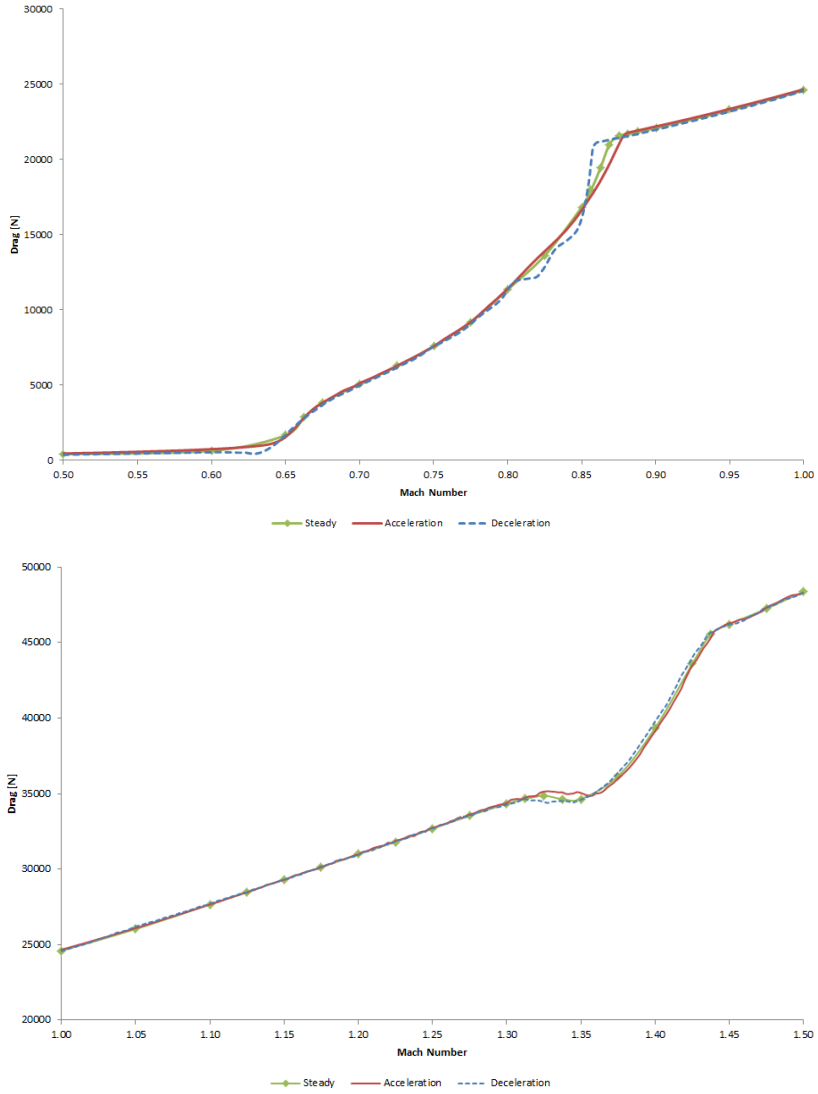


Figure 76: Inverted RAE 2822 aerofoil, h/c = 1.00 and α = -2.79° - steady state, 3 g acceleration and 3 g deceleration drag performance comparison between Mach 0.50 – 1.00 (top) and Mach 1.00 – 1.50 (bottom)

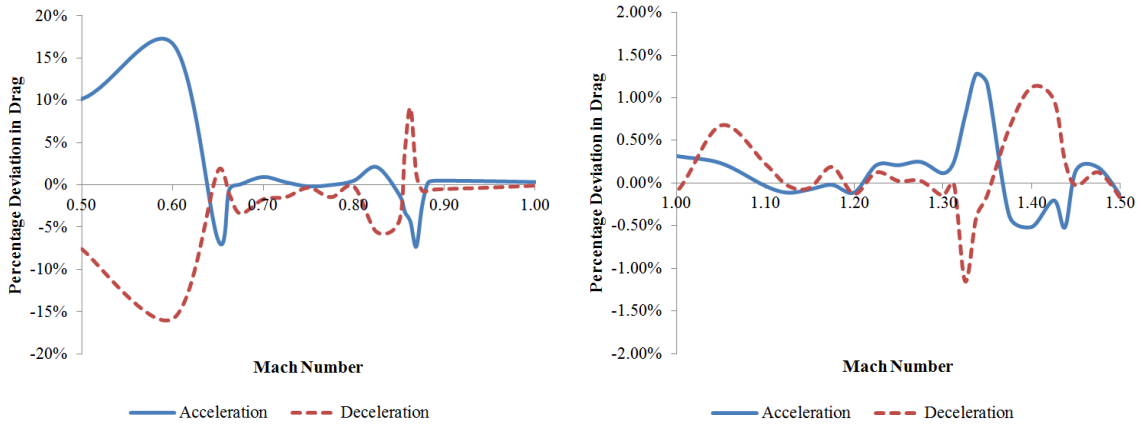


Figure 77: Percentage deviation in transient drag between Mach 0.50 and 1.00 (left) and Mach 1.00 and 1.50 (right).

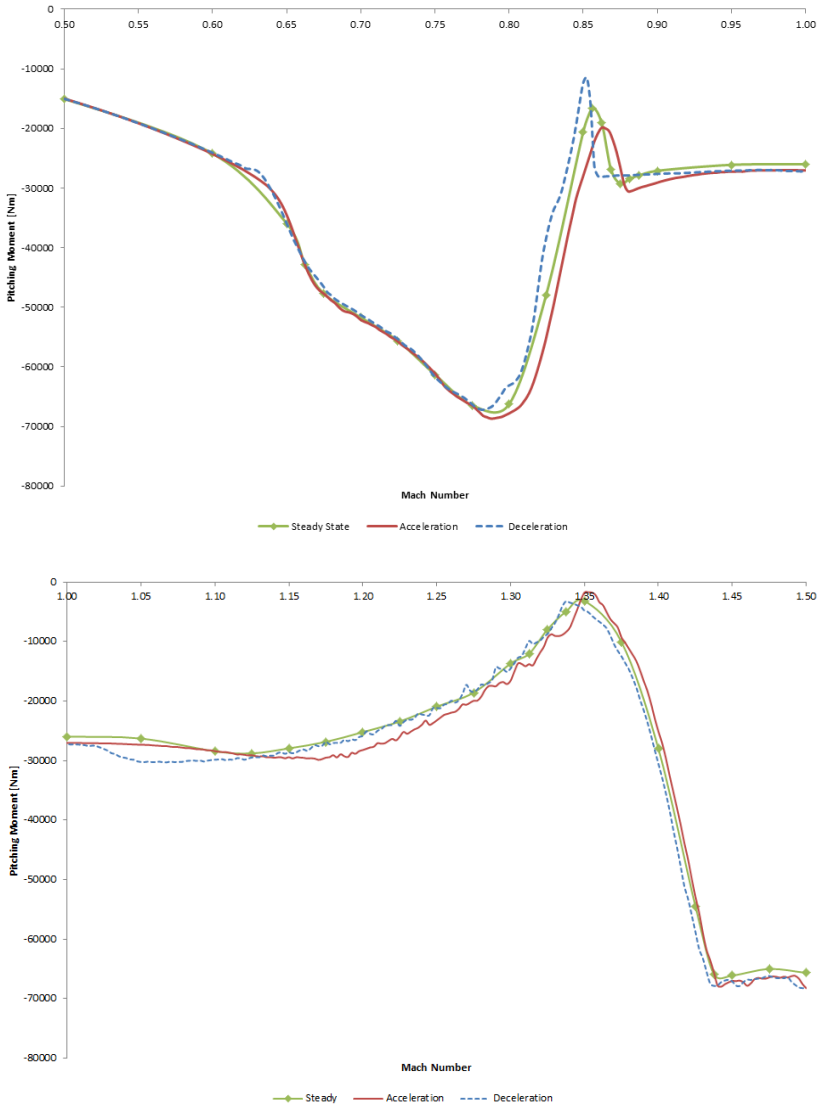


Figure 78: Inverted RAE 2822 aerofoil, h/c = 1.00 and α = -2.79° - steady state, 3 g acceleration and 3 g deceleration pitching moment performance comparison between Mach 0.50 – 1.00 (top) and Mach 1.00 – 1.50 (bottom)

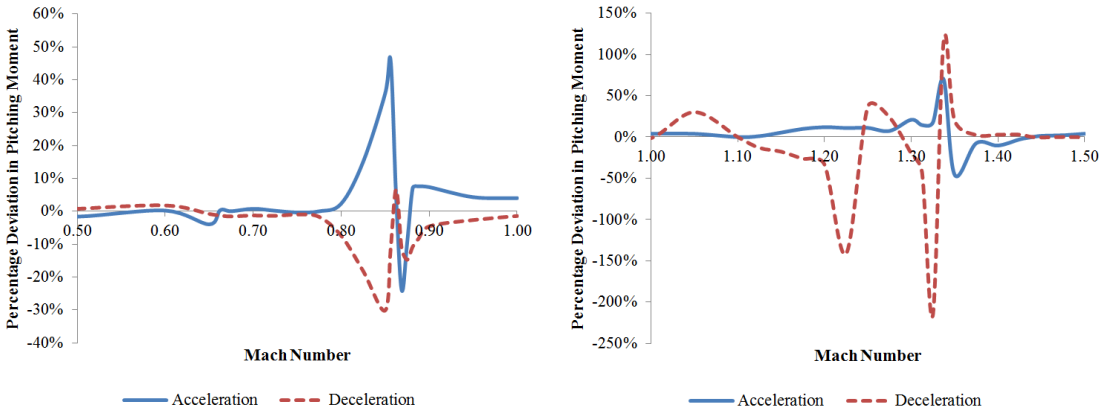


Figure 79: Percentage deviation in transient 3 g pitching moment between Mach 0.50 and 1.00 (left) and Mach 1.00 and 1.50 (right).

At Mach 0.85, the transient downforce and pitching moment deviated by up to 30 % and 50 % from the steady state predictions respectively. Between Mach 1.20 and 1.40 the deviation in downforce increased to a maximum of 200 % during acceleration and -250% during deceleration. Multiple inversions in downforce and pitching moment were also present during these speed ranges.

Transient Case Comparison

The aerodynamic performance of each transient acceleration and deceleration case are compared in Figure 80 to Figure 83, in order to illustrate the impact of the magnitude of the acceleration and deceleration on the flow field. The steady state aerodynamic performance has been included as well as a reference. The main observations taken from these results are the shifts in the aerodynamic performance, and the variations in slope and the maximum and minimum performance reached in each case.

The Mach number flood plots and coefficient of pressure plots in Figure 84 and Figure 85 highlight the difference in the size of the supersonic region above the aerofoils decelerating at -40 g and -176 g. This difference is a result of the higher acceleration allowing less time for the supersonic region to reach the sizes seen in the steady state, -3 g, and -40 g results, as seen in Figure 35.

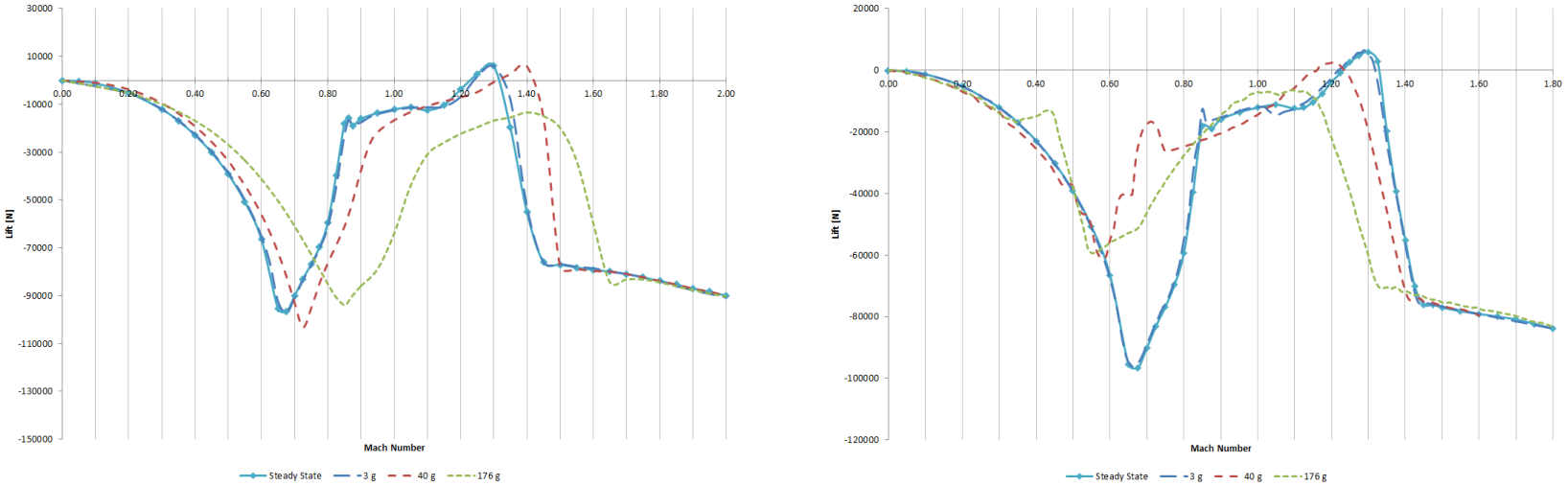


Figure 80: Transient lift performance comparison for acceleration (left) and deceleration (right)

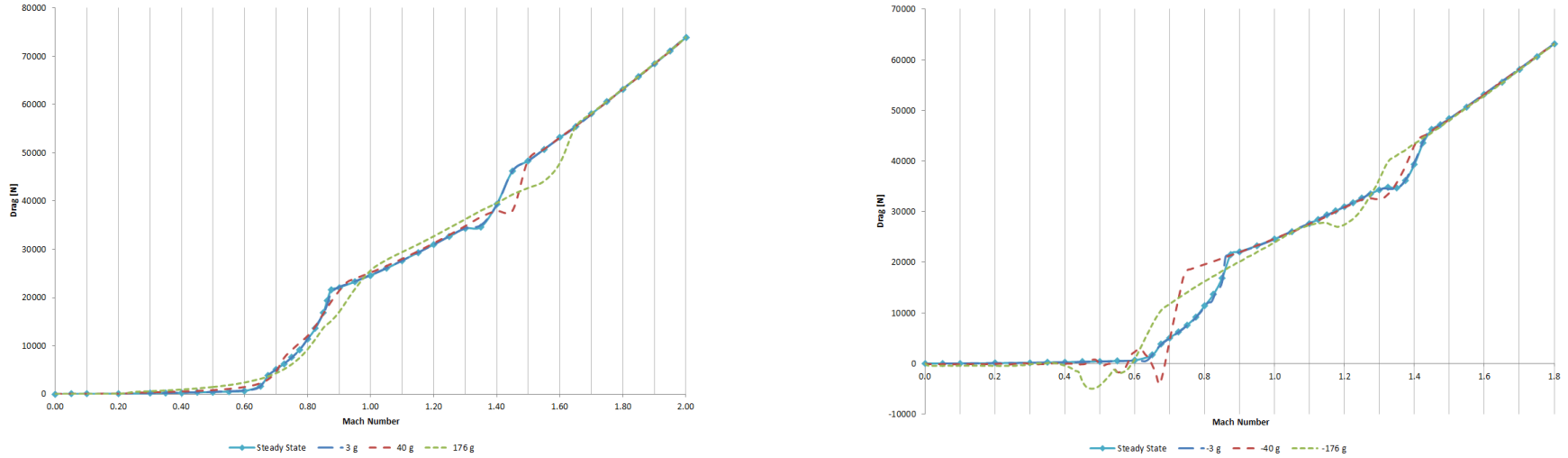


Figure 81: Transient drag performance comparison for acceleration (left) and deceleration (right)

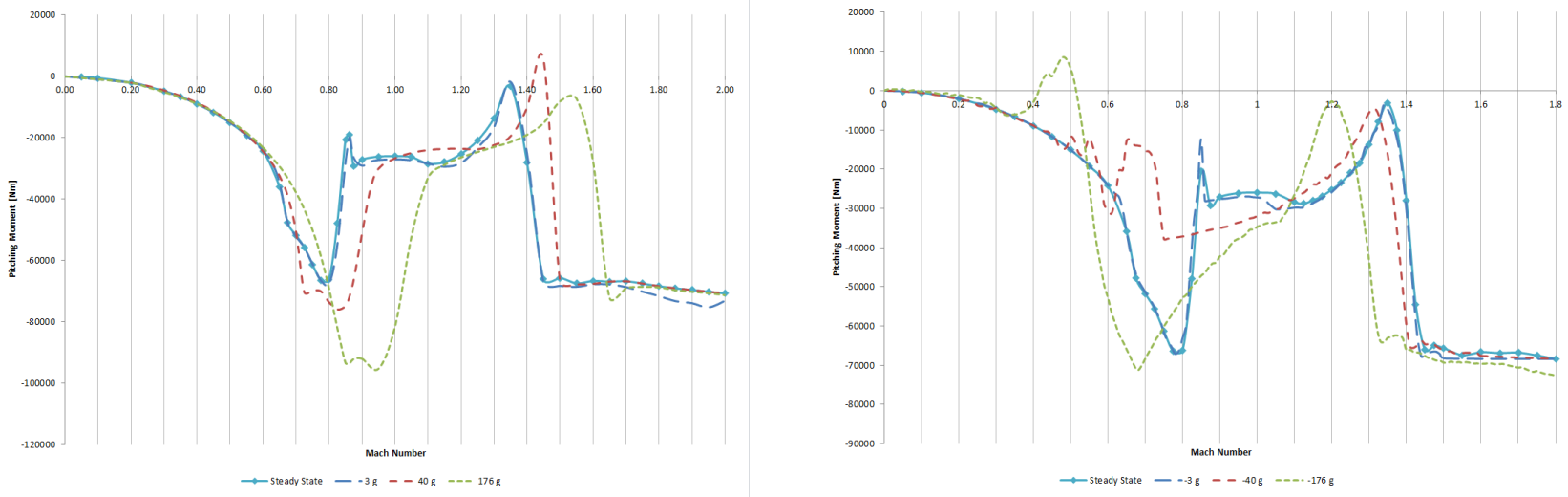


Figure 82: Transient pitching moment performance comparison for acceleration (left) and deceleration (right)

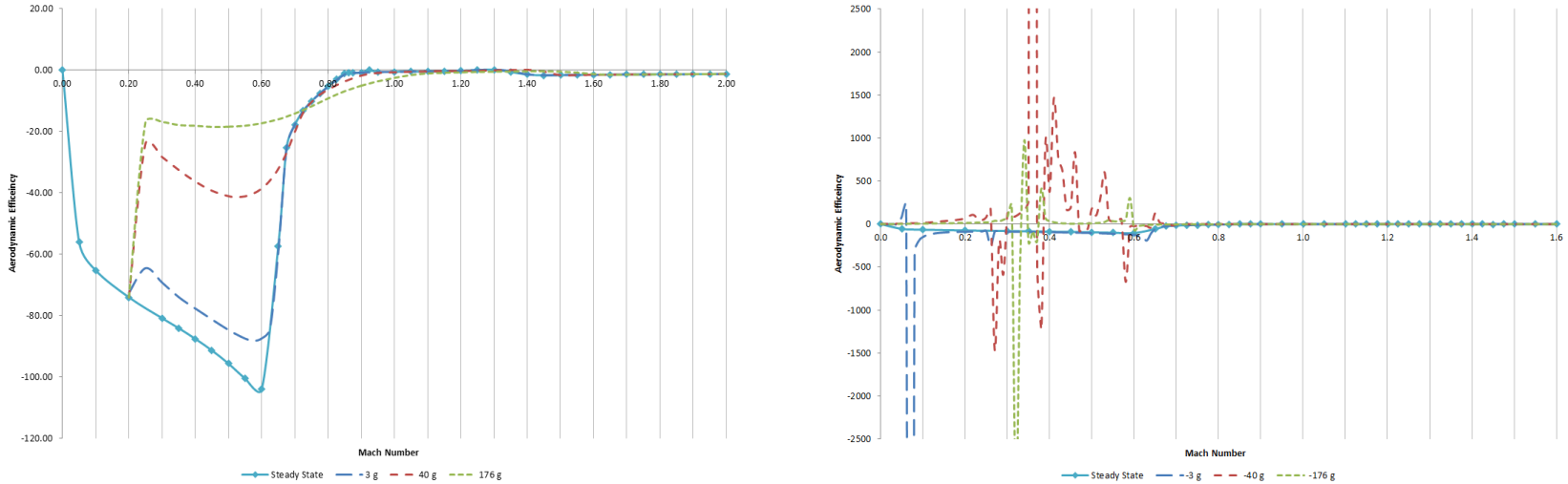


Figure 83: Transient aerodynamic efficiency comparison for acceleration (left) and deceleration (right) cases.

With reference to Table 8, the location of the shock wave on the upper surface of the aerofoil in the -3 g and -40 g deceleration cases is predicted to be further forward than at steady state. In terms of flow history these shock waves should reflect the shock system of a higher velocity and thus be further down the aerofoil, as observed in the -176 g results and locations of the shock wave on the pressure surface. The transient shock locations deviate further from the steady state location as the magnitude of the deceleration increases.

Table 8: Comparison of steady state and transient shock locations at Mach 0.70 and different rates of deceleration

	x/c				Δ x/c from steady state		
Surface	**Steady**	**-3 g**	**-40 g**	**-176 g**	**-3 g**	**-40 g**	**-176 g**
Upper	N/A	N/A	0.603	0.611	N/A	N/A	N/A
Lower	0.648	0.645	0.616	0.865	-0.003	-0.031	0.217

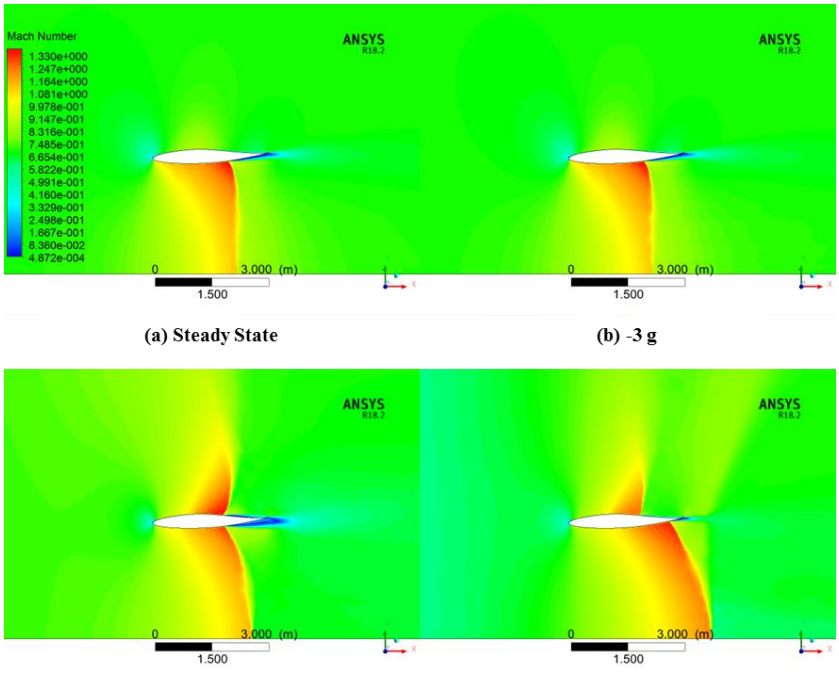
Table 9: Comparison of steady state and transient shock locations at Mach 0.75 and different rates of deceleration

	x/c				Δ x/c from steady state		
Surface	**Steady**	**-3 g**	**-40 g**	**-176 g**	**-3 g**	**-40 g**	**-176 g**
Upper	0.419	0.423	0.860	0.677	0.004	-0.441	0.258
Lower	0.689	0.689	0.981	0.887	0.000	0.293	0.198

Table 10: Comparison of steady state and transient shock locations at Mach 0.80 and different rates of deceleration

	x/c				Δ x/c from steady state		
Surface	**Steady**	**-3 g**	**-40 g**	**-176 g**	**-3 g**	**-40 g**	**-176 g**
Upper	0.577	0.589	0.872	0.731	0.012	-0.295	0.154
Lower	0.775	0.770	0.985	0.908	-0.005	0.210	0.133

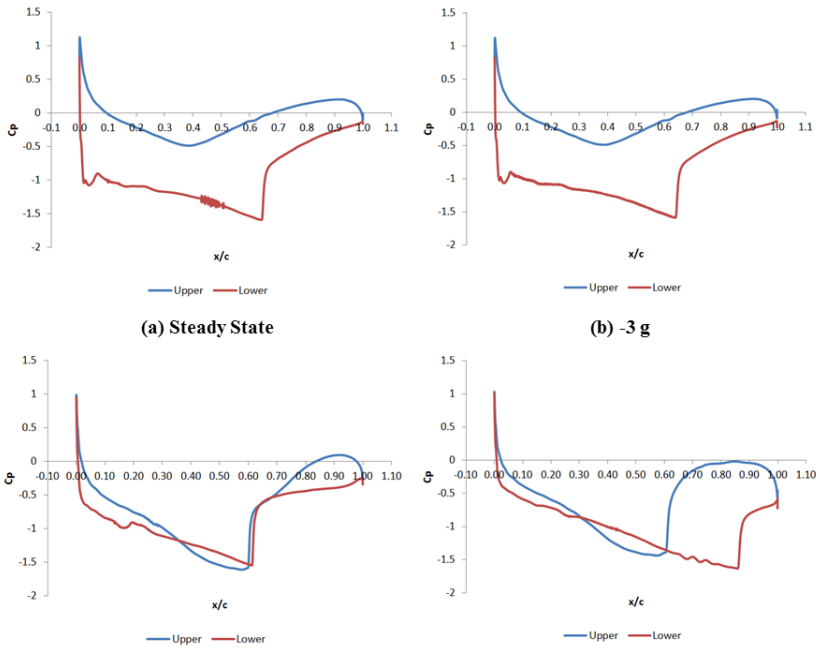
As the aerofoil continued to decelerate, refer to shock locations from Table 10 up to Table 8, the difference in the 40g and 176 g transient shock locations from steady state increased, which is consistent with flow history effects. These results show that the shock waves propagate and overtake the aerofoil at different rates, with the lower shock of the 40 g results having the highest movement of the Mach 0.80 to Mach 0.70 interval. The shock wave geometry, strengths and locations were compared at each rate of deceleration using the Mach number flood plots and coefficient of pressure plots given from Figure 84 to Figure 88.



(a) Steady State (b) -3 g

(c) -40 g (d) -176 g

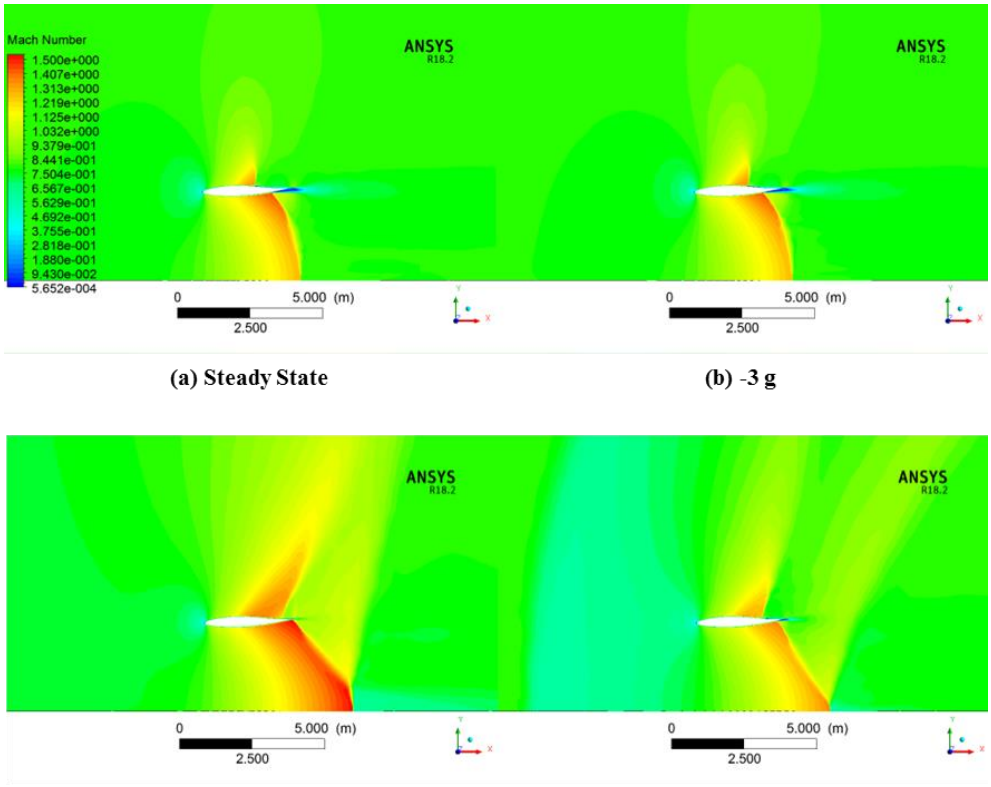
Figure 84: Transient case comparison against (a) steady state of the RAE 2822 aerofoil decelerating at: (b) -3 g, (c) -40 g, and (d) -176 g. Mach number contours are taken at Mach 0.70.



(a) Steady State (b) -3 g

(c) -40 g (d) -176 g

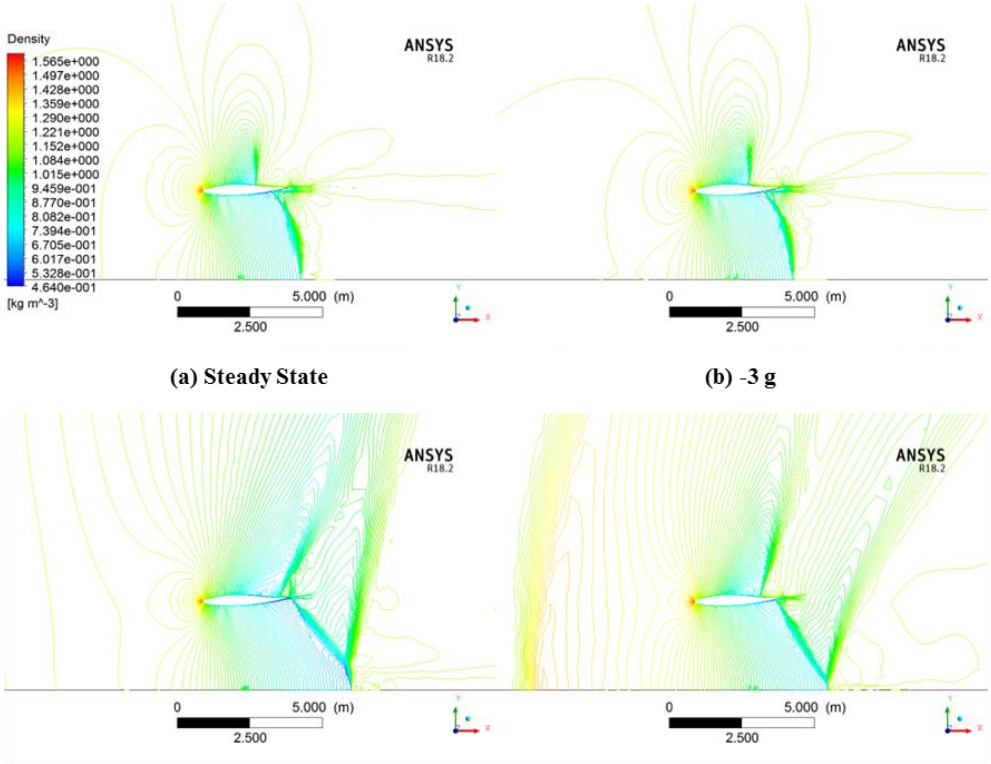
Figure 85: Mach 0.70 coefficient of pressure plot comparison of steady state and transient deceleration results: (a) steady state, (b) -3 g, (c) -40 g, and (d) -176 g.



(a) Steady State (b) -3 g

(c) -40 g (d) -176 g

Figure 86: Mach 0.80 Mach number contour plot comparison of steady state and transient deceleration results: (a) steady state, (b) -3 g, (c) -40 g, and (d) -176 g.



(a) Steady State (b) -3 g

(c) -40 g (d) -176 g

Figure 87: Mach 0.80 density contour plot comparison of steady state and transient deceleration results: (a) steady state, (b) -3 g, (c) -40 g, and (d) -176 g.

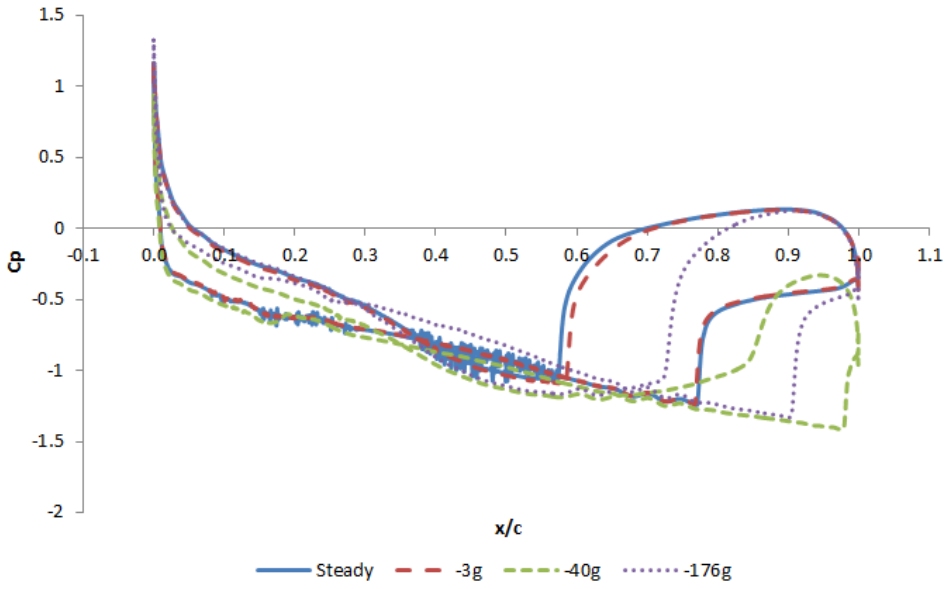


Figure 88: Mach 0.80 coefficient of pressure plot comparison of steady state and transient deceleration results.

Figure 88 and Table 10 illustrate that the upper and lower shock locations of the 40 g results did not always fall between the locations of the shock waves in the 3 g and 176 g deceleration results. Thus, the shifts in the shock locations are not only dependent on magnitude of the deceleration and flow history effects, and additional inertial effects may also be present.

4.2.3 Angle of Attack

From the steady state analysis detailed in section 4.1.3, the reduction in ground clearance is shown to increase the effective angle of attack. For the upright aerofoil at a clearance of h/c = 0.50, this proved to be favourable, but for the inverted aerofoil, at the same clearance, ground effect caused an overall reduction in the downforce produced. With only the highest angle of attack α = -6.0° consistently producing downforce throughout the speed range. In fact, two different trends were seen for the subsonic and transonic to supersonic flow regimes. As shown in Figure 89 and Figure 90, at a zero angle of attack once the shock waves form the aerofoil the aerofoil only produces lift from this point onwards.

Due to ground effect, the range of usable angle of attack for an inverted aerofoil without lift inversions is restricted. As a result, the angle of attack would have to be greater than -2.79° to prevent the reversal of the normal force and pitching moment as observed in Figure 89.

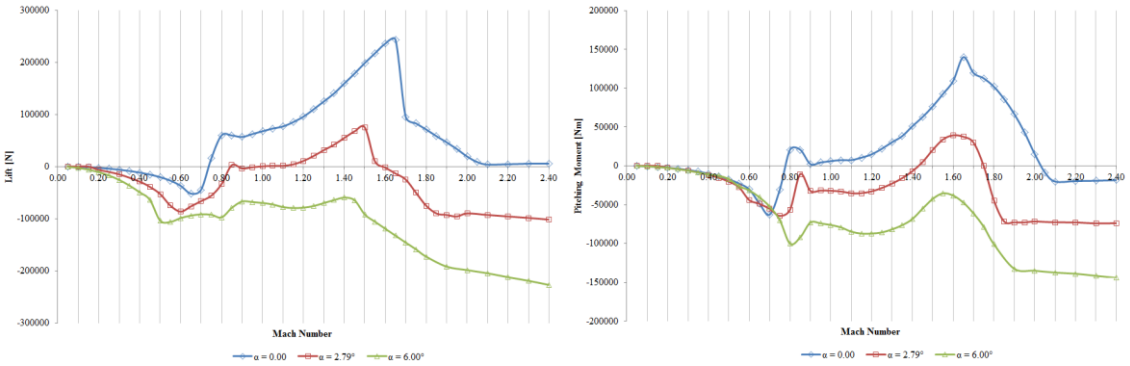


Figure 89: Inverted RAE 2822 aerofoil, h/c = 0.50 – lift (left) and pitching moment (right) performance curves at different angles of attack.

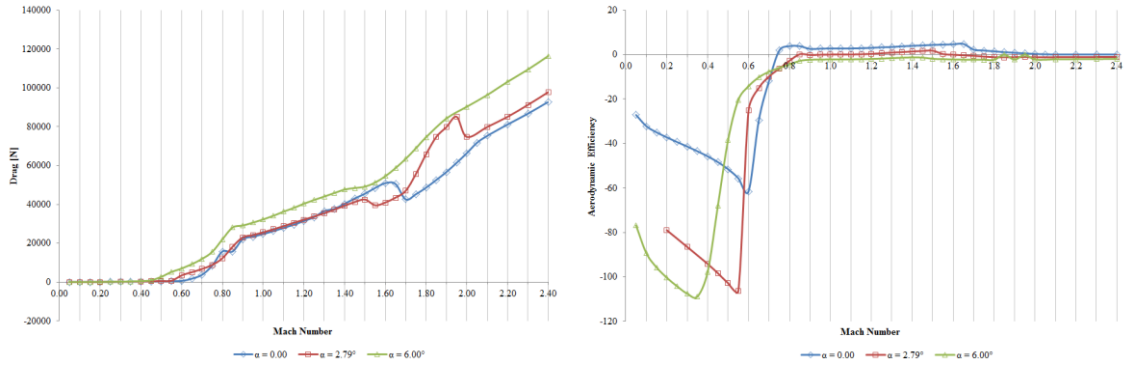


Figure 90: Inverted RAE 2822 aerofoil, h/c = 0.50 – drag (left) and aerodynamic efficiency (right) performance curves at different angles of attack.

5 DISCUSSION

5.1 Aerodynamics

The impact of ground effect and transient acceleration and deceleration on the aerodynamics of the RAE 2822 aerofoil are discussed in detail here. In order to assess the impact of ground effect each ground effect case was compared against the equivalent free flight case. The transient effects were considered by comparing the unsteady results against constant velocity steady state runs.

5.1.1 Ground Effect

The impact of ground effect on the aerodynamics of the upright RAE 2822 aerofoil was assessed in the lift, drag, pitching moment and aerodynamic efficiency curves included in section 4.1.1. In general, the greatest difference in aerodynamic performance featured in the transonic and supersonic regions. The proximity of the ground had minimal effect on the subsonic lift and pitching moment performance of the aerofoils with a clearance of h/c = 0.25 and above as seen in Figure 24 and Figure 30. The subsonic lift increased by an average of 3 %, while the pitching moment decreased by an average of 3%. An average drop in subsonic drag of 21 % was observed, Figure 27, which then lead to an average increase of 35 % in aerodynamic efficiency as shown in Figure 28.

As the flow becomes transonic the impact of ground effect on the upright aerofoil can be seen by the deviation of the aerodynamic performance from the free flight results in Figure 24, Figure 25, and Figure 27 to Figure 30. After the shock waves form on the upper and lower surfaces, a distinct gain in lift and drag is seen for each reduction in ground clearance. The pitching moment performance features a different trend; with a much larger initial drop in performance the transonic and supersonic pitching moment performance decreases with the reducing ground clearance. These distinct gains and losses are maintained for most of the supersonic region and are attributed to an increase in the effective angle of attack of the aerofoil. However, after the bow shock reflects under the aerofoil and this reflection moves past the trailing edge of the aerofoil, this effective increase in angle of attack is lost and the two higher ground effect cases tend towards and eventually overlap with the free flight performance. The same behaviour appears to be present with the h/c = 0.25 results, however, this would depend on the geometry of the shock wave and the Mach number required for the reflected shock to pass the trailing edge of the aerofoil.

In Figure 24, the sudden decreases in lift, due to the bow shock reflecting under the aerofoil, occurred at higher Mach numbers as the ground clearance was reduced. Consequently, these sudden decreases were then reflected in the drag and pitching moment performance. The reason for these sudden decreases is due to the increase in pressure of the subsonic region ahead of the leading-edge stagnation point. This increase comes from the fact that the reduced clearance and geometry of the aerofoil forces more air to flow over the top of aerofoil. Consequently, the leading-edge stagnation point moves slightly downwards and causes the bow shock stand-off distance to increase. These effects further delay the propagation of this shock under the aerofoil, but also greatly increase the lift produced by the aerofoil. For example, the maximum lift produced by the h/c = 0.25 aerofoil is almost 10 times (969%) than that produced at free flight conditions, however this drops rapidly down to 186 % at Mach 2.40 and comes with a severe drag penalty. The resulting aerodynamic efficiency increases to a maximum of 6.18, but this is only 5 % of the maximum efficiency obtained at subsonic speeds. Any aircraft looking to take advantage of this gain in lift would first have to overcome the drag and dangerous reversal in the transonic pitching moment in order to do so. From there, the specific Mach numbers at which these drops occur at would have to be well known in order to safely navigate them.

In Figure 29, the pitching moment for the h/c = 0.50 aerofoil features a less severe peak before it drops off. The reason for this is that the reflected shock strikes the aerofoil near the halfway point of the aerofoil and reflects off the lower surface of the aerofoil for a longer period. At Mach 1.40 the reflection in the higher ground clearance case of h/c = 1.00 strikes the aerofoil towards the trailing edge and by Mach 1.60 propagates behind the trailing edge of the aerofoil.

A significant development is the way in which the angle of the bow shock wave varies as it approaches the ground. First the curvature changes such that the bow shock strikes the ground as a normal shock and then it is forced to transition into a Mach reflection in order to maintain the drop in Mach number across the shock and keep the streamline parallel to the wall. At higher Mach numbers the angle of the approaching bow shock decreases and the Mach stem, seen in Figure 31, reduces in size until it disappears and a regular reflection forms instead.

Next the impact of ground effect on downforce was assessed in section 4.2.1. The inversion of the aerofoil leads to a "venturi" effect and the flow under the aerofoil is accelerated between the aerofoil and the ground. The inversion also means that that the first normal shock wave appears on the lower surface of the aerofoil. Therefore, the critical Mach number of the aerofoil is reached earlier and the normal shock wave on the lower surface forms further forward on the aerofoil, as shown by the decrease in the critical Mach numbers in Table 4. For example, the critical Mach number drops from Mach 0.70 for free flight down to Mach 0.40 at the lowest clearance h/c = 0.05. The location of the shock also moves forward as the flow becomes supersonic earlier.

Figure 41 shows that the drop in downforce becomes more gradual as the aerofoil gets closer to the ground. This is because the flow is more restricted, and the supersonic region does not grow to the same extent seen at the higher ground clearances. With the normal shock starting further forward it also takes longer for it to reach the trailing edge of the aerofoil.

With each lower critical Mach number M_{cr} the drag divergence Mach number decreases as well, as shown in Figure 42 with the drag dramatically increasing earlier and earlier with each reduction in ground clearance. The influence of ground effect on shock formation and drag is shown here clearly with the initial drag rises being staggered by the formation of the shock wave underneath the aerofoil. However, when the shock forms on the upper surface of the aerofoil the wave drag divergence is uniform and consistently ahead of the drag divergence seen at free flight conditions.

Another trend that can be seen in Figure 42 is that the supersonic drag for the higher set of ground clearances h/c = 1.00 and h/c = 0.50 is less than that at free flight. For the lower set the increased proximity of the ground leads to a greater pressure differential across the bow shock. The greater pressure differential increases the strength of the bow shock and consequently the wave drag is greater than predicted at the higher ground clearances and free flight conditions. This shows that there is a ground clearance between h/c = 0.50 and h/c = 0.25 where the drag is approximately equal to that at free flight conditions. Throughout the supersonic region the drag continues to increase and the only deviations coming from the induced lift component. At Mach 1.45 and Mach 2.00 the reflecting shock wave under the aerofoil no longer reflects off the lower surface and, as with the upright aerofoil, the drag converges with the free flight. The lower the aerofoil the longer it takes for the reflections to

pass under the aerofoil and the reduction in lift induced drag is seen respectively for each lower ground clearance.

The upper normal shock forms slightly earlier on the inverted aerofoil for each decrease in ground clearance, as the pressure build up under the nose of aerofoil forces more air over the top. At Mach 0.90, the lower shock has moved to the trailing edge of the aerofoil, while the upper shock movement is delayed by the curvature of the aerofoil. From this inflection point on the aerofoil the adverse pressure gradient along the wall of the aerofoil causes a separation bubble to form in the boundary layer. This separation bubble then leads to the formation of a lambda shock system. With the lower ground clearances this separation bubble and the resulting lambda shock form earlier, Figure 49 and Figure 50 – cases h/c = 1.00 to h/c = 0.05 at Mach 0.80. The oblique shock wave C1 is a lot stronger than that at higher clearances and causes a large region of separated flow. This significantly increases the drag and continues to do so until the shock forms on the upper surface. From that point onwards, there is an almost uniform drag increase across all the ground clearances.

From Mach 0.90 to 1.20 the normal shocks stabilise and propagate downstream, Figure 49 and Figure 50, with the lower shock reflecting off the ground and through the viscous shear layer coming off the aerofoil. With shock waves on both surfaces, the produced downforce drops significantly and the average downforce during this range of Mach numbers is less than 10 % of the downforce produced at free flight. Table 4 lists the Mach numbers where the downforce drops below zero and the pressure differential is reversed such that the aerofoil now starts producing lift. As the ground clearance is reduced the velocity range where the aerofoil produces positive lift increases. The reason for the drop in downforce and in most cases inversion of lift is due to the presence of the bow shock wave. The associated subsonic region grows ahead of the aerofoil and as more and more flow accelerates over the top of the aerofoil, this high-pressure region is forced underneath the nose of the aerofoil. This is further confirmed by the slight downwards movement of the leading-edge stagnation point. As a result, the pressure differential across the aerofoil increases and for both the upright and inverted aerofoil this leads to an increase in the upward normal force produced by the aerofoil. This is desirable for the upright aerofoil, but for the inverted aerofoil the lift inversions would make it very difficult for any vehicle to safely maintain a given ground clearance. Furthermore, the reversal in the pitching moment seen in Figure 43 for the intermediate h/c = 0.50 and 0.25 ground clearance would lead to a positive nose up moment,

which could drastically change the aerodynamics of a wing or vehicle travelling at these speeds and ground clearances.

When comparing the density contour plots at Mach 1.20 in Figure 49 and at Mach 1.40 in Figure 50, the bow shock stand-off distance increases with reducing ground clearance. Such an effect further adds to the delay in the propagation of the bow shock underneath the aerofoil.

5.1.2 Transient Effect

In the previous chapter two different behaviours were identified for the subsonic and transonic and supersonic results. In general, the transient acceleration results showed a shift in the aerodynamic performance towards higher Mach numbers as the development of the transient flow field trails that of the steady state flow field. This difference increased with the magnitude of the acceleration, as the transient flow field has less time to develop and reach equilibrium. At the extreme acceleration, the shock waves had less time to develop and propagate into the flow field. As such, the resulting rapid changes in the aerodynamic forces and moments due to the shock formations and reflections were less severe.

The formation of the transient bow shock was also delayed by the extreme acceleration. The bow shock was shown to start forming at a higher free stream Mach number in Figure 52 and with a significantly lower stand-off distance than the steady state bow shock, Table 7. Such a result goes against the transient flow history effects seen in the formation of the other shock waves and inertial effects were shown to be the cause of this. The extreme acceleration, led to a much higher stagnation pressure at the leading edge of the aerofoil and thus significantly increased the pressure gradient ahead of the aerofoil. As the flow continued to accelerate, the stand-off distance of the steady state bow shock decreased faster than that of the acceleration case and by Mach 1.30 the steady state bow shock had a lower stand-off distance than the accelerating bow shock. Thus, the flow history effects proved to dominate the transient supersonic flow again and the upstream difference in the bow shock location was restored for the accelerating aerofoil. Eventually the difference in shock location in the accelerating flow field is negligible as the transient results converged and overlapped with the steady state results.

The transient effects due to deceleration were then assessed and overall, a shift towards lower Mach numbers was seen in the transient aerodynamic performance, with the decelerating

flow instead resembling the steady state flow field at a higher instantaneous velocity. As per the acceleration the shift continued to increase as the flow decelerates, however, unlike the extreme acceleration the shift proved to have a greater impact on transonic and subsonic flow field. With the rapid deceleration of the aerofoil and the transient flow representing a higher velocity flow field, the shock waves and resulting flow history effects start to overtake the aerofoil and then propagate upstream at higher velocities relative to the aerofoil. The normal shocks and even the top half of a reflected shock of one of the lower ground clearances overtook and detached from the leading edge of the aerofoil. Thus, the aerofoil was exposed to the downstream effects of these shock waves, which greatly impacted on the subsonic performance of the aerofoil. Between Mach 0.60 and 0.40 the direction of the drag reverses as the overtaking flow field pulls the aerofoil forward. This also resulted in a reversal of the direction of pitching moment between Mach 0.50 and 0.40. As such it became more difficult to assess the effect of deceleration on the subsonic and transonic flow field. Hence the 3 g results were then drawn upon to provide further detail of the transient effects under deceleration.

The 3 g results showed that the shift in the acceleration results is mainly due to the transient flow history effects and the normal force and pitching moment performance of the aerofoil are more sensitive to these effects. The 3 g acceleration and deceleration aerodynamic performance results were compared between Mach 0.50 and Mach 1.50 in Figure 74, Figure 76 and Figure 78 and their relative deviation away from the steady state results was presented in Figure 75, Figure 77 and Figure 79. This comparison showed that for the speed range considered the flow history effects from acceleration and deceleration had approximately inverse effects on the aerodynamics of the aerofoil. The comparison of these results also showed that the decelerating flow field was more unstable, with fluctuations in the aerodynamic performance being clearly seen after the dissipation of the upper shock wave at Mach 0.85. These fluctuations only appear after this point, with the transient results developing to produce the same aerodynamic performance, but with a slight shift to lower Mach numbers. The supersonic pitching results in Figure 78, showed the most unsteady behaviour with regular fluctuations seen in both the acceleration and decelerations results as the upper shock formed on the surface. As such further investigation of the source of these fluctuations is recommended.

The lift, drag and aerodynamic efficiency results of the 2-D upright aerofoil, Figure 32 and Figure 33 have been presented by Morrow *et al.*, 2019 [2]. The investigation proved that

throughout the subsonic region, transient flow history caused a drop in lift, while inertia effects caused an increase in the drag. Combined these two effects greatly reduced the aerodynamic efficiency of the aerofoil, as shown in Figure 33. The extreme acceleration meant that once the shock waves had formed, there was less time for them to propagate into the surrounding flow field. Consequently, the severe fluctuations in lift performance seen within the transonic region are less severe and occur at Mach 0.90 instead of Mach 0.75. The transient effects on the formation of the bow shock and pitching moment performance were not presented in the conference paper and are discussed here.

The upper normal shock forms slightly earlier for each decrease in ground clearance, as the pressure build up under the nose of aerofoil forces more air over the top. At Mach 0.90, the lower shock has moved to the trailing edge of the aerofoil, while the upper shock movement is delayed by the curvature of the aerofoil. As discussed in section 5.1.1, an adverse pressure gradient along the wall of the aerofoil causes a separation bubble to form in the boundary layer. This separation bubble then leads to the formation of a lambda shock system. With the lower ground clearances this separation bubble forms earlier, and the lambda shock forms earlier. The oblique shock wave C1 is a lot stronger than that at higher clearances and causes a large region of separated flow. This significantly increases the drag and continues to do so until the shock forms on the upper surface and there is an almost uniform drag increase across all the ground clearances.

From Mach 0.90 to 1.25 the normal shocks stabilise and propagate downstream, with the lower shock reflecting off the ground and through the viscous shear layer coming off the trailing edge of the aerofoil.

Figure 80 to Figure 88 provide a direct comparison of the above acceleration and deceleration cases. In general, the shift in the aerodynamic performance increases as the magnitude of the acceleration and deceleration increases. Each acceleration case follows the general trend of the steady state results, while in the deceleration cases, additional transient effects are seen especially during the transonic regime. The maximum downforce is produced during the 40 g acceleration case near Mach 0.725 and in this case the underdeveloped flow and delayed shock formation results in a higher pressure differential across the aerofoil. A similar effect is observed in the pitching moment performance, with the 40 g results leading to a dangerous inversion of the pitching moment between Mach 1.425 and 1.475.

In Figure 81 to Figure 83 the 40 g results in general fall as an intermediate between the 3 g and 176 g results. However, this is not the case for the 40 g results in the transonic region. The reason for this is due to the similarity in the positions of the shock waves above and below the aerofoil, as evident in Figure 72 and the shock locations given in Table 8. Between Mach 0.75 and Mach 0.65 there is a 1.3 % difference in locations of the shock waves, which leads to a reduction in the pressure differential across the aerofoil and consequently the downforce and pitching moment of the aerofoil. The 40 g deceleration results also feature rapid changes in pitching moment as the upper and lower shock waves overtake the aerofoil. The fluctuations and, in the case of drag, Figure 81, the reversals of the aerodynamic forces lead to an erratic aerodynamic performance and efficiency of the aerofoil, Figure 83 (right), especially in the transonic regime.

The erratic aerodynamic efficiency of the decelerating aerofoil indicated in Figure 83 (right) show how unpredictable and turbulent the flow field is as the aerofoil decelerates through the transonic regime. The difference in the unsteady flow fields of the pure acceleration, and acceleration and deceleration cases to steady state conditions, highlighted in section 2.1 and illustrated by Figure 5 to Figure 7, are evident when comparing the steady state aerodynamic performance against the transient aerodynamic performance in Figure 80 to Figure 83.

6 CONCLUDING REMARKS

6.1 Conclusions

The objective of this investigation was to study the influence of ground effect and transient effects from acceleration and deceleration on the shock system formed on an RAE 2822 aerofoil. The steady state ground effect results proved that decreasing the clearance of the aerofoil impacted on the formation and location of the shock on the aerofoil. The transient acceleration and deceleration results proved that flow history effects caused a delay in the formation of the shock waves on the aerofoil and the transient shock locations differed to those seen at steady state conditions.

The above transient effects were considered over a significant longitudinal acceleration and deceleration of an aerofoil in ground effect. Both upright and inverted cases have been considered. The literature summarised above does not contain the combined effects of ground effect and rectilinear acceleration and deceleration on aerofoil loads for the subsonic to supersonic speed range, Mach 0.20 to 2.00, and therefore this work is considered to be novel.

In the steady state analysis, ground effect proved to increase the effective angle of attack and was shown to promote shock formation under the inverted aerofoil. The shock under the inverted aerofoil also formed further forward with each decrease in ground clearance. Thus, ground effect reduced the critical Mach number of the inverted aerofoil significantly more than the upright aerofoil and consequently, had a greater impact on the subsonic aerodynamic performance of the inverted aerofoil.

In the transonic and supersonic regimes, ground effect and the developing bow shock wave enhanced the lift produced by the upright aerofoil but reduced the downforce of the inverted aerofoil. By approximately Mach 1.20, all the inverted aerofoil cases produced lift instead of downforce. Downforce production was only restored after Mach 1.30 and 1.55 for the two highest ground clearances h/c = 1.00 and 0.50 respectively.

Increasing ground effect also proved to change the stand-off distance of the bow shock and delay the propagation and reflection of the bow shock under the aerofoil. This was seen for both orientations of the aerofoil.

Acceleration and deceleration were proved to shift the aerodynamic performance of the aerofoil to lower and higher Mach numbers respectively. Flow history effects proved

dominant in the transonic and supersonic regimes. The acceleration results in general reflected flow fields with lower instantaneous free stream velocities while the deceleration results reflected flow fields with higher instantaneous free stream velocities.

Consequently, by comparing the subsonic transient acceleration and steady state results at a specific instantaneous velocity, acceleration was shown to decrease the normal force produced by the aerofoil and increase the drag. With pitching moment being a combination of these two forces the overall effect of acceleration was approximately canceled out in the subsonic regime. In the transonic and supersonic regime, the deviation from the steady state results, in the drag performance is significantly lower than the deviation in lift performance. Thus, the changes in pitching moment are substantially more dependent on the changes in the lift.

Shifts in the aerodynamic performance and shock locations increased with the magnitude of the acceleration and deceleration. The aerodynamic performance curves are functions of the Mach number and when flow history effects dominate the performance shifts to lower Mach numbers under acceleration and higher Mach numbers under deceleration. Additionally, the shift in the transient shock location from steady state is in general towards the nose under acceleration and towards the trailing edge under deceleration.

The transient flow history effects of acceleration proved to delay the formation of the bow shock, but inertial effects were shown to change the stand-off distance of the bow shock. As a result, the accelerating bow shock temporarily, between Mach 1.20 and 1.30, forms further ahead of the steady state case. At higher Mach numbers the steady state bow shock stand-off drops below that of the acceleration case as predicted by the transient flow history effects.

In each transient case, the shockwaves propagate across the upper and lower surfaces of the aerofoil at different rates, which led to noticeable changes in the pitching moment of the aerofoil. The greatest differences in the aerodynamic performance due to shock location and propagation were observed in the transonic regime of the 40 g deceleration results of the inverted aerofoil.

Increasing angle of attack with ground effect also proved to offset and delay the propagation of the bow shock wave under the aerofoil. To avoid the rapid inversions of lift to downforce, the angle of attack for this aerofoil should be limited respectively to positive values for the

upright aerofoil ($\alpha > 0.0°$) and negative values less than approximately -2.79° ($\alpha < -2.79°$) for the inverted aerofoil.

The rapid decreases and changes of sign of the lift and pitching moment in this investigation pose severe dangers to vehicles and bodies travelling at high accelerations or decelerations in ground effect. The 3 g transient analysis given in Figure 75 and Figure 79 identified two major deviations and periods of inverted forces from the steady state results, at approximately Mach 0.85 and 1.25 for both the acceleration and deceleration results. These deviations in downforce and pitching moment respectively reached maximums of 200 % and 50 % during acceleration and -225% and -225 % during deceleration. Land vehicles, such as the BSSC could be subjected to these sudden and unexpected drops in downforce or nose-down pitching moments and thus would lead to the vehicle lifting off the ground and potentially flipping over to disastrous effects.

At ground clearances of h/c = 0.50 and 0.25, multiple shock wave reflections developed between the inverted aerofoil and the ground, as seen in Figure 49 and Figure 50. With the long nose, low ground clearance and flat base plate of the TSSC, it is possible that the discrepancy seen in the results in Figure 3 could be attributed to shock reflections occurring underneath the length of the body of the vehicle.

6.2 Recommendation for Further Work

In order to determine the exact location of the underbody shock a full three-dimensional model of the Thrust SSC Pendine model would be required. To ensure no boundary effects influence the aerodynamics of the model, the domain would need to be sized at least 20 characteristic lengths ahead, above and to the left and right of the geometry. To fully capture the effects of the large wake produced by the vehicle, 40 characteristic lengths behind the geometry would be required. The transient results would also have to be conducted over the full speed range of the Thrust SSC using a suitable time step. These simulations would be extremely expensive to run computationally. Consequently, a three-dimensional study on RAE 2822 wing has already been initiated as the next step towards modeling the full three-dimensional model of the Thrust SSC.

The deceleration cases were initiated from transient acceleration results after they had reached steady state conditions. The transient acceleration cases were initiated from steady state conditions at Mach 0.20. The transient results were run until the transient effects had

subsided and the flow had reached steady state conditions. Steady state conditions were reached at different Mach numbers and the deceleration cases were then initiated from these Mach numbers respectively. Further insight could be gained of the flow history effects by comparing the deceleration cases presented here to cases initiating from steady state conditions.

In section 4.2.2, fluctuations in the pitching moment were observed in supersonic regime of the 3 g acceleration and deceleration cases. These unsteady fluctuations occurred as the shock wave formed on and propagated along the pressure surface of the inverted aerofoil. Further investigation is thus recommended to determine the source of these fluctuations.

In the inverted 176 g transient analysis of the bow shock formation, Figure 60, a Mach reflection of the trailing edge shock occurred only while the aerofoil was accelerating. The reason for the transition of this shock from the regular reflection should be investigated further.

Multiple shock structures occurred because of the reflections of the trailing edge shock and bow shock. These shocks also interacted with the shear layer coming off the trailing edge of the aerofoil. As a result, the propagation and interaction of these shocks could be studied in further detail, especially as their development will impact on the downstream flow field and potentially the aerodynamics of an aerofoil rapidly decelerating.

This study focused on constant acceleration and deceleration cases and could be extended by considering non-constant acceleration and deceleration cases. In reference to the Thrust SSC and Bloodhound SSC, the magnitudes of acceleration could be based on the propulsion of the vehicles, while the deceleration could be based on the drag produced by the vehicle and the various breaking mechanisms employed when slowing down.

The study could be repeated using a solver with an in-built moving reference technique, such as Star CCM. and compared against these results.

REFERENCES

[1] S. R. Morrow, H. Roohani, B. W. Skews, I. M. A. Gledhill, and B. J. Evans, "The Effects of Rectilinear Acceleration on Shock Formation in Ground Effect", *Proceedings of the 23rd International Shock Interaction Symposium*, Kruger National Park, South Africa, 9-13 July 2018, ed. R. T. Paton and B. W. Skews, 159-164, 2018 ISBN 978-0-620-80449-3 (ebook) 978-0-620-80448-6 (Print)

[2] S. R. Morrow, H. Roohani, B. W. Skews, I. Gledhill, and B. J. Evans, "The Aerodynamic Performance of an Aerofoil in Tri-sonic Ground Effect," in *Proceedings of the 32nd International Symposium on Shock Waves (ISSW32 2019)*, Research Publishing Services, 2019, pp. 261–274. doi: 10.3850/978-981-11-2730-4_0376-cd.

[3] "ThrustSSC," BLOODHOUND SSC. Accessed: Jul. 03, 2017. [Online]. Available: http://www.bloodhoundssc.com/node/311/thrustssc

[4] "Bloodhound SSC," BLOODHOUND SSC. Accessed: Jul. 03, 2017. [Online]. Available: http://www.bloodhoundssc.com/project/car

[5] B. J. Evans, *priv. comm.*, Feb. 13, 2017.

[6] J. A. Schetz, "Aerodynamics of High-Speed Trains," *Annu. Rev. Fluid Mech.*, vol. 33, no. 1, pp. 371–414, 2001, doi: 10.1146/annurev.fluid.33.1.371.

[7] K. V. Rozhdestvensky, "Wing-in-ground effect vehicles," *Prog. Aerosp. Sci.*, vol. 42, no. 3, pp. 211–283, May 2006, doi: 10.1016/j.paerosci.2006.10.001.

[8] J. Powell, G. Maise, J. Paniagua, and J. Rather, "Maglev Launch and the Next Race to Space," presented at the Aerospace Conference, Apr. 2008, pp. 1–20. doi: 10.1109/AERO.2008.4526501.

[9] G. M. Lilley, R. Westley, A. H. Yates, and J. R. Busing, "Some Aspects of Noise From Supersonic Aircraft," *Aeronaut. J.*, vol. 57, no. 510, pp. 396–414, Jun. 1953, doi: 10.1017/S036839310012526X.

[10] H. Roohani and B. W. Skews, "Unsteady aerodynamic effects experienced by aerofoils during acceleration and retardation," *Proc. Inst. Mech. Eng. Part G J. Aerosp. Eng.*, vol. 222, no. 5, pp. 631–636, May 2008, doi: 10.1243/09544100JAERO280.

[11] H. Roohani and B. W. Skews, "The influence of acceleration and deceleration on shock wave movement on and around aerofoils in transonic flight," *Shock Waves*, vol. 19, no. 4, pp. 297–305, Aug. 2009, doi: 10.1007/s00193-009-0207-9.

[12] I. M. A. Gledhill, H. Roohani, and B. W. Skews, "Stagnation Pressure on a Uniformly Accelerating Aerofoil", *Proceedings of the 23rd International Shock Interaction Symposium*, Kruger National Park, South Africa, 9-13 July 2018, ed. R. T. Paton and B. W. Skews, 121-127, 2018 ISBN 978-0-620-80449-3 (ebook) 978-0-620-80448-6 (Print)

[13] J. G. Leishman, "Boundary Layers," Jan. 2023, doi: 10.15394/eaglepub.2022.1066.n22.

[14] T. Saito, K. Hatanaka, H. Yamashita, T. Ogawa, S. Obayashi, and K. Takayama, "Shock stand-off distance of a solid sphere decelerating in transonic velocity range," *Shock Waves*, vol. 21, no. 5, pp. 483–489, Sep. 2011, doi: 10.1007/s00193-011-0323-1.

[15] J. D. Anderson, *Fundamentals of Aerodynamics*, 5th ed. Mc Graw Hill, 2016. Accessed: Jul. 17, 2017. [Online]. Available: http://www.mheducation.com/highered/product/fundamentals-aerodynamics-anderson/M1259129918.html

[16] U.S. Federal Aviation Administration - Airplane Flying Handbook. U.S. Government Printing Office, Washington D.C.: U.S. Federal Aviation Administration, p. 15-7. FAA-8083-3A, May 2004.

[17] G. Ben-Dor, O. Igra, and T. Elperin, *Handbook of Shock Waves, Three Volume Set*. Academic Press, 2000.

[18] J. Matheis and S. Hickel, "On the transition between regular and irregular shock patterns of shock-wave/boundary-layer interactions," *J. Fluid Mech. Camb.*, vol. 776, pp. 200–234, Aug. 2015, doi: http://0-dx.doi.org.innopac.wits.ac.za/10.1017/jfm.2015.319.

[19] H. Roohani, "Aerodynamic effects of accelerating objects in air.," Thesis, U. Witwatersrand, 2011. Accessed: Jul. 05, 2017. [Online]. Available: http://wiredspace.wits.ac.za/handle/10539/10520

[20] I. Mahomed, H. Roohani, B. W. Skews and I. M. A. Gledhill, "Application of Moving Reference Frame to a Supersonic Accelerating Body", *Proceedings of the 23rd International Shock Interaction Symposium*, Kruger National Park, South Africa, 9-13 July 2018, ed. R. T. Paton and B. W. Skews, 209-214, 2018 ISBN 978-0-620-80449-3 (ebook) 978-0-620-80448-6 (Print)

[21] Y. Yamashita *et al.*, "Supersonic Flow Fields with Various Deceleration Levels," in *Proceedings of the 32nd International Symposium on Shock Waves (ISSW32 2019)*, Research Publishing Services, 2019, pp. 2601–2612. doi: 10.3850/978-981-11-2730-4_0496-cd.
[22] M. R. Ahmed, T. Takasaki, and Y. Kohama, "Aerodynamics of a NACA4412 Airfoil in Ground Effect," *Am. Inst. Aeronaut. Astronaut. AIAA J.*, vol. 45, no. 1, p. 37, Jan. 2007.
[23] N. A. Ahmed and J. Goonaratne, "Lift Augmentation of a Low-Aspect-Ratio Thick Wing in Ground Effect," *J. Aircr.*, May 2012, doi: 10.2514/2.2940.
[24] M. R. Ahmed and S. D. Sharma, "An investigation on the aerodynamics of a symmetrical airfoil in ground effect," *Exp. Therm. Fluid Sci.*, vol. 29, no. 6, pp. 633–647, Jul. 2005, doi: 10.1016/j.expthermflusci.2004.09.001.
[25] C. Coulliette and A. Plotkin, "Aerofoil ground effect revisited," *Aeronaut. J.*, vol. 100, no. 992, pp. 65–74, Feb. 1996, doi: 10.1017/S0001924000027305.
[26] C.-M. Hsiun and C.-K. Chen, "Aerodynamic characteristics of a two-dimensional airfoil with ground effect," *J. Aircr.*, vol. 33, no. 2, pp. 386–392, Mar. 1996, doi: 10.2514/3.46949.
[27] M. R. Ahmed, "Aerodynamics of a Cambered Airfoil in Ground Effect," *Int. J. Fluid Mech. Res.*, vol. 32, pp. 157–183, Jan. 2005, doi: 10.1615/InterJFluidMechRes.v32.i2.30.
[28] J. W. Vogt, T. J. Barber, and E. Leonardi, "Flow Field Phenomena about Lift and Downforce Generating Cambered Aerofoils in Ground Effect," presented at the 16th Australasian Fluid Mechanics Conference (AFMC), School of Engineering, The University of Queensland, 2007, pp. 328–335. Accessed: Jul. 17, 2017. [Online]. Available: https://espace.library.uq.edu.au/view/UQ:120803
[29] T. Barber, "Aerodynamic ground effect: a case study of the integration of CFD and experiments," *Int. J. Veh. Des.*, vol. 40, no. 4, p. 299, 2006, doi: 10.1504/IJVD.2006.009068.
[30] G. Doig and T. J. Barber, "Considerations for Numerical Modeling of Inverted Wings in Ground Effect," *AIAA J.*, vol. 49, no. 10, pp. 2330–2333, Oct. 2011, doi: 10.2514/1.J051273.
[31] J. Gross and L. W. Traub, "Experimental and Theoretical Investigation of Ground Effect at Low Reynolds Numbers," *J. Aircr.*, vol. 49, no. 2, p. 576, Apr. 2012.
[32] J. W. Vogt and T. J. Barber, "Ground effect phenomena about lift and downforce generating cambered aerofoils," *Int. J. Numer. Methods Heat Fluid Flow Bradf.*, vol. 22, no. 2, pp. 153–174, 2012, doi: http://0-dx.doi.org.innopac.wits.ac.za/10.1108/09615531211199809.
[33] S. Diasinos, T. J. Barber, and G. Doig, "Influence of wing span on the aerodynamics of wings in ground effect," *Proc. Inst. Mech. Eng. Part G J. Aerosp. Eng.*, vol. 227, no. 3, pp. 569–573, Mar. 2013, doi: 10.1177/0954410011434884.
[34] G. Doig, T. J. Barber, A. J. Neely, and D. D. Myre, "Aerodynamics of an aerofoil in transonic ground effect: numerical study at full-scale Reynolds numbers," *Aeronaut. J.*, vol. 116, no. 1178, pp. 407–430, Apr. 2012, doi: 10.1017/S0001924000005297.
[35] G. Doig, T. J. Barber, and A. J. Neely, "The Influence of Compressibility on the Aerodynamics of an Inverted Wing in Ground Effect," *J. Fluids Eng.*, vol. 133, no. 6, pp. 061102-061102–12, Jun. 2011, doi: 10.1115/1.4004084.
[36] G. C. Doig, T. J. Barber, E. Leonardi, A. J. Neely, and H. Kleine, "Methods for investigating supersonic ground effect in a blowdown wind tunnel," *Shock Waves*, vol. 18, no. 2, pp. 155–159, Jul. 2008, doi: 10.1007/s00193-008-0144-z.
[37] S. I. Silton, "Navier-Stokes Computations for a Spinning Projectile from Subsonic to Supersonic Speeds," *J. Spacecr. Rockets*, vol. 42, no. 2, pp. 223–231, 2005, doi: 10.2514/1.4175.
[38] G. Pechuzal and J. Kevorkian, "Supersonic-Transonic Flow Generated by a Thin Airfoil in a Stratified Atmosphere," *SIAM J. Appl. Math. Phila.*, vol. 33, no. 1, p. 26, Jul. 1977, doi: http://0-dx.doi.org.innopac.wits.ac.za/10.1137/0133002.
[39] NATO, Ed., *Experimental data base for computer program assessment*. in AGARD advisory report, no. 138. Neuilly-sur-Seine: AGARD, 1979.
[40] T. Coakley, "Numerical simulation of viscous transonic airfoil flows," in *25th AIAA Aerospace Sciences Meeting*, American Institute of Aeronautics and Astronautics, 1987. doi: 10.2514/6.1987-416.
[41] F. Mohebbi, B. Evans, and M. Sellier, "On an Exact Step Length in Gradient-Based Aerodynamic Shape Optimization—Part II: Viscous Flows," *Fluids*, vol. 6, no. 3, Art. no. 3, Mar. 2021, doi: 10.3390/fluids6030106.
[42] G. Doig, "Transonic and supersonic ground effect aerodynamics," *Prog. Aerosp. Sci.*, vol. 69, pp. 1–28, Aug. 2014, doi: 10.1016/j.paerosci.2014.02.002.

[43] T. J. Barber, G. Doig, C. Beves, I. Watson, and S. Diasinos, “Synergistic integration of computational fluid dynamics and experimental fluid dynamics for ground effect aerodynamics studies,” *Proc. Inst. Mech. Eng. Part G J. Aerosp. Eng.*, vol. 226, no. 6, pp. 602–619, Jun. 2012, doi: 10.1177/0954410011414321.
[44] H. Roohani, I. M. A. Gledhill, I. Mahomed, and B. W. Skews, “Bow shock stand-off distance for subsonic decelerating bodies,” *Shock Waves*, vol. 30, no. 2, pp. 115–129, Mar. 2020, doi: 10.1007/s00193-019-00921-3.

APPENDIX A: User-Defined Function for Modelling Acceleration

Fluent does not have the function for modelling non-inertial reference frames. In the case of constant acceleration, the momentum source term is constant, and this value can be set in the Fluent source term panel. However, the energy source term is not constant and the following user-defined function (UDF) is an example of how the energy source term is applied to every cell in the fluid. [19] The code is written in the programming language C.

```
#include "udf.h"
DEFINE_SOURCE(uns_Energy,c,t,dS,eqn)
{
real source;
float time, Energy;
time = RP_Get_Real("flow-time");
Energy = 1.176674*347.0877*(0.1+0.25*time)*0.25*347.0877;
source = Energy;
dS = 0;
return source;
}
DEFINE_PROFILE(unsteady_Mach, thread, position)
{
float t, Mach;
face_t f;
t = RP_Get_Real("flow-time");
Mach = (0.1+0.25*t);
begin_f_loop(f, thread)
{
F_PROFILE(f, thread, position) = Mach;
}
end_f_loop(f, thread)
}
```

In the given code, a constant acceleration of M0.25 every second was applied to the flow. This equates to an acceleration of 86.77m/s^2 (~8.85g). The density of the air was 1.176674kg/m^3 at a pressure and temperature of 101.325kPa and 300K. For the energy variable defined above, the velocity and acceleration were based on the far-field Mach number and the velocity is increased from the initial value of M0.1 by 0.25 each time step.